Alma Mater Studiorum — Università di Bologna

SCUOLA DI SCIENZE
Corso di Laurea Magistrale in Astrofisica e Cosmologia
Dipartimento di Fisica e Astronomia

Heavily obscured AGN: an ideal laboratory to study the early co-evolution of galaxies and black holes

Tesi di Laurea Magistrale

Candidato:
Chiara Circosta

Relatore:
Chiar.mo Prof.
Cristian Vignali

Correlatore:
Dr. Roberto Gilli

Sessione I
Anno Accademico 2015-2016

Abstract

A crucial science goal of modern astrophysics consists in understanding the formation and evolution of supermassive black holes (SMBHs). A key phase of their history occurs when the BH is rapidly growing within a highly star-forming galaxy. However, phases of intense accretion in active galactic nuclei (AGN) are often coupled with heavy obscuration, which challenges our attempt to identify and investigate them especially at high redshift, when the reservoirs of available gas were larger. X-ray emission produced by the AGN is a good tracer of this accretion activity, but it can be heavily depressed by passing through the obscuring material, limiting the detection of these sources in the X-ray band. In general, deep X-ray surveys are very powerful tools, as they allow to efficiently detect large populations of AGN up to high redshift, although the most obscured ones (which constitute the bulk of the SMBH growth in the Universe) still escape detection. During this evolutionary stage, the central engine is intimately connected with its host galaxy, as large amounts of gas can induce both obscured accretion and star formation. These hosts often show up as submillimeter galaxies (SMGs), which trace the most active phase in the lifetime of massive systems at high redshift. Therefore, to have a complete view of this class of sources and achieve a better comprehension of the early co-evolution of galaxies and black holes, it is fundamental to fully characterize the host-galaxy properties via a multiwavelength approach.

In this work we present a multiwavelength study of a sample of six X-ray selected type-2 AGN in the *Chandra* Deep Field South (CDF-S) at $z > 2.5$, characterized by heavy obscuration and good FIR/sub-mm detections. We performed the X-ray spectral analysis based on the 7Ms *Chandra* dataset, which provides the best X-ray spectral information currently available for distant AGN. We were able to place constraints on the obscuring column densities and the intrinsic luminosities of our targets, as well as to study the iron emission line whose equivalent width is particularly high in obscured AGN. Moreover, we built up the UV to FIR spectral energy distributions (SEDs) by combining the broad-band photometry from CANDELS and the *Herschel* catalogs, and analyzed them by means of an SED decomposition technique. Therefore, we de-

rived important physical parameters of both the host galaxy and the AGN, such as stellar mass, IR luminosity, SFR and AGN bolometric luminosity. In addition, we obtained, through an empirical calibration, the gas mass in the host galaxy and assessed the galaxy sizes in order to estimate the column density associated with the host ISM.

The comparison of the ISM column densities with the values measured from the X-ray spectral analysis pointed out that the contribution of the host ISM to the obscuration of the AGN emission can be substantial, ranging from $\lesssim 10\%$ up to $\sim 100\%$ of the value derived from the X-ray spectra. The absorption may occur at different physical scales in these sources and, in particular, the medium in the host galaxy is an ingredient that should be taken into account, since it may have a relevant role in driving the early co-evolution of galaxies with their black holes. It appears therefore likely that the obscuration is not totally ascribed to the parsec-scale torus of the unified model, but that a fraction of the obscuration is related to the host galaxy, at least at high redshift.

Sommario

Uno degli obiettivi scientifici più importanti dell'astrofisica moderna consiste nella comprensione della formazione e dell'evoluzione dei buchi neri supermassivi (SMBHs). Una fase chiave della loro evoluzione si verifica quando il buco nero aumenta rapidamente la propria massa all'interno di una galassia con alta formazione stellare. Tuttavia, queste fasi di forte accrescimento all'interno dei nuclei galattici attivi (AGN) sono associate ad un alto oscuramento che ne rende difficoltoso lo studio, in particolare ad alto redshift, quando le galassie contengono una quantità maggiore di gas. L'emissione X prodotta dagli AGN è un buon tracciante di questa attività di accrescimento ma può essere fortemente attenuata dal passaggio attraverso il mezzo oscurante, limitando la detezione di queste sorgenti in banda X. In questo ambito, le survey X profonde sono strumenti estremamente efficaci in quanto permettono di selezionare in modo efficiente popolazioni numerose di AGN, sebbene le sorgenti più oscurate (che costituiscono i principali protagonisti dell'attività di accrescimento dei SMBH nell'Universo) non siano ancora state rivelate. Durante questa fase evolutiva, l'attività del buco nero centrale è strettamente "connessa" a quella della propria galassia ospite, dato che le grandi quantità di gas presenti nella galassia possono indurre attività di accrescimento e di formazione stellare. Spesso le galassie ospiti mostrano una intensa emissione in banda sub-millimetrica (dette submillimeter galaxies) durante la fase più attiva delle sorgenti massicce ad alto redshift. Pertanto, al fine di avere una visione completa di questa classe di oggetti e ottenere una migliore comprensione della fase primordiale di coevoluzione di galassie e buchi neri, è fondamentale caratterizzare in maniera completa le proprietà delle galassie ospiti seguendo un approccio multifrequenza.

In questo lavoro di tesi presentiamo uno studio multifrequenza di un campione costituito da sei AGN di tipo 2 selezionati in banda X nel *Chandra* Deep Field South (CDF-S) a $z > 2.5$, caratterizzati da forte oscuramento e buoni dati in banda FIR/sub-mm. E' stata effettuata l'analisi degli spettri estratti dai 7Ms di osservazione ottenuti con il satellite *Chandra* nel CDF-S, i quali forniscono i dati più accurati attualmente disponibili per AGN distanti. Tramite questa analisi sono state misurate

le densità di colonna e si sono ricavate le luminosità intrinseche delle sorgenti, ed è stato possibile studiare la riga di emissione del ferro, la cui larghezza equivalente è particolarmente elevata negli AGN oscurati. Inoltre, combinando fotometria multi-banda dalla survey CANDELS a dai cataloghi *Herschel*, sono state ottenute le distribuzioni spettrali di energia (SEDs), in seguito analizzate tramite una tecnica di decomposizione spettrale. Sono stati così derivati alcuni parametri fisici fondamentali che caratterizzano la galassia ospite e l'AGN, come la massa stellare, la luminosità infrarossa, il tasso di formazione stellare e la luminosità bolometrica dell'AGN. Inoltre, mediante una calibrazione empirica, è stata ottenuta la massa del gas contenuto nella galassia. Combinando questa informazione con la stima della dimensione della sorgente è stato possibile ricavare la densità di colonna associata al mezzo interstellare (ISM).

Il confronto delle densità di colonna dell'ISM con i valori misurati dall'analisi degli spettri X mostra che il suo contributo all'oscuramento dell'emissione dell'AGN può essere significativo, tra il 10 e il 100% del valore derivato dall'analisi spettrale X. L'oscuramento in queste sorgenti potrebbe avvenire su scale fisiche diverse; in quest'ottica, il mezzo nella galassia ospite risulta essere un ingrediente non trascurabile in quanto potrebbe avere un ruolo rilevante nello scenario coevolutivo di galassie e buchi neri supermassivi. Sembra probabile, quindi, che l'oscuramento non sia completamente attribuibile al toro su scala del parsec assunto dal modello unificato, ma che una frazione dell'oscuramento sia legata alla galassia ospite, almeno ad alto redshift.

Contents

Chapter 1

Introduction

Active galactic nuclei (hereafter AGN) are among the most spectacular objects in the sky. They produce huge amounts of energy in very concentrated volumes. These powerful and compact energy sources are observed in approximately $1 - 10\%$ of all galaxies. Moreover, their emission can emerge over an extraordinarily broad range of wavelengths, from the radio band to the gamma regime. Their luminosities cannot be attributed to the normal components of galaxies such as stars, dust and gas. Indeed, AGN are assumed to be powered by accretion activity onto a super massive black hole (SMBH) located at their center. From an observational point of view, an object is classified as an AGN if it presents at least one of the following properties: it contains a compact nuclear region whose luminosity is significantly beyond what is expected from stellar processes typical of normal galaxies; it shows the clear signature of a nonstellar continuum emitting process in its center; its spectrum contains strong emission lines with line ratios that are typical of excitation by a nonstellar radiation field; it shows line and/or continuum variations (Netzer 2013).

In the following, we will describe the scientific background in which our study lies, providing a brief overview of the AGN physical and spectral properties. Then, we will focus on the issues related to obscured AGN, with particular attention to their evolution with cosmic time, as well as on their host galaxy properties.

1.1 AGN components

The physical structure of an AGN and the corresponding formation mechanisms are, at present, not perfectly known and are still matter of debate. In AGN, different components are concentrated in extremely small sizes and direct investigations are

not possible due to observational limitations that prevent the study of their innermost region ($\lesssim$ parsec). Nevertheless, some information on the sizes of the central regions can be obtained through variability studies. Moreover, the properties of each component depends on density, composition, as well as its location with respect to the central BH. We provide a brief description of what are believed to be the main components of the AGN structure, with a schematic representation shown in Fig. 1.1. The corresponding approximate sizes are reported in Table 1.1.

SMBH. It is thought to be the central engine of the AGN. BHs are the most compact objects in the Universe as well as extreme cases of curved space-time, described by general relativity. According to the current theory, a black hole can be completely described by only three properties: mass, charge and angular momentum. The mass of a SMBH ranges between $\sim 10^6$ and $\sim 10^9$ $M_\odot$, but a few examples are known even outside this range. The most basic characteristic that defines a BH is the presence of an event horizon, i.e. a boundary from which matter and even light can never re-emerge. It is described by the gravitational radius, defined as $r_g = GM_{BH}/c^2$. Charge is usually assumed to be zero, i.e. neutral black holes. As for the angular momentum J, it is described by the adimensional angular momentum per unit mass, often called spin, $a = Jc/GM_{BH}^2$. This quantity can assume all values between $+1$ and -1: it is positive if the direction of BH rotation is the same of that of the accreted inflowing material, it is negative otherwise. The radius of the event horizon, in units of r_g, is given by $r_\pm = 1 \pm (1 - a^2)^{1/2}$. If $a = 0$ we have a static BH with an event horizon described by the Schwarzschild radius $R_s = 2GM_{BH}/c^2$. Instead, if $a = 1$, the BH is maximally rotating and is described by the Kerr metric. It is characterized by an additional surface, the static limit $r_0 = 1 + (1 - a^2 \cos^2\theta)^{1/2}$, which defines, along with r_+, a region called ergosphere, where the BH drags particles to rotate and it is theoretically possible to extract energy and mass from this region. Moreover, particles in orbital motion around a BH fall directly into the event horizon if they are beyond the innermost stable circular orbit (ISCO), which is equal to $6r_g$ for a Schwarzschild BH, while for a Kerr BH it ranges between 1 and $6r_g$ if $a > 0$, and farther away from the BH, up to $9r_g$, in case of retrograde accretion ($a < 0$). The process at work in an active nucleus is the conversion of gravitational potential energy into electromagnetic radiation. In particular, energy is generated by gravitational infall of material which is heated to

high temperatures in a dissipative accretion disk. This process depends on the radius of the ISCO, as the smaller the radius is, the larger is the fraction of energy converted (Netzer 2013). Concerning the accretion process, two fundamental quantities need to be defined, the Eddington luminosity $L_{\rm Edd}$ and the Eddington accretion rate $\dot{M}_{\rm Edd}$. In case of spherical accretion of fully ionized gas onto the central object, the Eddington luminosity is a critical value achieved when the outward radiation pressure equals the inward gravitational force. Above the Eddington limit, radiation pressure overcomes gravity and the gas is pushed away. These quantities are related by the equation:

$$L_{\rm Edd} = \eta \dot{M}_{\rm Edd} c^2 = \frac{4\pi c G M_{\rm BH} \mu m_{\rm p}}{\sigma_{\rm T}} \simeq 1.5 \times 10^{38} \left(\frac{M_{\rm BH}}{M_\odot} \right) \text{ erg s}^{-1} \qquad (1.1)$$

where η is the mass-to-luminosity conversion efficiency and depends on how the accretion occurs (usually assumed of order 0.1), μ is the mean molecular weight, $m_{\rm p}$ is the mass of proton and $\sigma_{\rm T}$ is the Thomson cross section.

Accretion disk. It forms when matter is falling towards the BH. The viscosity and the turbulent processes of the disk transfer outward the angular momentum of the gas and allow it to spiral into the center, losing a considerable fraction of its gravitational energy. The energy lost in the process can be converted into electromagnetic radiation with high efficiency, from about 6% up to about 40%. It can also be converted into kinetic energy of the gas, which is blown away from the disk, or it can heat the gas to very high temperatures, which causes much of the energy to be advected into the BH. AGN disks can be optically thick or thin, depending on the column density, the level of ionization of the gas and the mass accretion rate (e.g. Netzer 2013). A commonly assumed model of accreting disk is the optically thick, geometrically thin accretion disk (Shakura & Sunyaev 1973). Assuming that the medium is optically thick and that the energy at a distance r from the BH is dissipated locally, the local emission can be assumed as a perfect blackbody. Thus, the accretion disk can be divided in annuli, each emitting as a black body. The overall emission can be explained as a multicolor black body, i.e. a sum of different temperature blackbody spectra. The result is a power-law spectra $S_\nu \propto \nu^{1/3}$, and a decreasing disk temperature as a function of the radius (Peterson 2003):

$$T(r) \sim 6.3 \times 10^5 \, M_8^{-1/4} \left(\frac{\dot{M}}{\dot{M}_{\rm Edd}} \right)^{1/4} \left(\frac{r}{R_{\rm S}} \right)^{-3/4} \; K \qquad (1.2)$$

where $\dot{M}$ is the accretion rate, $\dot{M}_{\rm Edd}$ is the Eddington accretion rate, M_8 is the black hole mass in units of 10^8 $M_\odot$ and $R_{\rm S}$ is the Schwarzschild radius. In particular, for a disk surrounding a 10^8 $M_\odot$ black hole accreting at the Eddington rate, the maximum temperature is roughly $T \sim 10^5$ K. Therefore, such disk emits most of its energy in the UV/soft-X part of the spectrum. However, real AGN disks are quite different from the simple, optically thick, geometrically thin disk commonly assumed, as several elements (such as strong magnetic fields) can affect the physics and the structure of these systems.

Hot corona. It is probably a hot, rarefied gas ($T \sim 10^{8-9}$ K, $n \sim 10^8$ cm^{-3}) located $\sim$3-10 $r_{\rm g}$ above the disk in which the soft thermal photons produced by the disk are upscattered to their observed X-ray energy, thus explaining the origin of the energetic X-ray emission from AGN. The condition for the formation of a hot corona around thin accretion disks is still unknown, but it could be related to a direct consequence of the internal dynamics of an accretion disk. Different possibilities have been proposed, for instance the formation mechanism might be due to the large density gradient in the vertical direction of the disk with part of the accretion proceeding through the lower-density, outer layers, resulting in a large energy dissipation and an expansion of the outer layers themselves (Netzer 2013). Another possibility is related to an instability in weakly magnetized accretion flows, responsible for the transport of angular momentum (Di Matteo 2000). The simplest model involves an optically thin corona with a small scale height, whose temperature is determined by the fraction of the total accretion power deposited into the corona itself. Even a small fraction can result in temperatures of $\sim 10^8$ K (Netzer 2013). However, the heating mechanism and the exact geometry are, at present, open issues.

Broad Line Region (BLR). It contains clouds of gas located in proximity of the central source, which dominates the bulk motion of this region. The gas reprocesses the energy produced by the continuum source at ionizing ultraviolet energies through emission lines from recombination or de-excitation of photoionized atoms. The BLR electron densities are sufficiently high ($\sim 10^{9-10}$ cm^{-3}) that basically all forbidden lines are collisionally suppressed. The gas temperature is of about 10^4 K. Due to the Doppler shift that affects the emitting clouds, the permitted emission lines from the BLR are broad, characterized by widths ranging from $\Delta v_{\rm FWHM} \sim 500$ km s^{-1} to $\Delta v_{\rm FWHM} \gtrsim 10^4$ km s^{-1}, with typical values $\Delta v_{\rm FWHM} \sim 5000$ km s^{-1} (Peterson 2003). This emission

can be a useful probe of the central engine, as the clouds reside deep inside its gravitational potential well and are located up to $0.1 - 1$ pc from the center. Moreover, the BLR is dust-free, being within the dust sublimation radius (§ 4.1.3).

Narrow Line Region (NLR). It extends for some hundreds of parsecs and is the largest spatial scale where the ionizing radiation from the central source can excite the surrounding medium. The electron densities are low enough ($\sim 10^4$ cm^{-3}) to allow the production of forbidden lines, which are not collisionally suppressed through recombination processes. The electron temperatures are in the range $10000 - 25000$ K. The clouds of gas in this region have velocities lower than those characterizing the BLR. Indeed, the FWHM of the narrow lines is in the range $200 \lesssim \Delta v_{\rm FWHM} \lesssim 900$ km s^{-1}, with most values around $350 - 400$ km s^{-1}. The NLR arises outside the dust sublimation radius, hence significant amount of dust are present as the radiation field is much weaker. Probably, the radius where dust sublimates represents the transition boundary between the BLR and the NLR. Moreover, this is the only AGN component spatially resolved in the optical, revealing an axisymmetric morphology rather than a spherically symmetric one, with two opposite ionization cones centered into the nuclear source (Peterson 2003).

Obscuring torus. It is the region between about 0.1 and 10 pc from the central BH. Interpolation between the BLR and NLR properties suggests gas density of about $10^4 - 10^7$ cm^{-3} and velocities of the gas of about 1000 km s^{-1}. The region is beyond the dust sublimation radius and is likely to contain dust and molecular gas. In particular, the gas at the inner radius of the torus is ionized by the central source, while at larger distances there is neutral and molecular material. The related opacity, at all wavelengths except for the infrared where the torus emits the reprocessed radiation, must be large and hence the central source is obscured for certain lines of sight. Indeed, this component is characterized by a broad range of obscuring column densities, whose estimate is particularly good through X-ray observations (Netzer 2013). The matter distribution of the torus is modelled with smooth or clumpy distributions, described in more detail in § 4.

Jets. These extended linear structures are present in almost all powerful radio-loud AGN. Radio-loud AGN represent $\sim 10\%$ of luminous AGN and are usually

separated from radio-quiet AGN by means of the radio loudness parameter R, that is a measure of the ratio of radio to optical monocromatic luminosity, $R = \frac{L_\nu(5\,\mathrm{GHz})}{L_\nu(4400\,\text{Å})}$ (Kellerman et al. 1989). The jet origin point coincides with the location of the optical-UV and X-ray continuum source. These relativistc jets, aligned with the symmetry axis of the system, emit mostly through synchrotron mechanism, from the radio band to the γ-rays. The formation mechanism is still unknown, but it is probably related to a fast rotating black hole and the magnetic field that can collimate the outflow of charged particles, leading to jet structures which transport energy and particles from the central compact source to the extended regions. They are affected by "Doppler beaming", the relativistic effect that enhances the surface brightness of the jet that is approaching the observer with respect to the other. Weaker jets decelerate closer to the central engine, even inside the host galaxy, while the most powerful propagate into the interstellar and intergalactic medium up to Mpc scales. The interaction between jets and the environment causes the formation of hot spots and large-scale radio lobes.

Component	Approximate size
BH	$R_\mathrm{S} \sim 0.01 - 10$ AU^a
Accretion disk	$\mathrm{R_{in}} \sim 0.01 - 60$ AU^b
	$\mathrm{R_{out}} \sim 1 - 1000$ AU^c
Broad line region	$\mathrm{R_{BLR}} \sim 0.01 - 1$ pc
Molecular torus	$\mathrm{R_{torus}} \sim 1 - 10$ pc
Narrow line region	$\mathrm{R_{NLR}} \sim 10^2 - 10^4$ pc
Jet	$\mathrm{R_{jet}} \sim 100 - 1000$ kpc

Table 1.1: Size ranges of the extension of the different components considered to be part of the AGN phenomenon. ^{a} Radius of the event horizon; ^{b} inner radius; ^{c} outer radius.

1.2 Spectral properties of AGN

The emission from the different components described above comes into play building up the AGN spectral energy distribution (SED). It can be described, to a first-

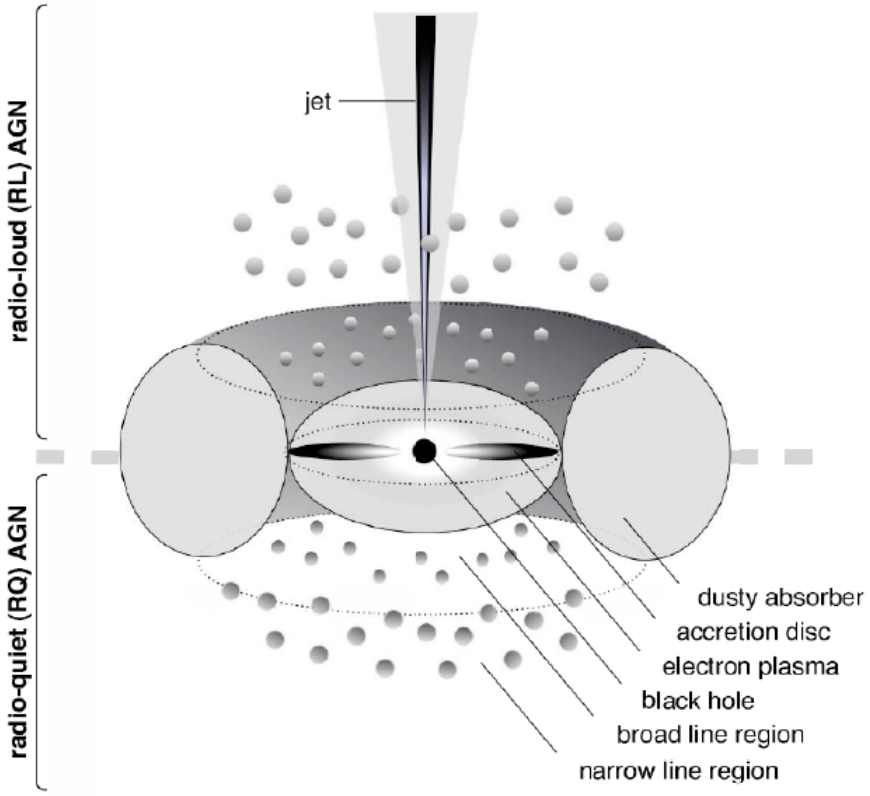

Figure 1.1: Schematic representation of the AGN structure and its main components. Radio-loud sources, which show the presence of jets and are bright in the radio band, are distinguished from radio-quiet sources, which have no or weak radio emission. This simplified view is not to scale. Image taken from Beckmann & Shrader 2012.

order approximation, as a power law $S_\nu \propto \nu^{-\alpha}$, with the spectral index ranging generally between 0 and 1. The primary radiation from the central engine is the driving force for all other secondary processes, each one producing specific spectral features. The physics underlying the observed emission involves several emission mechanisms and a complex interplay between them. Across the whole electromagnetic spectrum, ignoring emission from the underlying galaxy, the following continuum properties can be distinguished (see, e.g., Peterson 2003, Risaliti & Elvis 2004, Beckmann & Shrader 2012):

- The radio emission is significantly different for radio-loud and radio-quiet sources. In radio-loud objects, a strong, non-thermal continuum extends from the radio to the far-IR, while in radio-quiet objects the SED decreases rapidly at low energies (the so-called "submillimeter break"). Fig. 1.3 shows a typical SED for both radio-loud and radio-quiet AGN, from the radio to the X-ray

band. The emission is due to rapidly accelerated charged particles and magnetic fields producing a power-law continuum spectrum through synchrotron emission. In some sources, the synchrotron radiation extends to the X-rays or even the γ-rays. The radio emitting regions are the compact core and the extended regions. The compact emission component is believed to be coincident with a position close to the central black hole, where the jets become optically thin. The extended emission is due to the jets, with their lobes and hot spots resulting from interactions between the jet and the environment. However, the radio contribution to the bolometric luminosity is small.

- The IR emission between a few μm up to about 100 μm is mainly produced by the dusty torus. It has a spectral shape characterized by a minimum at $\sim 1-2$ μm due to the sublimation temperature of the dust, a bump at typical wavelengths of about $10-30$ μm due to thermal emission of hot dust with temperatures ranging between 50 and 1000 K, and a steep decline due to the decreasing emitting efficiency of dust grains. This wavelength range, for radio-loud AGN, can be also associated with non-thermal emission, produced by the same synchrotron emission that dominates in the radio regime.

- The optical and UV spectrum of quasars is characterized by the "big blue bump", ascribed to thermal emission from the accretion disk. It dominates the emission between $\sim$300 Å to $\sim$3000 Å, and the spectrum can be well approximated with a power law. An additional feature, the "small blue bump", consists of blended Fe emission lines and Balmer continuum. Moreover, several emission lines are present in quasar spectra. In particular, broad lines (such as Ly$\alpha\lambda$1216, CIVλ1549, NV$\lambda\lambda$1239, 1243, OVIλ1035) are emitted from the BLR, and narrow (forbidden) lines (such as [OIII]λ5007, [NII]λ6583, [OII]λ3727) from the NLR. The optical regime is still the best one to gather information about AGN classification and redshift.

1.2.1 X-ray emission

The X-ray domain is currently one of the key energy ranges to study AGN. In X-ray astronomy, power-law SED are given in units of photons s^{-1} cm^{-2} keV, and are of the form $N(E) = N_0 E^{-\Gamma}$, where Γ is the photon index. Alternatively, the detected quantity is usually plotted instead of the emitted quantity, in units of number of counts per second per cm^2 per keV, that is the intrinsic spectrum convolved with the

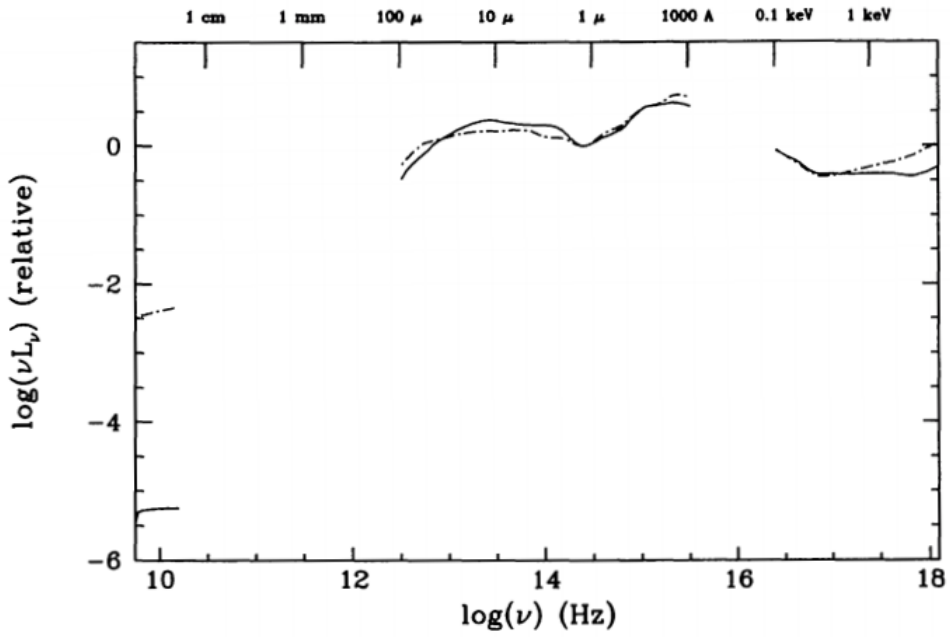

Figure 1.2: Mean SED of radio-loud (dashed line) and radio-quiet (solid line) quasars. In this plot, the former shows a rising X-ray spectrum, while the latter shows an horizontal X-ray spectrum. The two SEDs present a very different behaviour in the radio regime, being radio-loud AGN radio sources more powerful that radio-quiet ones, characterized by weak or no radio emission. Omitted spectral regions have few or no data available (from Elvis et al. 1994).

detector response. The energy flux is $F(E) = EN(E) = N_0 E^{-\alpha}$ where $\alpha = \Gamma - 1$ is the energy index. Finally, $EF(E)$ plotted versus E in logarithmic scales gives the energy at which the source luminosity peaks. As a result, hard spectra peaking at high energy have $\Gamma < 2$, soft spectra with $\Gamma > 2$ peak at low energies, while flat spectra have $\Gamma = 2$ (Done 2010). X-ray emission accounts for $\sim$10% of the bolometric luminosity of AGN[1]. This is one of the most interesting part of the AGN SED, as it shows some important and peculiar features typical of the presence of an active nucleus in the center of the galaxy. The X-ray emission extends from $\sim$0.1 keV up to $\sim$300 keV. Here we describe the different components that define the overall emission, shown in Fig. 1.3.

[1]However, there is a correlation between the bolometric correction $k_{\rm bol} = L_{\rm bol}/L_{\rm X}$ and the bolometric luminosity (e.g. Marconi et al. 2004, Lusso et al. 2012). In particular, for increasing bolometric luminosities, $k_{\rm bol}$ increases as well, being the X-ray luminosity less dominant.

Primary emission

The intrinsic X-ray spectra of quasars presents a power-law component extending from about 1 keV to hard energies up to 200 keV. It is produced by the thermal Comptonization of the soft X-ray photons from the accretion disk occurring in the hot corona, situated above the disk itself. In particular, the thermal seed photons undergo Inverse Compton scattering from the energetic electrons, which boost their energy. In turn, each seed becomes the seed photon for next scattering events. Eventually, all the different scattering orders build up the resulting power-law spectrum (Done 2010). It is characterized by an exponential cut-off at $\sim 80-300$ keV, i.e. the values for which the energies of electrons and photons are comparable and the energy transfer from the former to the latter becomes inefficient. The process depends on the optical depth and the temperature of the electron thermal distribution.

In addition to the main power-law continuum component there is also a soft emission with characteristic temperature $kT \sim 0.2-1$ keV called "soft excess", the exponential tail of the "blue bump" at high energy, produced by thermal emission from the accretion disk. Alternatively, this emission could be due to ionized reflection from the accretion disk (Fabian & Miniutti 2005).

Reflection component

While about half of the primary photons can reach the observer, the remaining part is directed back to the accretion disk, giving rise to the reflection spectrum which is the result of both Compton scattering and photoelectric absorption. Since these processes are energy-dependent, the incident soft X-rays are mostly absorbed, whereas hard photons are Compton scattered out of the disk. The reflection continuum peaks at $\sim 20-30$ keV, with a cut-off at $4-5$ keV due to photoelectric absorption of the lower energy incident radiation. Above a few tens of keV, Compton recoil reduces the backscattered photon flux, as at high energy the interaction cross-section is smaller and photons penetrate at larger depths in the disk, losing energy and making absorption relevant again. The combination of these effects produces a broad hump-like structure called Compton hump. The reflected emission is typically a few percent of the primary one in the $2-10$ keV band.

Iron line

The most important feature in the 2-10 keV band is an iron emission line at a rest-frame energy of 6.4 keV. It arises from the same mechanism that produces

the reflection component, namely, photoelectric absorption of photons from the hot corona followed by fluorescent line emission or Auger de-excitation. These two processes occur when, after photoelectric absorption of an X-ray photon, one of the two electrons in the K-shell (i.e., $n = 1$) of the iron atom (or ion) is ejected. A threshold energy of 7.1 keV is required to have the absorption by neutral iron[2]. As a result, the excited state can decay following two ways: an electron in the successive shell (L, i.e. $n = 2$) de-excites into the K-shell either emitting an emission-line photon at 6.4 keV (34% probability), or ejecting an Auger electron, that internally absorbs the photon energy (66% probability). Actually, the line is a doublet, composed of the Kα1 and Kα2 lines at 6.404 and 6.391 keV respectively, but they are too close to be resolved. There is also a Kβ line at 7.06 keV, corresponding to a decay from the M (i.e., $n = 3$) to the K-shell, although the Kα transition is the most probable. If we consider ionized iron, the lower number of electrons is less able to screen the K-electrons from the nuclear charge, therefore the energies of both the photoelectric threshold and Kα line increase (6.7 keV for helium-like iron and 6.96 keV for hydrogen-like iron). This line is so prominent because iron, among all metals, has the best combination of fluorescent yield (i.e., the probability that a photoelectric absorption event is followed by fluorescent line emission rather than the Auger effect) and abundance (e.g. Fabian et al. 2000).

If the line is produced in the inner part of the accretion disk, its profile will be highly broadened and skewed. In particular, the red wing extending to lower energies is one of the best tool to look for general relativistic effects in strong gravity, carrying unique information on structure, geometry and dynamics of the emitting regions in the immediate vicinity of the central BH. The line shape is distorted by different effects: the Newtonian effect, which produces a double-peaked shape due to the approaching and the receding side of the disk, as well as special and general relativistic effects, more and more important close to the BH, which enhance the blue peak with respect to the red one and shift the line profile to lower energies. The total profile is the integral of the emission over all radii. It also depends on two main quantities: the inclination of the disk with respect to the observer's line of sight, as for higher inclinations the line is bluer due to the angular dependence of relativistic effects; the emission efficiency of the line as a function of the radius, which depends on how the disk is illuminated by the corona - e.g. the inner regions of the accretion disk can be illuminated more efficiently in case of a steep emissivity profile and hence

[2]It produces a feature in the spectrum (see Fig. 1.3), the so-called Compton edge, due to absorption of most incident photons just above the photoelectric threshold.

the innermost disk emission prevails over that of the external regions. Moreover, the line profile is also influenced by the spin of the BH, as the disk, which extends down to the ISCO (see § 1.1), is more or less close to the central engine depending on a (Fabian & Miniutti 2005).

There is also a second narrow component in this emission line, whose width is a few 1000 km s^{-1}, thus not showing relativistic effects. It does not vary when the continuum does and, in addition to the narrowness, this suggests that it originates far from the central BH. The torus walls, because of the large column density, are able to reflect the X-ray continuum radiation, thus producing the line (Risaliti & Elvis 2004). Moreover, emission-line photons may be scattered before they escape the medium, thus producing the "Compton shoulder" in the observed emission line, visible as a tail at lower energy. Photons that have been scattered once before escaping give the major contribution to the Compton shoulder. This effect depends on the column density, element abundances, orientation and geometry of the reprocessor (Murphy & Yaqoob 2009).

The equivalent width (EW) is usually adopted to measure the intensity of the line with respect to the continuum emission. It is defined as:

$$EW = \int \frac{F_{\rm l}(\lambda) - F_{\rm c}(\lambda)}{F_{\rm c}(\lambda)} d\lambda \tag{1.3}$$

where $F_{\rm l}(\lambda)$ is the observed flux of the emission line at the wavelength λ and $F_{\rm c}(\lambda)$ is the underlying continuum at the line energy. This quantity is a function of the geometry of the system, the element abundances, the inclination angle of the observer's line of sight and the ionization state.

1.3 The AGN family and the unified model

AGN are classified in several classes based on their emission properties at different wavelengths. The full family of AGN is a zoo of different names, which reflect different detection criteria and spectral and variability characteristics. The axisymmetric model which represents the AGN structure implies a radically different AGN appearance depending on the inclination of the object with respect to the observer's line of sight. Therefore, AGN with different orientations will be assigned to different classes. The AGN unification scheme (Antonucci 1993, Urry & Padovani 1995) was introduced to construct a general picture being able to explain and connect the various subgroups of AGN, thus attributing the observed properties to inclination

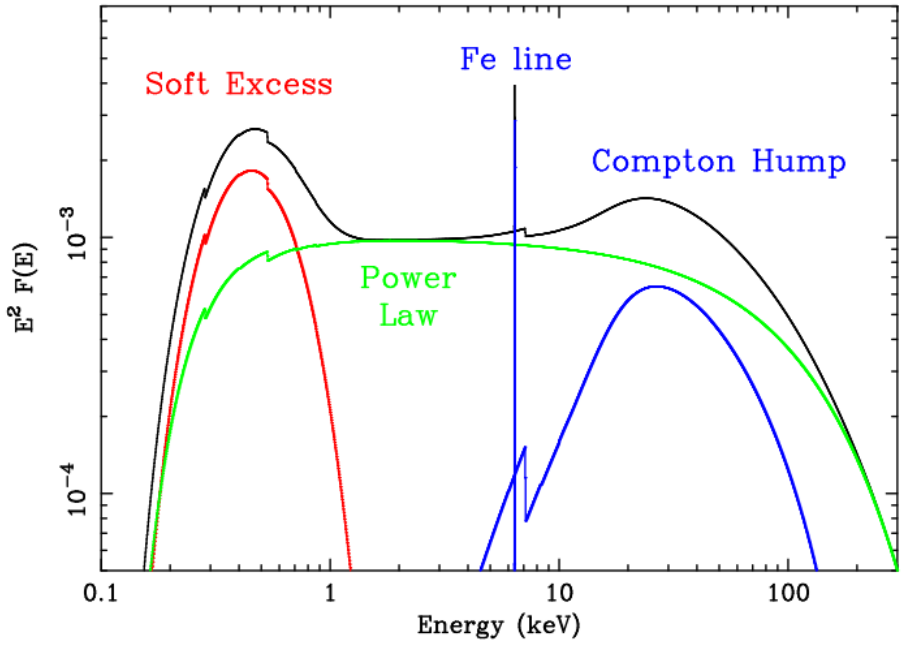

Figure 1.3: Main components of the X-ray spectra of unobscured AGN: soft emission from the accretion disk (red line), primary emission from thermal Comptonization of the soft X-rays from the hot corona (green line), reflected emission and Fe line due to reflection of hard X-rays from dense gas (blue line). The total emission is shown in black. Image taken from Fabian & Miniutti 2005.

effects of the same system, coupled with intrinsic differences in a small number of physical parameters (such as luminosity). The torus-like obscurer has been added to the two central components, namely the BH and the accretion disk, to explain the differences between type-1 and type-2 AGN. These two populations represent the biggest classes in which AGN can be divided and are based on the characteristics of their optical and ultraviolet spectra: the first group is characterized by brigth continua and broad emission lines (Fig. 1.4, *left panel*), as the line of sight does not intercept the obscuring torus; the second group presents weak continua and only narrow emission lines (Fig. 1.4, *right panel*), because of obscuration along the line of sight (basically, almost all optical-UV radiation from the inner parsec is absorbed). Instead, the classification in radio-loud and radio-quiet AGN according to their radio loudness is ascribed to the relativistic jets. Finally, the group of blazars includes radio-loud AGN in which the line of sight is close to the radio jet axis. Fig. 1.5 shows a schematic representation of the main AGN classification based on the inclination angle of the source.

AGN are also separated according to their luminosity: the name "Seyfert galax-

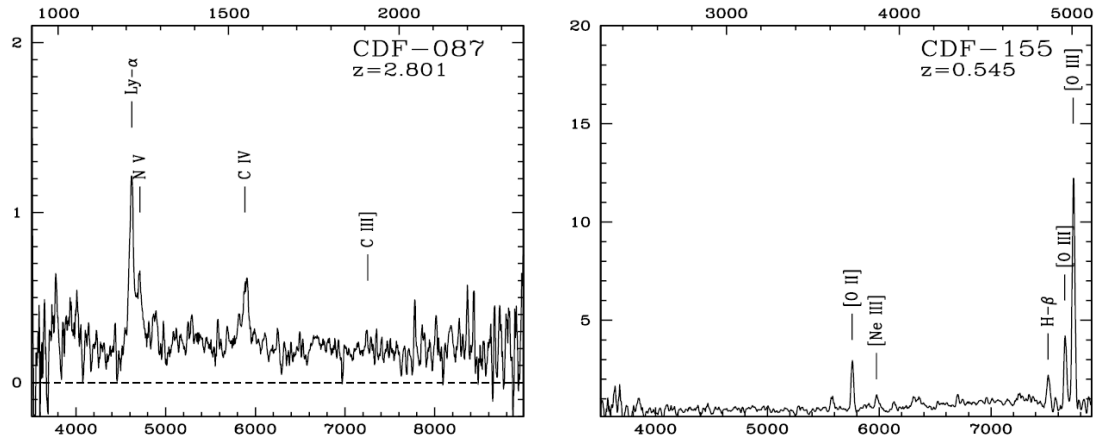

Figure 1.4: VLT spectra of two CDF-S sources, a type-1 (*left panel*) and a type-2 (*right panel*) AGN. Both rest-frame and observed wavelengths are shown on the top and on the bottom of the spectra. The measured flux is given in units of 10^{-18} erg cm^{-2} s^{-1} Å^{-1}. Important emission features are also marked (from Szokoly et al. 2004).

ies" is reserved for lower luminosity AGN, whereas "quasars" (QSOs) are considered to be more luminous members of the family. However, the dividing line between Seyfert galaxies and quasars has never been defined properly and is not very precise. Historically, QSOs were defined for $M_v < -23$, since preliminary samples of Seyferts/QSOs were selected in the optical/UV. The boundary is usually placed at about $L_{bol} \sim 10^{45}$ erg s^{-1}, where L_{bol} is the bolometric luminosity of the central source. In terms of X-ray luminosity, this division corresponds to $L_X \sim 10^{44}$ erg s^{-1} (Netzer 2013).

1.4 Obscured AGN

Obscured AGN are common objects both in the nearby and in the distant Universe. Locally, obscured AGN are $\sim$4 times more numerous than unobscured ones and this factor could be even higher at $z > 0.5 - 1$ (e.g. Maiolino & Rieke 1995, Gilli et al. 2001). Because of the effects produced by the obscuring medium along the line of sight, the spectral shape of this kind of objects proves to be modified in comparison to their unobscured counterparts. Absorption introduces a further spread in the emission properties of AGN, as the intrinsic emission is influenced by the amount, composition and geometry of the column density, producing large differences in their SEDs (Risaliti & Elvis 2004). The optical-UV continuum is heavily absorbed by dust and thermally re-radiated at infrared wavelengths, while narrow

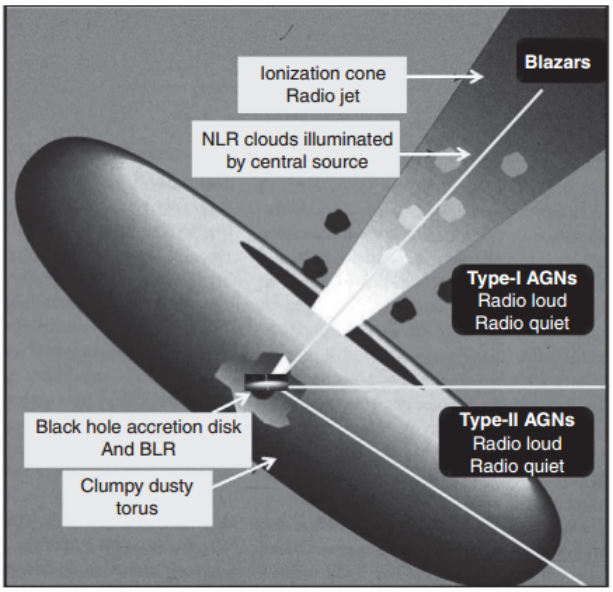

Figure 1.5: Schematic representation of the main AGN classes, based on the inclination angle of the observer's line of sight with respect to the torus axis. Type-I and Type-II classes refer to the optical/UV properties of the AGN spectrum, while the division between radio-loud and radio-quiet AGN is based on the loudness of their radio emission. Blazars are viewed along the jet direction. Moreover, the main AGN components are depicted (from Netzer 2013).

emission lines dominate the spectrum. As far as the X-ray regime is concerned, it suffers from photoelectric absorption, dominant at low energy (below $\sim$3 keV for $N_{\rm H} \sim 10^{23}$ cm^{-2}, even up to 10 keV, depending on the column density), as well as Compton scattering, dominant above $\sim$10 keV. Moreover, a prominent spectral feature, unambiguous signature of obscuration, is the iron Kα line, whose EW increases as a function of the column density, since it is measured against an absorbed continuum. For $N_{\rm H} < 10^{23}$ cm^{-2}, typical EW of about 100 eV are observed, while for higher column densities it reaches values of about 1 keV up to several keV. As explained above, this line is usually narrow ($\sigma = 0.1 - 0.01$ keV), being produced by a cold reflector far from the central BH.

How the emission getting through the obscuring medium appears depends on the amount of column density: if $N_{\rm H} \lesssim 10^{25}$ cm^{-2}, the direct X-ray emission of the AGN, with energies $>$10 keV, can penetrate the absorber emerging as transmitted emission. If $N_{\rm H} \gtrsim 10^{25}$ cm^{-2} no direct emission can survive as high-energy photons undergo multiple Compton scatterings that gradually decrease their energy until a photoelectric absorption can occur. Therefore, the high-energy spectrum is down-

scattered and depressed and the only detectable emission is the reflected one (Risaliti & Elvis 2004). Fig. 1.6 shows a model X-ray spectra of an AGN for different levels of absorption. At low energies a photoelectric cut-off is produced by absorption from cold gas and it moves towards higher energies for higher column densities, up to 10 keV. Likewise, the emission at $E > 10$ keV is more and more depressed until just the reflected emission emerges. Moreover, there is a soft component at low energy in excess of the absorbed power law, whose origin is not well known and may involve different processes: circumnuclear starburst, scattering of the primary power law by hot gas, fraction of the primary emission escaped the obscuring medium, sum of unresolved emission lines from photoionized gas (Gilli et al. 2007). However, it is usually a few % of the primary emission. Fig. 1.7 shows an observational validation of the model spectra described above. These X-ray spectra were obtained by Alexander et al. (2005b) by stacking the data for a sample of submillimeter galaxies at $z \sim 2$ in different obscuration classes. From top to bottom, as the column density increases, the observed spectrum is more and more absorbed and an emission feature comes out.

AGN can be classified according to the amount of X-ray absorption affecting their spectra: AGN with $N_{\rm H} < 1 \times 10^{24}$ cm^{-2} are called Compton-thin, whereas for $N_{\rm H} \geq 1 \times 10^{24}$ cm^{-2} we refer to Compton-thick AGN. Moreover, we consider AGN with $N_{\rm H} > 3 \times 10^{23}$ cm^{-2} as heavily obscured (e.g. Lanzuisi et al. 2015). $N_{\rm H} \sim 1.5 \times 10^{24}$ cm^{-2} corresponds to optical depths $\sim$1 for Compton scattering, i.e. the column density is equal to the inverse of the Thomson cross-section $\sigma_{\rm T}$. The cross-sections for Compton scattering and photoelectric absorption have approximately the same value for energies of order 10 keV, which means that for energies above 10 keV Compton scattering is the dominant process. This can be considered as the low-energy threshold for probing Compton-thick absorption regimes (e.g. Comastri 2004).

Because of the heavy absorption, type-2 AGN can be extremely elusive sources. Indeed, even when they dominate the bolometric emission of the galaxy, most of their primary emission is reprocessed by gas and dust, erasing most AGN signatures and making the distinction between the contributions from AGN and star forming regions very difficult. Thus, finding obscured AGN can be a hard job. But, in this regard, a major effort has been done by deep surveys (see § 2). Understanding the abundance of obscured AGN has several implications in astrophysics, and is currently subject of intense research activity. In particular, there are important research areas where a complete census of the AGN population and a deep study of

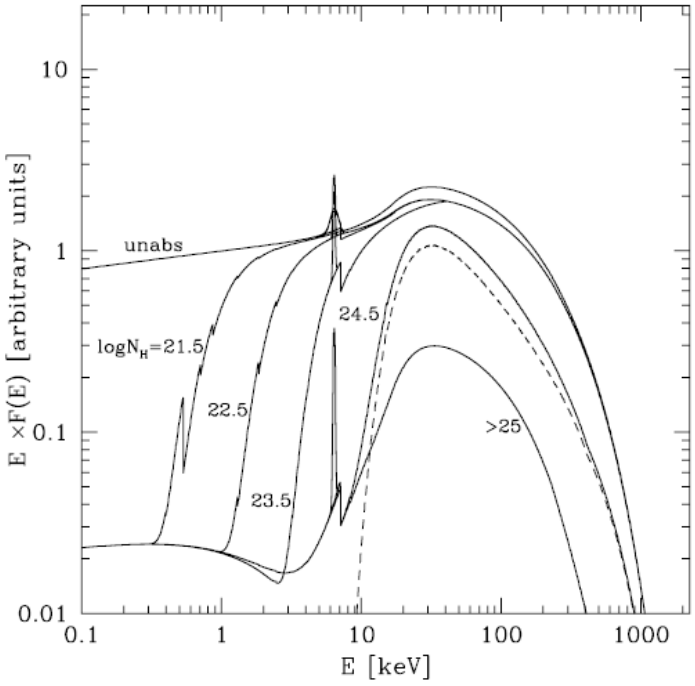

Figure 1.6: AGN X-ray spectrum with different levels of obscuration. From top to bottom, solid lines refer to increasing values of the column density $N_{\rm H}$. The emission feature is the Fe Kα line at 6.4 keV. The dashed line represents the transmitted emission in objects with $\log N_{\rm H} = 24.5$, which dominates above 10 keV (from Gilli et al. 2007).

obscured AGN are crucial, as follows.

1. The cosmic X-ray background (XRB) is the integrated emission of faint extragalactic point-like sources. In particular, most of the XRB sources are AGN. The XRB intensity, especially around its peak at $\sim$30 keV, is related to the energy released by accreting SMBHs over cosmic time and X-ray background synthesis models predict that the majority of AGN is obscured by a column density larger than 10^{22} cm^{-2} (Gilli et al. 2007). Hence, Compton-thick absorption cannot be neglected in modelling the X-ray background, as they may produce up to $\sim$30% of XRB peak emission and be as abundant as Compton-thin AGN. At present, almost all of the XRB at energies below 8 keV has been resolved into discrete sources, while in the hard X-ray band above 10 keV a significant fraction of the XRB is still unresolved, not allowing to directly reveal its whole origin.

2. The formation of the initial seed BHs within the first galaxies assembled in dark matter halos remains an important open question. In addition, observations of AGN at $z > 6$ show the existence of luminous quasars with $M_{\rm BH} > 10^9$ M$_\odot$ (e.g. Mortlock

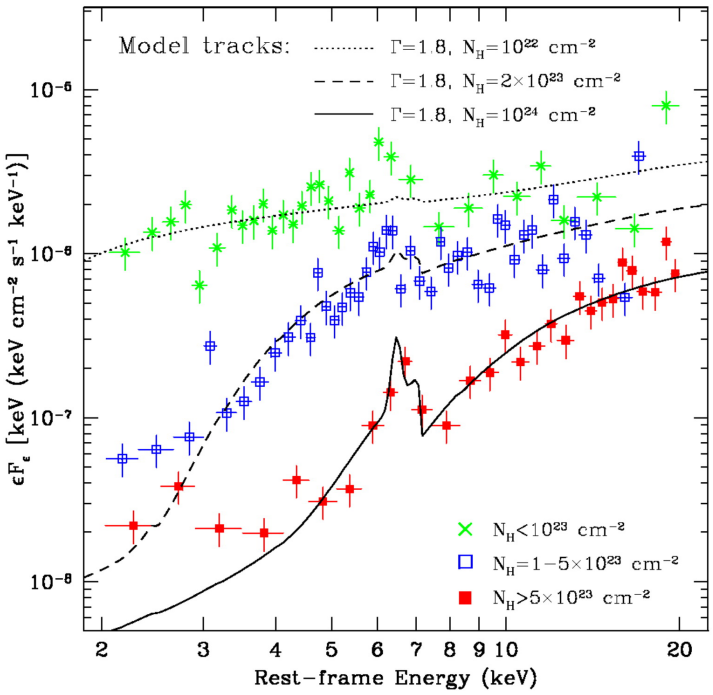

Figure 1.7: Stacked $2-20$ keV spectra for different amounts of X-ray absorption, as indicated in the legend. The spectra are normalised to the average flux density of each obscuration class (with the exception of the the top spectrum, green crosses, scaled by a factor of 2 for presentation purposes). Especially in the most obscured spectrum (red squares), the iron line and the excess of soft emission are present (from Alexander et al. 2005b).

et al. 2011) when the age of the Universe was only about 1 Gyr. Arguably, SMBHs were common immediatly after the birth of the first stars. These observational results pose one of the hardest challenges that models of seed BH formation have to deal with, i.e. how these seeds built up their masses up to the observed values in such short accretion periods. The comparison between the formation timescale and the redshift where these objects have been seen place constraints on the growth time and the accretion rate, suggesting that the majority of SMBHs must have grown rapidly in the past. There are currently three main channels of formation (Volonteri 2012 and references therein, Alexander & Hickox 2012):

- Remnants of population III stars, formed from very low-metallicity gas and characterized by masses up to a few hundreds $M_{\odot}$. The formation of such massive stars is made possible by the absence of heavy metals, otherwise atomic lines and dust would be very efficient coolants producing fragmentation of the

gas cloud. These stars can produce, in very brief timescales, BHs with masses that are roughly half their initial masses.

- Direct collapse of primordial gas clouds. In globally unstable disks of proto-galaxies, gas accumulates rapidly to the center falling on a supermassive star in such a short time ($\sim$ million years) that, after the core collapse, the newly born BH is still fed by the infalling gas. The result is a seed with mass up to $10^4 - 10^5$ $M_\odot$.

- Collisions in dense stellar clusters. In locally unstable disks, instead, a dense stellar cluster form in the central region. Collisions between stars produce a very massive object that collapses in a BH with mass similar to that of their progenitors if the initial gas is metal-poor ($M_{\rm BH} \sim 10^3$ $M_\odot$).

Once formed, the seed continues to grow by accreting gas. In order to model this growth, theory predicts that the first SMBHs accreted at rates larger than the Eddington limit, but the problem of the feedback near the BH affecting the gas supply has to be taken into account as well. Probably, the effects of feedback could be diminished by the production of collimated jets which deposit kinetic energy at large distances. As these seeds could be heavily obscured during their early phases, the quest for obscured AGN up to very high redshifts may shed light on SMBH formation, providing an observational comparison to the different models.
3. Much of the mass growth of SMBHs occurs during the heavily obscured phase; this is particularly important at high redshift, when large reservoirs of gas were available. The fuel that switches on accretion onto the central engine is expected to induce star formation activity as well. From these arguments a possible link between AGN and starburst galaxies arises, first suggested by Sanders et al. (1988). Hence, studying obscured AGN allows us to trace this symbiotic growth of active nuclei with their host galaxies (see §2).

As mentioned above, the existence of a large number of heavily obscured AGN was predicted by AGN population synthesis models to explain the X-ray background. In particular, the fraction of obscured AGN is an important quantity which characterizes the AGN population, but obscuration represents a substantial source of uncertainties in the demographic study of these objects and their evolution with redshift. The obscured AGN fraction is well constrained only in the local Universe (e.g. Burlon et al. 2011, who studied a complete sample of AGN detected by *Swift*-BAT), and a decrease with increasing luminosities has been observed up to $z \sim 3$

(e.g. Ueda et al. 2014). On the contrary, small samples of AGN are available at $z > 3$ from X-ray surveys, providing a poorly costrained fraction. In this regard, e.g., Vito et al. (2014) analyzed the obscured AGN fraction in the distant Universe collecting from different surveys a sample of X-ray selected AGN at $3 < z \lesssim 5$. They estimated the fraction of obscured AGN ($\sim 50\%$) with $\log N_{\rm H} > 23$ and found a positive evolution with z (Fig. 1.8) comparing their results with those from Burlon et al. (2011). In particular, this evolution turned out to be stronger at higher luminoisities ($\log L_{\rm X} > 44$). Moreover, a comparison with the predictions of X-ray background synthesis models provided a good agreement. A similar behaviour was found for AGN at $z > 1.7$ by Iwasawa et al. (2012). The increase of the obscured AGN fraction might be related to a larger availability of gas supply at high redshift (e.g. Carilli & Walter 2013, Bothwell et al. 2013), making the high-redshift obscured AGN population particularly interesting to study the bulk of SMBH accretion.

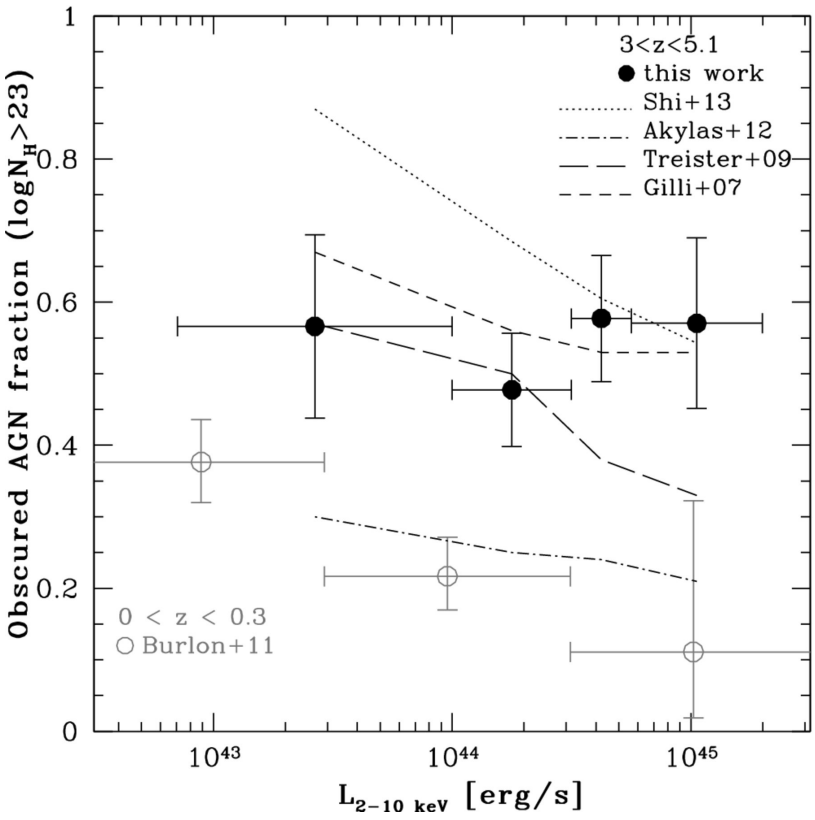

Figure 1.8: Obscured AGN fraction as a function of luminosity in the redshift range $3 < z \lesssim 5$. The value derived is 0.54 ± 0.05, compared with the X-ray background synthesis models (represented by the different lines, as indicated in the legend) and the fraction in the local Universe. This quantity shows an evolution with redshift, more remarkable at higher luminosities (from Vito et al. 2014).

1.4.1 A possible evolutionary scenario

Observations indicate that SMBHs reside at the centers of most galaxies. Scaling relations have been identified between SMBH masses and large-scale properties of their host galaxies, such as the mass (Magorrian et al. 1998) or the velocity dispersion (i.e., the $M_{\rm BH} - \sigma$ relation, Ferrarese & Merritt 2000), that suggest a direct link between the origin of galaxies and SMBHs. The tightness of this BH-spheroid mass relation suggests a joint BH-galaxy cosmic evolution, supported by indications of intense star formation phenomena coexisting with nuclear accretion. Several pieces of evidence favour the connection between the two activities: the differential evolution of the AGN population is also found for the star-forming galaxy population (the so-called downsizing, where the most massive galaxies and the most luminous AGN tend to have formed earlier, e.g. Thomas et al. 2005, La Franca et al. 2005); the redshift distribution of the most strongly star-forming galaxies traces closely that seen in the optical quasar population (Chapman et al. 2005, Wardlow et al. 2011); the peaks of the mass accretion and star-formation histories have similar redshifts (e.g. Madau et al. 1998, Delvecchio et al. 2014).

In order to fuel the BH growth, gas needs to overcome the barrier of the angular momentum. Large-scale gravitational torques could potentially remove significant amounts of angular momentum and drive the gas into the central regions of the galaxy. However, the physical processes responsible for driving the accretion are not well understood. Many mechanisms have been proposed which could explain this link, either external (galaxy mergers or interactions) or internal (gas instabilities, galaxy bars, ecc.). However, the accretion rates in quasars (i.e. high-luminosity AGN) cannot be produced easily by secular processes, which could, instead, trigger low-luminosity AGN. Powerful quasars require higher gas inflow rates and are probably triggered by gas-rich galaxy mergers, which induce sufficiently strong tidal forces (e.g. Alexander & Hickox 2012, and references therein).

One of the most popular scenarios is that proposed by Hopkins et al. (2008), who presented an evolutionary model for starbursts, quasars and spheroidal galaxies driven by mergers between gas-rich galaxies. In their picture, these phases are connected in a cosmic cycle by the same event: mergers can be responsible for triggering intense starburst activity that precedes quasar activity, so that the starburst galaxy could eventually evolve into a quasar. The evolutionary sequence is depicted in Fig. 1.9 (Hopkins et al. 2008). Disk galaxies evolve quiescently until a major merger event occurs (images (a)-(c) in Fig. 1.9). At the beginning of the merger, tidal

torques enhance weakly star formation and black hole accretion and the pair would be barely identified as a quasar. Then, massive inflows of gas able to fuel starburst activity, with intensities similar to those observed for ultraluminous IR galaxies and submillimeter galaxies, as well as rapid black hole growth are triggered during the final coalescence, when the BH is heavily obscured by gas and dust (image (d) in Fig. 1.9). During the brief blowout phase (which provides short lifetimes of $\sim 10^7$ yr for bright quasars), feedback from the black hole and supernova-driven winds begins to disperse the residual gas of the starburst activity (image (e) in Fig. 1.9). This phase is usually associated with highly dust-reddened and/or IR-luminous quasars, which constitute $\sim 20 - 40\%$ of the quasar population. When dust is removed, the system is visible as a luminous unobscured quasar and reaches its peak luminosity (image (f) in Fig. 1.9). Finally, as the remnant relaxes, star formation and quasar activity decline and the remnant evolves as an elliptical galaxy with a quiescent black hole (images (g)-(h) in Fig. 1.9). Hopkins et al. (2008) studied the merger efficiency of galaxies as a function of environment and mass ratio, and determined the characteristic mass of the dark matter halo in order to have a major merger event ($\sim 10^{12.5}$ $M_\odot$). This halo is referred to as the "small group" (image (b) in Fig. 1.9) and hosts $2 - 3$ galaxies of similar mass.

However, many of the physical properties that connect the evolutionary phases are not well understood, and the mechanism providing the trigger to fuel quasars remains uncertain. The host galaxies of up to $\sim 45\%$ of the X-ray AGN show evidence of disturbed morphologies (e.g., Kocevski et al. 2011, Silverman et al. 2011), supporting the idea that a substantial fraction of the distant AGN activity may be driven by external processes. Nevertheless, interpreting the galaxy morphology is difficult and such studies depend on signal-to-noise ratio, spatial resolution and redshift, thus suffering from potential complications. The self-regulated nature of the black hole growth in mergers explains observed correlations between the black hole mass and properties of normal galaxies, as well as the trend of obscured AGN fraction with redshift (e.g. Treister et al. 2010). In this framework obscured systems represent an earlier phase of a broad evolutionary sequence. Therefore, quasar obscuration could be an evolutionary effect rather than a geometric effect, where column densities are due to massive gas inflows required to fuel AGN activity (Hopkins et al. 2006). Probably, the unification paradigm that describes the AGN phenomenon does not hold anymore at high redshift.

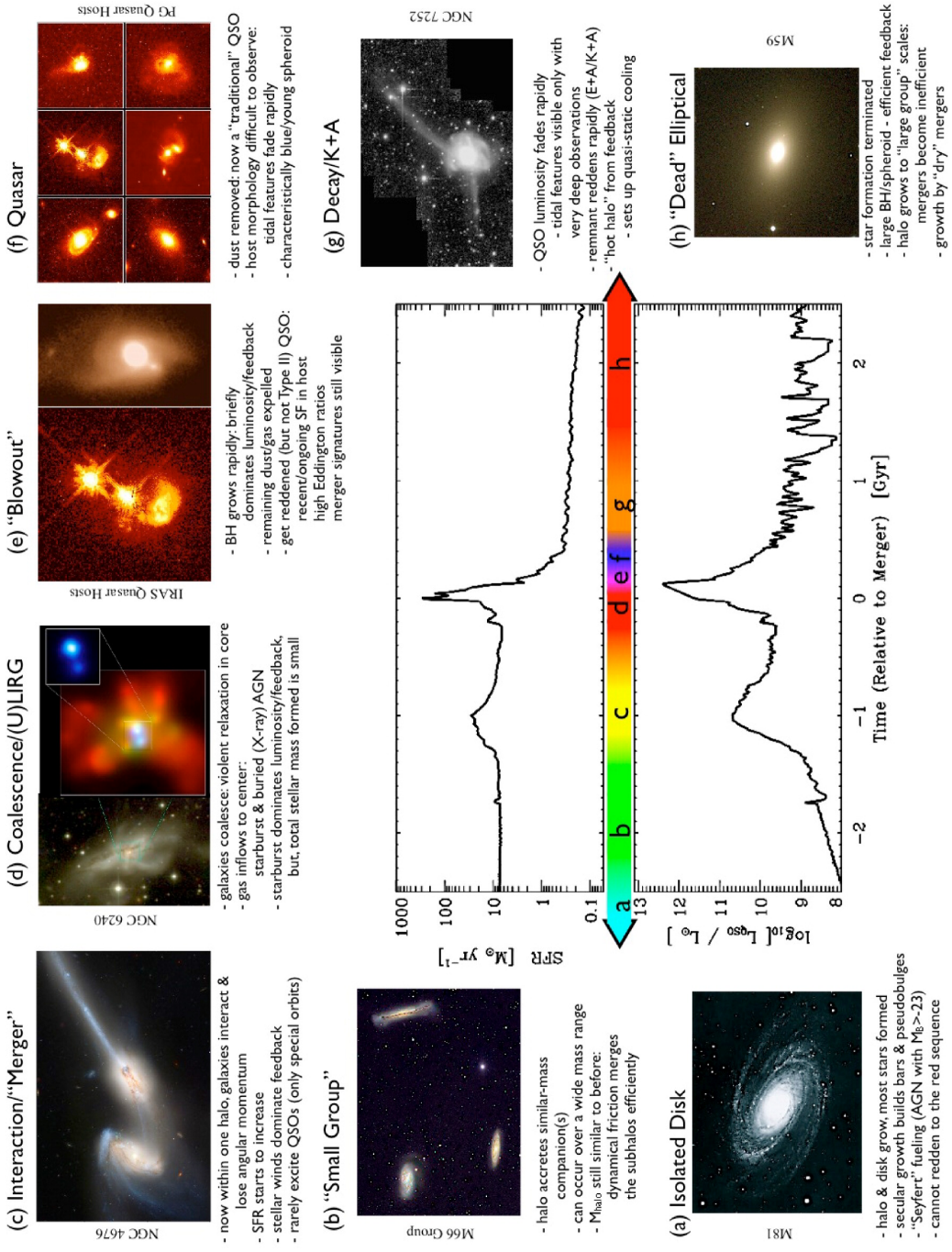

Figure 1.9: Schematic representation of the cosmic cycle that occurs after a gas-rich major merger. After the merger, the galaxy passes through starburst and quasar phases, ending up as an elliptical galaxy (from Hopkins et al. 2008).

1.5 Obscured AGN hosts

The evolutionary scenario described above matches the BH accretion phase with highly star-forming galaxies. Therefore, the analysis of obscured AGN hosts must aim at seeking sites where the most intense star formation is occurring. The most powerful starbursts at high redshift are submillimeter galaxies (SMGs), discovered as a population of very luminous galaxies at submillimeter wavelengths ($200-1000$ μm), thanks to advances in the submm detector technologies provided by the Submillimeter Common-User Bolometer Array (SCUBA) camera at the James Clerk Maxwell Telescope in the 850-μm atmospheric window (see Blain et al. 2002 for a review on these results). They are among the most luminous objects in the Universe and contribute significantly to the total cosmic star formation around $z \sim 2$. These objects are commonly detected at a median redshift $z \sim 2-3$ and defined as submm sources with flux densities $\gtrsim 1$ mJy at 850 μm, corresponding to typical infrared luminosities of $\sim 10^{12}$ $L_\odot$ and estimated star formation rates of $\sim 100-1000$ $M_\odot$ yr^{-1}. SMGs are massive objects, with stellar masses $M_* \sim 10^{11}$ $M_\odot$ or higher, and large reservoirs of cold gas, $\gtrsim 10^{10}$ $M_\odot$ (e.g. Coppin et al. 2010, Bothwell et al. 2013, Wang et al. 2013). Wider field surveys have become possible thanks to the development in IR-detector technology, including e.g. *Spitzer* and *Herschel*. These surveys have provided large numbers of dusty galaxies with properties similar to the original SCUBA population. The low-redshift companions of the high-redshift SMGs are likely the ultraluminous IR galaxies (ULIRGs), discovered in the IRAS all-sky survey at $z < 0.3$, which exhibit similar values of SFR and IR luminosity. The main sources of submm radiation from galaxies are thermal continuum emission from dust grains and line emission from atomic and molecular transitions (especially the CO rotational transitions) in the interstellar gas. In particular, observations of cold molecular gas at submillimeter wavelengths would be a useful tool to study how the cold gas feeds both star formation and accretion activity (e.g. Blain et al. 2002).

SMGs are unique objects to study the co-evolution of galaxies and their central SMBHs. Indeed, a significant fraction of X-ray detected SMGs shows AGN activity. Several studies, which matched submm observations with X-ray data, found an AGN fraction among SMGs between $\sim 20\%$ and $\sim 40\%$ (e.g. Alexander et al. 2005a,b, Laird et al. 2010, Georgantopoulos et al. 2011). However, although AGN are detected inside SMGs, they are not necessarily the main power source of the galaxy. Indeed, the bolometric output of SMGs appears to be dominated by power-

ful star formation rather than BH accretion activity. However, their large molecular gas supply can fuel both luminous star formation activity and intense BH accretion for $\sim 10^8$ yr (Alexander et al 2005a). The majority of AGN hosted in SMGs are obscured, as predicted for BHs undergoing efficient growth. The unobscured AGN luminosities suggest that the mass accretion rates are modest (~ 1 $M_\odot$ yr^{-1}), approximately an order of magnitude lower than those of coeval quasars. Alexander et al. (2005a,b), in their pioneering study on these sources, suggested that they are responsible for the crucial transition (pre-quasar) phase where BHs in massive galaxies are rapidly grown in powerful star-forming galaxy, as predicted by major merger fueling models. In SMGs hosting an active nucleus (see Fig. 1.7), estimates of the galaxy luminosities and BH masses indicate that the BH is undermassive in comparison with the host galaxy and may therefore be in an early stage of accretion that may precede the bright unobscured phase (but see also Hainline et al. 2011, who determined a lower median stellar mass for SMGs, $\sim 7 \times 10^{10}$ $M_\odot$).

Chapter 2

AGN sample and data

A crucial science goal of modern astrophysics is understanding the formation and evolution of SMBHs. A key phase of their history is the one characterized by obscured accretion at high redshift, when the BH is rapidly growing within a highly star-forming galaxy. X-ray emission produced by the AGN is a good tracer of this accretion activity, but it can be heavily depressed by passing through the obscuring material, limiting the detection of these sources at hard X-ray energies. In order to infer the cosmic history of the SMBH growth, it is necessary to identify large populations of AGN at different redshifts. In this regard, deep X-ray surveys are a very powerful tool and offer an exceptional possibility to efficiently select even low-luminosity AGN up to high redshift. Such objects are more numerous and more representative of the AGN population than the rare, highly luminous quasars found in optical and near-IR surveys. However, there is a large fraction of intrinsically luminous but heavily obscured AGN, constituting a substantial part of the SMBH growth in the Universe, that still escapes detection even in the deepest surveys.

Although X-ray observations are very sensitive to the accretion power of the AGN, a complete census of this population cannot be obtained following a single-band investigation. Indeed, a multi-wavelength approach is likely to be the best way to get a complete view of these class of sources. Moreover, the growing phase of SMBHs is intimately connected with the star formation activity in their host galaxies, as large amounts of gas can induce both obscured accretion and star formation (Vignali 2014). Hence, fully characterizing the host-galaxy properties by measuring e.g. star-formation rates, stellar masses and luminosities can provide additional information about the scenario of co-evolution between galaxies and SMBHs.

Our study focused on the *Chandra* Deep Field South (CDF-S) data, as they

provide the best X-ray spectral information for distant AGN currently available. We exploited the extraordinary multiwavelength coverage in this field as well, in order to obtain a picture as comprehensive as possible of our targets.

In this chapter we will describe the X-ray/multiwavelength approach followed to conduct our study, along with the used datasets. Then, we will present the criteria adopted to select the obscured AGN sample and the main steps of our analysis.

2.1 Studying obscured AGN in the X-ray band

X-ray emission is a solid tracer of the accretion activity of SMBHs, and the X-ray study of the AGN population is a reliable method to perform a "pure" analysis of the central engine. The advantages of approaching AGN through X-rays are numerous (see Brandt & Alexander 2015 for a review). Looking at higher energies means looking closer to the SMBH; indeed the intrinsic X-ray emission mostly originates from its surroundings. As explained in § 1.4, this emission may then interact with matter through photoelectric absorption, Compton reflection and scattering, producing a change in the intrinsic spectrum. However, high energy X-rays are capable of piercing substantial amount of matter with high column densities ($N_{\rm H} = 10^{21} - 10^{24}$ cm^{-2}), suffering from reduced absorption bias and making the directly transmitted emission observable in case of deep X-ray data. Even in the Compton-thick regime ($N_{\rm H} > 1.5 \times 10^{24}$ cm^{-2}), when the transmission of X-ray photons becomes impossible below 10 keV, the AGN emission can be investigated by means of X-rays reflected by neutral material, although such emission is much fainter (e.g. Comastri 2004). This penetrating capability is a fundamental feature of X-rays, since the majority of AGN in the Universe are subject to significant intrinsic obscuration. In particular, such benefit turns out to be very useful when objects at increasing redshift are studied in a fixed observed-frame band, as it is possible to probe higher rest-frame energies associated with increasingly penetrating X-rays. Another relevant advantage of X-ray studies is the presence of distinctive characteristics in the AGN spectrum which can facilitate their identification (such as the photoelectric cut-off, the Compton reflection continuum and the fluorescent emission line). An accurate analysis of these features allows us to derive valuable information about these systems (e.g. intrinsic luminosity, obscuration level and nuclear geometry). Moreover, X-rays have low dilution by emission from stellar processes in the host galaxy, thus providing excellent contrast between SMBH accretion light and starlight. Again, this aspect is especially important at high redshift where we cannot spatially resolve

the AGN from the host galaxy emission (e.g. Moran et al. 2002).

The investigation through X-rays allows us to reveal AGN in galaxies where the accretion activity in other wavebands is either obscured or overwhelmed by host galaxy light. Thanks to X-ray surveys, which have now achieved sufficient sensitivity and sky coverage, a systematic search for heavily obscured AGN is possible. In particular, an increasing obscured AGN fraction as a function of redshift has been observed (e.g., Treister et al. 2006, Iwasawa et al. 2012, Vito et al. 2014, see also Fig. 1.8), arguably due to the larger supply of cold gas and dust at earlier cosmic times. In this regard, X-ray surveys of distant AGN are capable of providing a deep understanding about when, where and how SMBHs grew, and about possible connections between AGN activity and star formation, when supported by other multiwavelength observations (Brandt & Alexander 2015). Several X-ray survey projects have been conducted over the years, allowing the coverage of a large part of the accessible sensitivity vs. solid angle space, providing a wide view of the AGN population in the distant Universe. An ideal survey should have the combination of both large area and sensitivity sufficient to detect the faintest sources. However, as shown in Fig. 2.1, deep surveys are able to probe intrinsically less luminous and more typical objects than wide-field ones, but are limited to a small area of the sky. On the contrary, wide-field survey can probe larger areas, but at the same time are shallower and sensitive to luminous and rare sources.

Surveys carried out with the NASA's *Chandra* X-ray Observatory and the ESA's XMM-*Newton* are currently sources of invaluable information for most of the present studies. They allow X-ray spectroscopic imaging over broad bandpasses ($0.3-8$ keV and $0.2-10$ keV, respectively) and over respectable fields of view (290 arcmin^2 for *Chandra* ACIS-I and 720 arcmin^2 for XMM-*Newton* EPIC-pn). Moreover, the imaging Point Spread Function is excellent for *Chandra* and good for XMM-*Newton* (on-axis half-power diameter of $0.84''$ and $15''$, respectively). These telescopes have been operating for the last 15 years and have already covered a significant portion of the accessible flux vs. solid angle plane (Fig. 2.1), from deep pencil-beam surveys (i.e. limited to a small solid angle) to shallow wide-area ones. In addition, they detected very large source samples (about 5×10^5 unique X-ray sources) over 1000 deg^2 of the sky. The identification and characterization of heavily obscured AGN is going to improve over the next years thanks to *Nu*STAR, which is exploring the distant Universe up to a few tens of keV and, on longer timescales (2028), *Athena*, which will provide an unprecedented comprehension of the accretion history of SMBHs at $z > 6$.

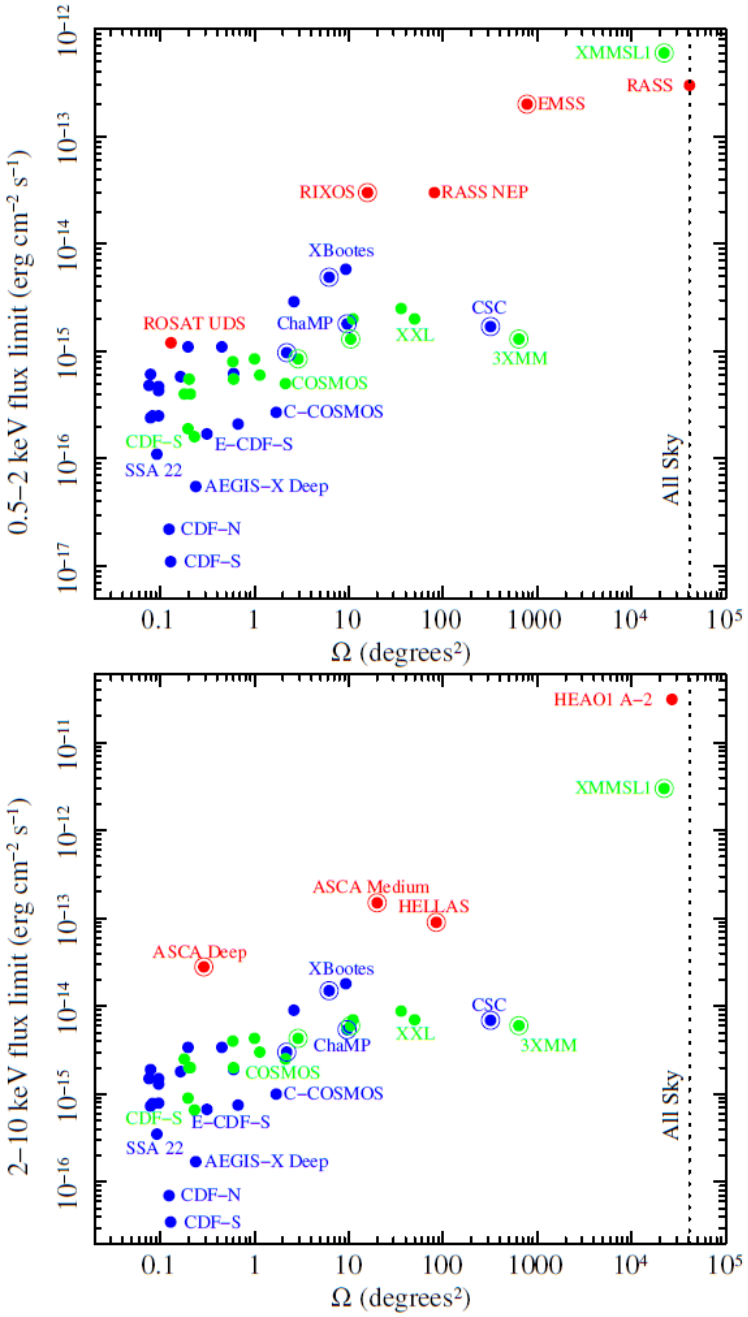

Figure 2.1: Plot of solid angle of sky coverage vs. sensitivity in both the $0.5-2$ keV (*top panel*) and $2-10$ keV bands (*bottom panel*) for different surveys carried out with *Chandra* (blue) and XMM-*Newton* (green). A few surveys from previous X-ray missions are shown in red, for comparison. The circles around some of the points indicate serendipitous surveys. The vertical dotted line shows the solid angle for the whole sky. Image taken from Brandt & Alexander (2015).

2.1.1 The Chandra Deep Field South

Chandra has brought great advances especially for what concerns spatial and spectral resolution, and has considerably improved the ability to observe the X-ray emission from AGN, due to the broad bandpass, the moderately large field of view, as well as its unmatched angular resolution and the low background (Brandt & Alexander 2009). Indeed, even the deepest observations performed to date do not suffer from significant source confusion in the central portion of the field of view.

The *Chandra* telescope It consists of four nested grazing-incidence Wolter-1 X-ray mirror pairs, called the High Resolution Mirror Assembly (HRMA). The largest mirror has a diameter of 1.2 m and a focal length of 10 m. The focal plane houses two instruments: the High Resolution Camera (HRC) and the Advanced CCD Imaging Spectrometer (ACIS). The former consists of a microchannel plate instrument used for imaging. The latter is capable of acquiring simultaneously high-resolution images and moderate resolution spectra. It is comprised of a 2×2 CCD array (ACIS-I) designed for imaging, and a 1×6 CCD array (ACIS-S) used either for imaging or for high-resolution spectroscopy, in conjunction with either the High Energy Transmission Grating (HETG) or the Low Energy Transmission Grating (LETG). Each 1024×1024 pixel CCD has a pixel size of $\sim 0.492''$. The Point Spread Function (PSF) and the Encircled Energy Fraction[1] (EEF), at a given radius, depend on off-axis angle and energy. In particular, the PSF broadens and the EEF decreases as the off-axis angle increases, because of mirror aberrations, and as the X-ray energy increases, due to increasing difficulty in focusing higher energy X-rays. An important characteristic that describes the ability of a telescope to collect X-ray photons is the effective area. It depends on different instrumental effects (regarding the system mirros+detectors) such as the vignetting, i.e. the fractional loss of detected photons which increases with off-axis angle and energy (Fig. 2.2). Therefore, the best performances are on-axis, where the PSF is very sharp, with a Full Width Half Maximum (FWHM) of $\sim 0.5''$. Thanks to the high spatial resolution, *Chandra* is suitable for observing very faint point-sources.

The deepest X-ray surveys with *Chandra* currently available in extragalactic fields are the *Chandra* Deep Fields, namely the 4Ms *Chandra* Deep Field-South

[1]It is the two dimensional integral of the PSF, defined as the percentage of photons for a given energy, within a certain radius.

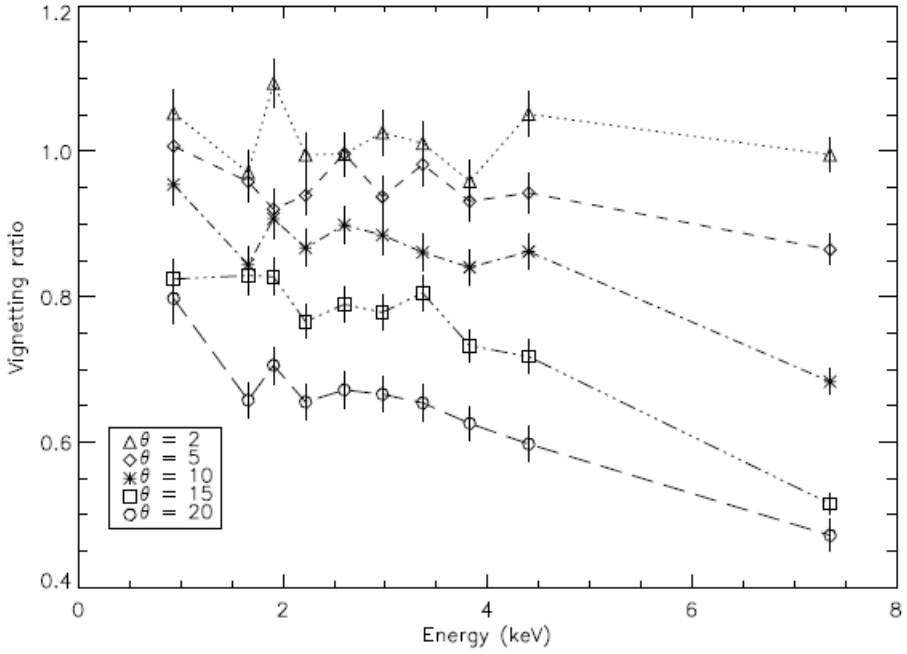

Figure 2.2: Vignetting (defined as the ratio of off-axis to on-axis effective area) as a function of energy, for different off-axis angles in arcmin. Image taken from *The Chandra Proposers' Observatory Guide* (http://cxc.harvard.edu/proposer/POG/).

(CDF-S, Xue et al. 2011) and the 2Ms *Chandra* Deep Field-North (CDF-N, Alexander et al. 2003). Thanks to these two surveys, a huge amount of reliable identified AGN has been found so far, with an AGN source density on the sky of about 10000 sources per deg^2. In particular, the maximum sensitivity is reached in the central regions of the CDF-S, namely $\sim 3.2 \times 10^{-17}/9.1 \times 10^{-18}/5.5 \times 10^{-17}$ erg cm^{-2} s^{-1} in the $0.5-8.0/0.5-2.0/2.0-8.0$ keV band. Its exposure has recently been extended to 7Ms[2], making the CDF-S a legacy field for the forthcoming years and the deepest view of the distant Universe at high energy. The first 2Ms exposure consisted of 23 observations performed between October 1999 and November 2007 (Luo et al. 2008), the second 2Ms exposure comprised 31 observations taken between March 2010 and July 2010 (Xue et al. 2011), while between October 2014 and March 2016 the last 3Ms exposure were carried out with 49 observations. All 103 observations were performed by using the ACIS-I instrument (CCDs I0-I3), optimized for imaging wide fields (with a field of view of $16'.9 \times 16'.9 = 285.6$ arcmin^2). The entire CDF-S covers an area of 464.5 arcmin^2, which is larger than the ACIS-I field of view, due to

[2]Although we have used the 7Ms dataset to extract X-ray spectra, we refer to the 4Ms catalog, as the 7Ms one has not been published yet (Luo et al., in preparation).

the variation of the aimpoints and roll angles between the observations. The average aimpoint, obtained by weighting the values of the individual observations with the corresponding exposure time, is $\alpha = 03^{\rm h}32^{\rm m}28^{\rm s}.06$, $\delta = -27°48'26''.4$, where α and δ are the J2000 right ascension and declination. Fig. 2.3 shows a full and an expanded "false-color" image of the 4Ms CDF-S.

The data products of this survey are public and stored in the *Chandra* Data Archive[3]. A full description of the procedure of data reduction and production of the main source catalog can be found in Xue et al. (2011).

2.2 Multiwavelength study of obscured AGN

Although X-ray surveys allow a very efficient study of obscured AGN, the determination of the accretion history of SMBHs and its relation to galaxy evolution cannot be achieved using X-ray data alone. As suggested by McLeod (1996), "although most of the attention given to AGN is concentrated on the *N*, there are compelling reasons to understand the *G*". The central engine and the host galaxy influence each other, and investigating these connections could provide important clues for achieving a better understanding of the galaxy-BH co-evolution. Therefore, in order to study the hosts, a multiwavelength approach is necessary. First of all, this method is used to identify AGN candidates missed by the X-ray selection technique. Indeed, the AGN primary continuum is reprocessed by gas and dust in the nucleus and comes out at other wavelenghts, e.g. the disc emission is thermally reprocessed by the torus in the mid-IR regime. Secondly, the characterization of the detected X-ray sources, by means of multiwavelength photometric data and/or spectroscopic observations, is crucial to investigate their nature and measure their properties. This kind of observations allows us to study either the AGN host galaxies, if the AGN emission is obscured, or the accretion physics of the central nucleus over a broad spectral range, if the AGN emission overwhelms the stellar emission of the host.

Thanks to the multiwavelength surveys in the CDF-S we were able to extend our analysis to a broad range of wavelengths, and to build UV-to-FIR spectral energy distributions (SEDs) for the sources using of a large set of photometric data. Broad-band SEDs are our primary source of information about the properties of unresolved galaxies and SED fitting models and procedures improved significantly

[3]http://cxc.harvard.edu/cda/

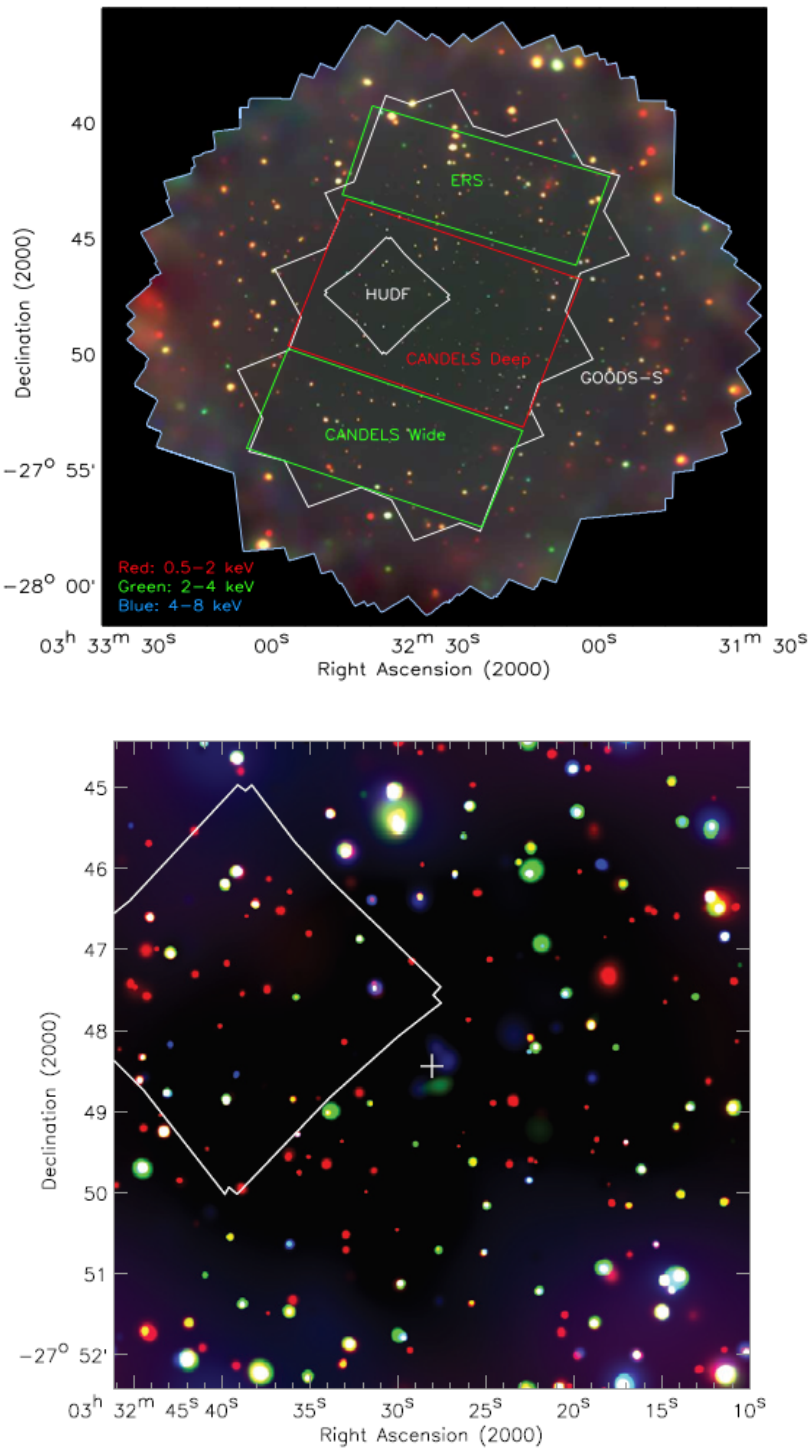

Figure 2.3: *Top panel*: *Chandra* "false-color" image of the 4Ms CDF-S, obtained by combining images in the $0.5-2.0$ keV (red), $2-4$ keV (green) and $4-8$ keV (blue) bands as given in the legend. The GOOD-S, CANDELS (see § 2.2.1), ERS (*HST* Early Release Science observations in the GOODS-S field) and HUDF (*Hubble* Ultra Deep Field) regions are marked. *Bottom panel*: Expanded view of the central $8' \times 8'$ region of the CDF-S. Here, the faint sources are more visible thanks to a different contrast ratio. Note that the apparent smaller size and lower brightness of sources near the center of the field is due to the smaller size of the on-axis PSF (from Xue et al. 2011).

over the years. By means of a detailed analysis of the SED it is possible to derive several physical parameters of both the host galaxy and the AGN through a decomposition in the contributions given by the different components which participate in the overall emission, each dominating at different wavelengths. The bulk of the emission is produced at UV-submillimeter wavelengths. The stellar emission peaks at UV-NIR wavelengths and corresponds to the radiation emitted by populations of stars over a range of masses and ages. Their intrinsic emission is modified by the presence of dust, particularly abundant in regions of star formation which are optically thick to short-wavelength (UV-optical) radiation. The dust re-radiates the absorbed starlight in the FIR producing a prominent peak at $\lambda \sim 100$ μm. The hot dust near the AGN, instead, emits mostly in the MIR regime. Over the bandpasses where the AGN primary emission is obscured (i.e. UV-NIR), measurements of the host galaxy properties without significant contamination from the AGN are possible. Moreover, from the FIR emission, the gas and dust content of the host can be estimated, giving the opportunity to study the components (i.e., gas and dust) that may have a leading role in the still unclear co-evolutionary scenario.

2.2.1 Broad-band photometry in the CDF-S

The deep X-ray survey in the CDF-S is complemented by several observing projects using different facilities. We can rely upon an unprecedented coordination between observatories across the whole electromagnetic spectrum to cover this region of the sky as deeply as possible at all accessible wavelengths. This field possesses data from diverse telescopes, such as *Hubble Space Telescope*, *Spitzer*, *Herschel*, and other observatories both in space and on the ground. Their joint effort revealed, during the last decade, a complex interplay between galaxy mergers, star formation and black hole accretion over cosmic time, introducing the new concept of galaxy-BH co-evolution. In addition, the recent contribution given by the Atacama Large Millimeter Array (ALMA), thanks to the high spatial resolution, has become fundamental and will provide extraordinary improvements in this field in the next few years with important implications for local as well as very high redshift AGN.

The Cosmic Assembly Near-IR Deep Extragalactic Legacy Survey (CANDELS) fields (Grogin et al. 2011), designed to document the first galaxy evolution from $z \sim 8$ to 1.5 via deep imaging of more than 250,000 galaxies, arguably provides the best data to identify and study distant AGN and their heavily obscured counterparts. One of the primary goals of this survey is conducting the deepest census

of active galaxies at $z > 2$ selected by X-ray, IR and optical spectra as well as testing models for the co-evolution of galaxies and BHs using demographic data on host characteristics, with particular attention to their structural and morphological properties. This requires, e.g., measuring accurate radii and axial ratios, classifying the morphological type or identifying merger-induced distortions. Moreover, it is necessary to determine redshifts, SFRs, and stellar masses from broadband SEDs as well, in order to connect the active BH accretion phase to highly star-forming phases which produce ultra-luminous IR and submillimeter galaxies.

This observing program targets five distinct fields at two different depths, distinguishing between the deep portion called CANDELS/Deep and the shallow one called CANDELS/Wide. We focus on the Great Observatories Origins Deep Survey South field (GOODS-S; Giavalisco et al. 2004), which is a region of $10' \times 16'$ in size within the CDF-S centered at $\alpha_{\rm J2000} = 03^{\rm h}32^{\rm m}30^{\rm s}$ and $\delta_{\rm J2000} = -27°48'20''$. It has been imaged with the major facilities, providing a wide combination of multi-epoch data available in several bands:

- optical imaging with *Hubble*/ACS in the B, V, i and z-bands;
- optical/near-IR observations with the Subaru Suprime-Cam Intermediate Band Filters;
- observations in the mid-IR in the *Spitzer*/IRAC and MIPS bands;
- U-band imaging with VIMOS as well as near-IR imaging in the Y-band with HAWK-I and in the J, H and K-bands with ISAAC on the *Very Large Telescope*;
- submillimeter observations taken with LABOCA on the *Apex* telescope and SCUBA on the James Clerk Maxwell Telescope.

Finally, the GOODS-S field has been observed with *Hubble*/WFC3 for the CANDELS survey through multiple exposures from October 2010 to February 2012. There are both the Wide and the Deep exposures in the GOOD-S field. In particular, the CANDELS/Deep field consists of a rectangular region of $\sim 6'.8 \times 10'$ in the central portion of the GOOD-S field (the different fields are marked in Fig. 2.3). Later, the field has also been imaged in the far-IR in the *Herschel*/PACS and SPIRE bands. Moreover, ALMA observations are available for some sources in this field. We used photometric data taken from the Rainbow Cosmological Surveys

Database[4]. Table 2.2 provides a summary of the photometry used, listing the various filters and corresponding instrument, observational facility, effective wavelength and effective width.

2.3 Sample selection

In order to select our sample, we searched for X-ray selected AGN in the CDF-S which satisfy the following requirements:

- secure spectroscopic redshift, in order to avoid the large photometric redshift uncertainties which propagate on the different measurements;
- $z_{\rm spec} > 2.5$, to find a compromise between the increasing gas supply in the host galaxy with redshift and the sample size;
- narrow-line AGN, i.e. objects classified as optical type-2 AGN (see Fig. 2.4 for the optical spectra), in order to study the galaxy properties without suffering from a strong AGN contamination;
- heavily obscured objects, with $\log N_{\rm H} > 23$, in order to trace the most obscured phase of AGN and to match it with the star-forming phase of the host galaxy;
- good *Herschel* FIR detections at $\lambda_{\rm obs} \geq 100$ μm, in order to constrain the emission peak produced by the cold dust heated by starburst activity and, as a result, to obtain a reliable estimate of the IR luminosity and the SFR.

We combined targets from the sample of Vito et al. (2013), who analyzed the Chandra X-ray spectra of all AGN at $z > 3$ using the 4Ms exposure of the CDF-S, and from the sample of Rigopoulou et al. (2009) who observed, with SCUBA, eight heavily obscured AGN at $z = 1.1-3.7$ discovered in the 1Ms exposure of the CDF-S. We found a total of 6 X-ray sources, whose properties are summarized in Table 2.1. Three of them are well known heavily obscured QSOs individually studied over the years: XID262 was studied by Manieri et al. (2005), who presented a complete SED analysis; XID412 is the first high-z Compton-thick QSO discovered in the CDF-S by Norman et al. (2002) and studied by Comastri et al. (2011) in the 3.3Ms XMM-*Newton* survey in the CDF-S; XID403 is a distant QSO hosted by a luminous SMG,

[4]http://rainbowx.fis.ucm.es/Rainbow_navigator_public/, operated by the Universidad Complutende de Madrid (UCM), partnered with the University of California Observatories at Santa Cruz (UCO/Lick,UCSC).

whose sub-mm properties were analyzed by, e.g., Coppin et al. (2010), De Breuck et al. (2014) as well as Gilli et al. (2014), who presented a complete SED and X-ray spectral analysis. The three remaining less studied objects, XID34, XID546 and XID490, are known since the 1Ms observation of the CDF-S (Szokoly et al. 2004).

The sources XID262, XID412, XID490, and XID546 are in the CANDELS/Deep portion of the CDF-S, while the source XID403 lies in the CANDELS/Wide area. As for XID34, it is outside the CANDELS field, therefore we used the MUSYC catalog to characterize the broad-band properties of this source.

Clearly, our sample is not complete. We stress that the sample selection was carried out on the 4Ms catalog, although the X-ray spectral analysis was performed on the 7Ms dataset. Hence, in the updated 7Ms catalog (Luo et al., in preparation), new sources that match our selection criteria will likely emerge.

XID (a)	CID (b)	RA (c)	DEC (d)	$z_{\rm spec}$ (e)
34	326[1]	$03^{\rm h}31^{\rm m}51^{\rm s}.95$	$-27°53'27''.2$	2.94
262	5479	$03^{\rm h}32^{\rm m}18^{\rm s}.85$	$-27°51'35''.7$	3.66
403	273	$03^{\rm h}32^{\rm m}29^{\rm s}.27$	$-27°56'19''.8$	4.755
412	6294	$03^{\rm h}32^{\rm m}29^{\rm s}.86$	$-27°51'6''.1$	3.7
490	9834	$03^{\rm h}32^{\rm m}35^{\rm s}.72$	$-27°49'16''.4$	2.578
546	10578	$03^{\rm h}32^{\rm m}39^{\rm s}.68$	$-27°48'51''.1$	3.064

Table 2.1: AGN sample summary. $^{(a)}$ Source identification number in the 4Ms CDF-S catalog of Xue et al. (2011); $^{(b)}$ CANDELS identification number; $^{(c)}$ J2000 right ascension and $^{(d)}$ declination; $^{(e)}$ spectroscopic redshift. [1] ID from GEMS (Haussler et al. 2007).

2.4 The analysis

We studied the sample of AGN by combining the X-ray and the multiwavelength approaches described. Hence, the crucial steps of the method adopted for our analysis can be summarized as follows:

1. We used the publicly available 7Ms *Chandra* data to perform an X-ray study of the active nucleus by analyzing the spectra of the sources, obtained by

summing the spectra extracted from the individual observations. Therefore, we were able to determine important physical parameters, e.g. the obscuring column density $N_{\rm H}$ and therefore the intrinsic luminosity in the $2-10$ keV band, as well as put constraints on spectral features, such as the iron emission line.

2. We combined the broad-band photometry (from UV to FIR) to build up the whole SEDs of our targets. Therefore, by means of an SED decomposition technique, we characterized both the host galaxy and the AGN deriving the stellar mass, the SFR, the FIR luminosity and the AGN bolometric luminosity.

3. Then, following the recent work of Scoville et al. (2016), we measured the source luminosity at 850 μm rest-frame which is a good proxy to derive the dust mass and, in turn, the gas mass (dominated by the molecular component) of the ISM in the host.

4. In order to estimate the column density of the host ISM towards the nucleus, we assessed the source size by using either the dust half-light radius, when available from ALMA observations, or the stellar half-light radius, and then adopted a very simple geometric model for the obscuring matter.

5. Finally, we compared this value with the X-ray absorption to verify whether the ISM in the host galaxy is able to contribute significantly to the absorption measured from the X-rays.

The details of each step will be explained extensively in the following chapters.

Throughout this thesis a ΛCDM cosmology with $\Omega_{\rm M} = 0.3$, $\Omega_{\Lambda} = 0.7$ and $\rm H_0 = 70$ km s^{-1} Mpc^{-1} is assumed.

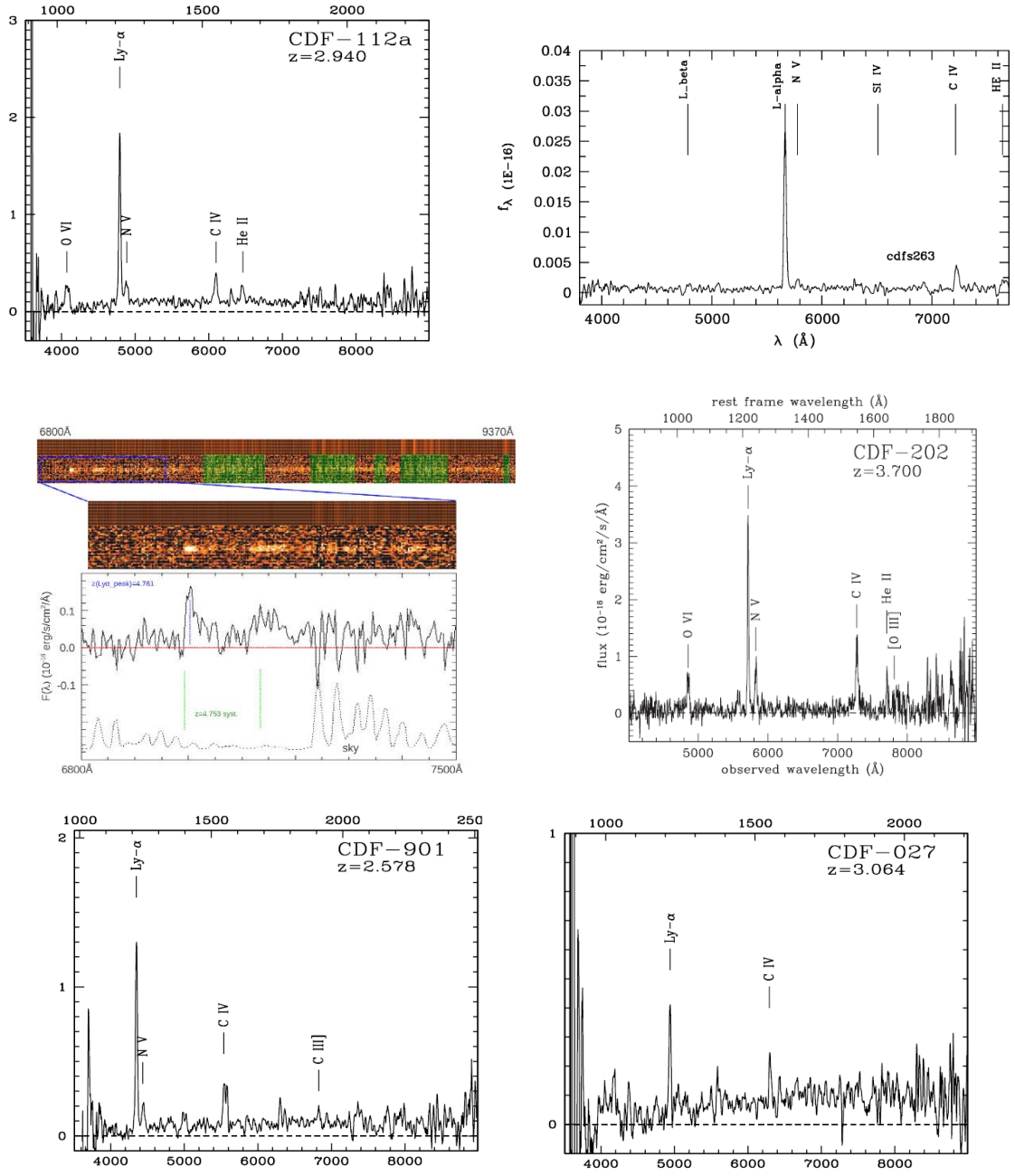

Figure 2.4: *From top left to right bottom*: optical spectra of sources XID34, XID262, XID403, XID412, XID490, XID546. The spectra are taken from Norman et al. (2002), Szokoly et al. (2004), Mainieri et al. (2005) and Gilli et al. (2014). The "CDF-" IDs within the figures refer to the 1Ms source catalog (Giacconi et al. 2002). For the source XID403 (*second panel on the left*) the two-dimensional spectrum from 6800 to 9400 Å is shown at the top of the figure, where the regions affected by intense sky emission lines are indicated by the shaded green areas. The middle and bottom of the figure show a zoom of the spectrum between 6800 and 7500 Å (blue dotted rectangle). The green vertical dotted lines mark the wavelength of the Lyα and Nv at the systemic redshift.

Filter ID	Instrument	Obs. Facility	$\lambda_{\rm eff}$ Å	$W_{\rm eff}$ Å
VIMOS.U	VIMOS	*VLT*	3765	376
IA427	SuprimeCam	*Subaru*	4260	196
F435W	ACS	*HST*	4333	800
IA464	SuprimeCam	*Subaru*	4633	214
IA484	SuprimeCam	*Subaru*	4848	222
IA505	SuprimeCam	*Subaru*	5061	226
IA527	SuprimeCam	*Subaru*	5260	246
IA574	SuprimeCam	*Subaru*	5764	267
F606W	ACS	*HST*	5810	1777
IA624	SuprimeCam	*Subaru*	6232	294
IA679	SuprimeCam	*Subaru*	6782	328
IA709	SuprimeCam	*Subaru*	7074	310
IA738	SuprimeCam	*Subaru*	7360	313
F775W	ACS	*HST*	7652	1377
IA767	SuprimeCam	*Subaru*	7681	335
F814W	ACS	*HST*	7985	1877
IA856	SuprimeCam	*Subaru*	8565	335
F850LP	ACS	*HST*	9009	1325
F098M	WFC3	*HST*	9802	1569
HAWKI.Y	HAWKI	*VLT*	10172	1016
F105W	WFC3	HST	10365	2649
F125W	WFC3	HST	12305	2845
HAWKI.J	HAWKI	*VLT*	12522	1524
F140W	WFC3	*HST*	13645	3839
F160W	WFC3	*HST*	15236	2682
HAWKI.Ks	HAWKI	*VLT*	21323	3249
ISAAC.Ks	ISAAC	*VLT*	21522	2719
IRAC.1	IRAC	*Spitzer*	35075	6836
IRAC.2	IRAC	*Spitzer*	44366	8649
IRAC.3	IRAC	*Spitzer*	56281	12561
IRAC.4	IRAC	*Spitzer*	75892	25289
MIPS.24	MIPS	*Spitzer*	232096	52963
PACS.70	PACS	*Herschel*	689247	214149
PACS.110	PACS	*Herschel*	979036	312860
PACS.170	PACS	*Herschel*	1539439	697595
SPIRE.250	SPIRE	*Herschel*	2428218	676155
SPIRE.350	SPIRE	*Herschel*	3408914	957560
SPIRE.500	SPIRE	*Herschel*	4822548	1856721

Table 2.2: Photometry summary. For each filter we provide the corresponding instrument, observational facility, effective wavelength and effective width. Each target has photometric datapoints for a certain subgroup of this set of filters.

Chapter 3

X-ray spectral analysis

X-ray analysis is likely to be the most efficient way to study the accretion onto SMBHs. However, phases of intense growth in AGN are coupled with heavy obscuration, which challenges our attempt to identify and investigate them. Although X-ray emission from heavily obscured AGN suffers from photoelectric absorption at low energy, the high-energy radiation can penetrate large amounts of gas and dust without significant absorption, being, in any case, depressed because of Compton scattering. This is true especially at high redshift, when the reservoirs of available gas were larger. To detect these sources with reasonable statistics, we have to exploit X-ray data provided by deep fields. Then, through the analysis of X-ray spectra, we are able to gather information about the accretion properties of AGN, such as the obscuring column density, the intrinsic luminosity and the emission line features. X-ray spectral analysis is a fundamental practice in this kind of study, and requires some preliminary steps which can be outlined as follows: first of all, the source and background extraction regions need to be chosen; secondly, the source and background spectra have to be extracted; finally, they are summed and grouped in order to obtain a better statistics in each spectral bin. Once the final spectra have been produced, it is possible to analyze them by means of proper models and to derive important physical quantities.

In this chapter the main steps of the spectral extraction will be described, along with the spectral models used to perform the X-ray spectral analysis of our sources. Lastly, spectra and best-fit parameters will be presented and discussed.

3.1 X-ray spectral extractions

Starting from the *Chandra* data, we need to extract and combine X-ray spectra from individual observations in order to perform the spectral analysis. The *Chandra* data products for each of the 103 observations of the 7Ms dataset publicly available were used. As individual observations depend on off-axis angle and roll-angle, sources lying at the edges of the field could be outside the field of view of some observations. In particular, concerning our sample, only two sources (XID34 and XID403) suffer from this problem; therefore we considered those observations where the source is within the field of view. As a first step, source extraction regions were chosen based on the coordinates of the 4Ms *Chandra* catalog (Xue et al. 2011), as it was the only available during our spectral analysis. Instead, the respective backgrounds were taken from nearby source-free regions in the full 7Ms exposure image. Images were inspected by means of the SAOImage DS9 application.

Depending on the source position in the field of view, some important effects need to be taken into account: the PSF depends on off-axis angle and energy, specifically it broadens and distorts as the off-axis angle and the energy increase (Fig. 3.1); furthermore, faint sources require smaller radii than bright ones, in order to include a low number of background counts and increase the signal-to-noise ratio. In spite of this distortion effect, source regions are always circular but it was verified that most of the counts were included. The choice of the extraction radii was carried out considering the effects mentioned above and the relation between the off-axis angle and the encircled energy fraction radius, checking that different values do not affect our spectra significantly. Off-axis angles of the sample are in the range $1.9 - 9.4$ arcmin (see Table 3.1), therefore the selected extraction radii are between 2.3 and 7 arcsec. As far as the background regions are concerned, we chose two regions for each source, usually an annulus centered at the source position and a circle. When there were contaminations by other sources close to the considered one or when the source was near the edges of the field, two circular regions were selected. Additionally, in order to avoid contaminations by the source itself, the background regions were defined outside the radius corresponding to an Encircled Energy Fraction larger than 95%, according to Fig. 3.1. The same regions were used for all observations. Moreover, the background spectrum was extracted from regions with an area larger than the extraction region of the corresponding source, in order to ensure a good sampling of the background itself. However, the final spectrum is "normalized" accounting for the different areas.

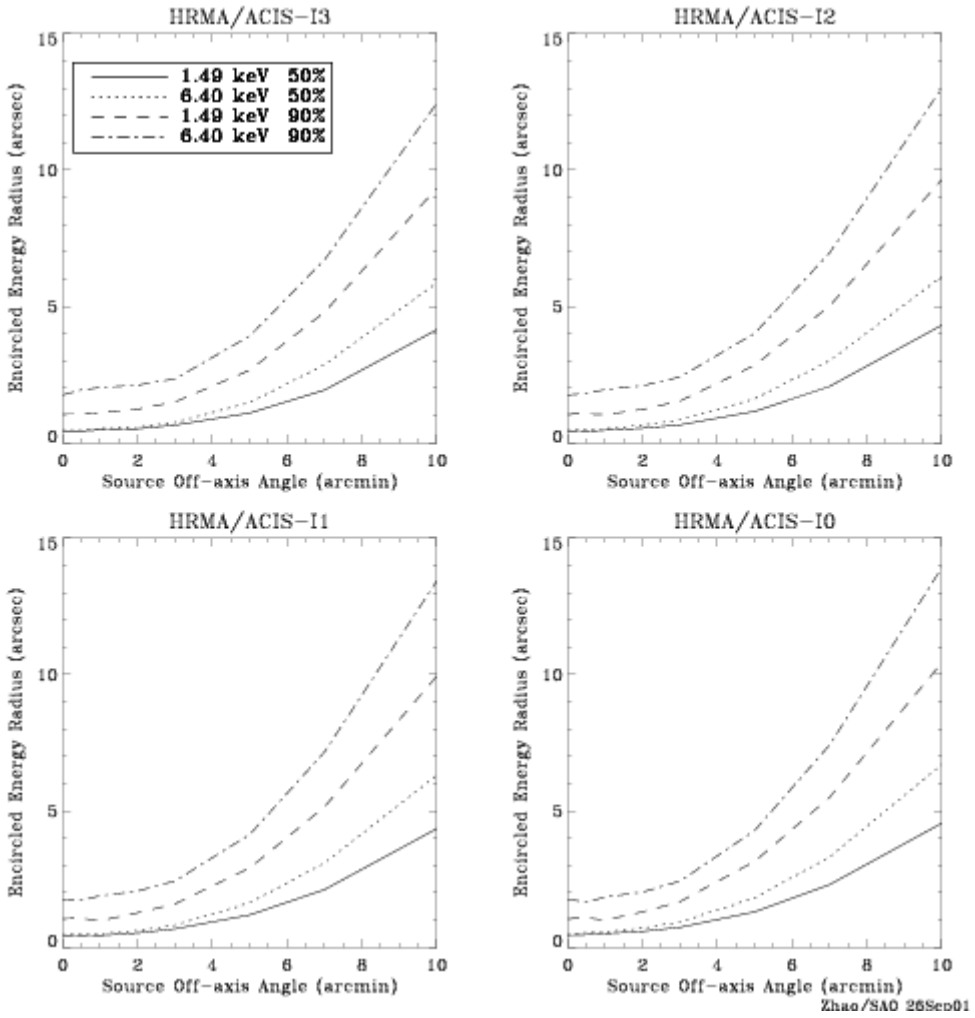

Figure 3.1: Encircled energy radius for the four ACIS-I chips. The different curves refer to the trend of the radius enclosing 50% and 90% of the power at 1.49 and 6.40 keV. Off-axis sources need larger radii in order to encircle the same energy fraction as on-axis ones; this effect is more remarkable at higher energies (figure taken from *The Chandra Proposers' Observatory Guide*, http://cxc.harvard.edu/proposer/POG/).

The spectra extrated from the individual observations provide the number of counts collected in each energy channel. Therefore, to produce the final observed spectrum, we need to match each channel with the corresponding energy, as well as accounting for the instrumental response. The input spectrum is, thus, coupled with two essential response matrix files: the Auxiliary Response File (ARF), which contains information about the combined telescope/filter/detector areas (i.e. the effective area) and the quantum efficiency (QE) as a function of energy, corresponding to the efficiency of the instrument in revealing photons; the Redistribution Matrix File (RMF), which associates each instrument channel with the equivalent photon energy, accounting for the spread of the observed counts due to the detector resolution. The result is a spectrum convolved with the telescope effective area and detector efficiencies as a function of energy. Moreover, as the number of counts in each channel can be low, several channels are grouped together in spectral bins in order to improve the statistics. Final spectra were obtained by means of the *Chandra* Interactive Analysis of Observations (CIAO) software and, in detail, the following tools, which perform the steps described above, have been used: firstly, source and background spectra were created for each observation by the *specextract* tool; secondly, these spectra were added using the *mathpha*, *addarf* and *addrmf* tools weighting for the exposure time of the individual observations; finally, channels (hence counts) of each spectrum were grouped using the *grppha* tool. The total exposure time for each source is reported in Table 3.1. It is lower than the total observing time of the field (namely 7Ms), as the effects of the vignetting, which depend on energy and off-axis angle, are accounted for. Indeed, the sources with the largest off-axis angle are the sources with the smallest exposure time.

For two out of six sources (XID412 and XID546), those with the largest number of counts, the χ^2 statistic was used requiring at least 20 counts per bin. For the other ones the Cash statistic (Cash 1979) was used, requiring at least 1 count per bin.

For each source a given number of net counts (i.e. background-subtracted) was collected from the spectral extraction in the full-band $0.5 - 7.0$ keV. The number of counts ranges between ~ 90 and ~ 2065, with a median value of about 300. Bearing in mind that this quantity increases roughly as the exposure time, the values obtained can be compared with those presented in the source main catalog by Xue et al. (2011) for the 4Ms dataset (Table 3.1). Multiplying the number of counts provided by Xue et al. by a factor ~ 1.75, given by the ratio between the exposure times of the 7 and 4Ms, we obtained a good agreement with our values for four out

of six sources. As reported in Table 3.1, the number of counts does not show a large increase for XID34 and XID403. However, these are the most off-axis sources, and the PSF at the edges of the field suffers from strong distortion effects. In particular, Xue et al. accounted for these effects, adopting poligonal source extraction regions. On the contrary, we used a "traditional" circular extraction region, which may have missed some of the photons produced by XID34 and XID403. However, the obtained fluxes are corrected for this different choice by the ARF. Finally, we highlight that some spectra were then fitted in a narrower energy range, in order to exclude spectral regions with a high background.

Source (a)	Counts (b)	Counts (c)	Off-axis angle (d)	Exposure time (e)
34	238^{+28}_{-26}	260 ± 16	9.43	1.8×10^6
262	215^{+19}_{-18}	335 ± 18	3.76	5.5×10^6
403	82^{+26}_{-25}	88 ± 9	7.89	4.3×10^6
412	435^{+25}_{-23}	714 ± 27	2.69	6.3×10^6
490	85^{+12}_{-11}	149 ± 12	1.89	5.6×10^6
546	1231^{+40}_{-39}	2065 ± 45	2.60	6.6×10^6

Table 3.1: Summary of source parameters. $^{(a)}$ XID; $^{(b)}$ net counts (i.e. background-subtracted) presented in Xue et al. (2011), which refer to the 4Ms dataset; $^{(c)}$ net counts collected for the whole sample in this work, referred to the 7Ms dataset (errors were computed assuming a Poisson statistic); $^{(d)}$ off-axis angle, i.e. the angular separation between the X-ray source and the CDF-S average aimpoint, from the 4Ms source catalog; $^{(e)}$ total exposure time in seconds.

3.2 Spectral models

The X-ray spectra of AGN are characterized by several components associated with different physical processes, and modelling them properly is fundamental in order to derive source physical parameters. In obscured AGN spectra especially we find contributions related to absorption, scattering and reflection of the direct X-ray emission which contribute differently for different lines of sight. Through X-ray spectral analysis it is possible to constrain important quantities, such as the amount

of obscuration, the equivalent width (EW) of the iron emission line, the intrinsic luminosity. The analysis was performed by means of the X-ray spectral fitting package XSPEC v. 12.8.2 (Arnaud 1996).

Due to the low photon statistics characterizing our X-ray spectra - the best possible for this kind of sources so far - we started the spectral analysis with the simplest model, i.e. a power law including Galactic absorption[1] (XSPEC models POWERLAW and PHABS), in order to verify whether it is possible to reproduce the observed emission. As shown in Fig. 3.2 (*top panel*), where an example of spectrum for the source XID490 is reported, the model does not provide a good fit as it cannot reproduce the whole spectrum. Although the intrinsic photon index tipically found for AGN is $\Gamma = 1.8 \pm 0.2$ (e.g. Nandra & Pounds 1994, Mainieri et al. 2002, Mateos et al. 2005, Tozzi et al. 2006), sources with low counting statistics usually have flatter spectral indices with large errors (e.g. Del Moro et al. 2015). Indeed, we measured $\Gamma = 0.2^{+0.3}_{-0.4}$, as expected for type-2 AGN, whose spectra are harder and more obscured than those observed for sources with higher number of counts. Moreover, this spectrum presents a strong emission line. Such flat slopes, especially if coupled with prominent emission features, are characteristic of heavy obscuration, as explained in § 1. As it is not possible to obtain reasonable constraints on Γ, we fixed it to 1.8, but large residuals were obtained in any case (Fig. 3.2, *bottom panel*), requiring the presence of an obscuring spectral component.

Hence, to obtain a better reproduction of the spectra, more complex models were adopted. Considering the limited counting statistics, the spectral fits were performed with the purpose of minimizing the number of free parameters to constrain reasonably the resulting best-fit parameters. Four main models, described below, have been used: the transmission and the reflection ones are phenomenological models, built up by combining single components in order to reproduce the observed spectra; the MYTorus and the BNTorus ones, instead, treat the line and the continuum components self-consistently. The adopted models have fixed geometry, as it is not exactly known a priori for these specific sources and data quality does not allow us to obtain them from the fitting process itself. Furthermore, for most of the sources, the poor photon statistics have not allowed us to simultaneously place tight constraints on the photon index and the column density, as they are degenerate for low count spectra. Therefore, to obtain a better determination on the column density, fixing the photon index has been necessary.

[1] A model component accounting for absorption within our Galaxy was included in all spectral models, the column density at each given position was calculated using the Ftool *nh*.

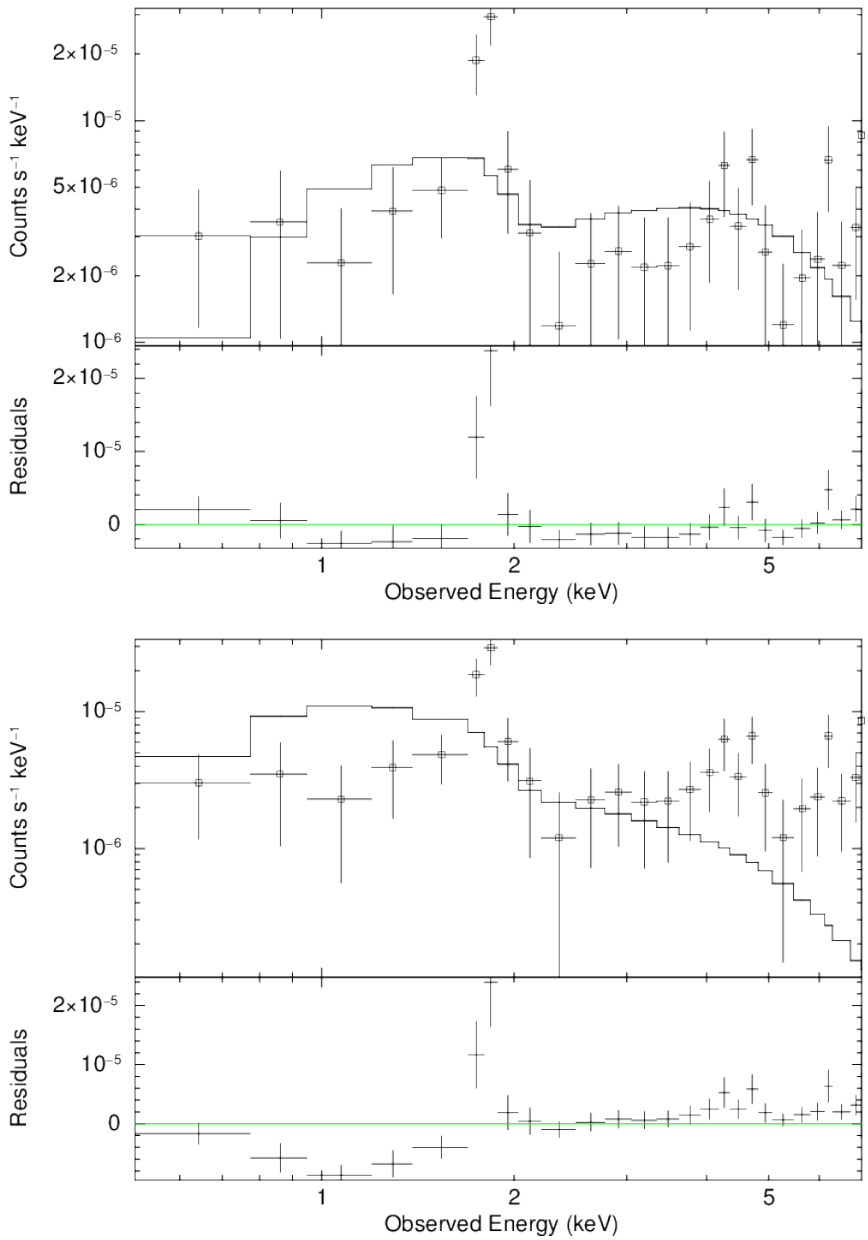

Figure 3.2: X-ray spectrum of XID490. *Top panel*: The spectrum is fitted by a spectral model made up of a power law including Galactic absorption with the photon index left free to vary. The best-fit photon index, $\Gamma = 0.2^{+0.3}_{-0.4}$, is typical of heavily obscured spectra, along with the presence of a prominent emission feature. *Bottom panel*: The spectrum is fitted by the same model used above, but with the photon index fixed to 1.8, as expected for the intrinsic AGN emission. However, the large residuals point out the necessity of an obscuring spectral component as well as an emission component. The spectrum has been rebinned for presentation purposes. The residuals, i.e. the difference between the data and the model, are shown at the bottom of both panels and the Cash statistic has been adopted.

3.2.1 Transmission model

A first simple model accounting for the transmitted emission has been considered as a start. As discussed in § 1, for obscured sources only a fraction of the primary emission escapes absorption from the obscuring medium. Therefore, this model reproduces the observed spectrum assuming that it consists of the surviving scattering component, only accounting for photoelectric absorption and neglecting Compton scattering. It was built up with four model components, shown in Fig. 3.3:

- a primary power law (XSPEC model POWERLAW) with the photon index fixed to 1.8;
- photoelectric absorption intrinsic to the source which accounts for the obscuration that characterizes AGN spectra (XSPEC model ZPHABS);
- a Gaussian line representing the observed Fe Kα fluorescence emission line, whose line width σ was fixed to 10 eV assuming that it is produced by a cold reflector (XSPEC model ZGAUSS);
- an unabsorbed power law (referred to as scattered or secondary power law), when the data demand it, with the photon index tied to the primary one which accounts for the observed soft emission. It can be due to different processes, e.g. emission related to Thomson scattering outside the reprocessing material, thermal emission deriving from star formation or the blend of emission lines from photo-ionized circumnuclear gas. Distinguishing among these different mechanisms is not possible since the spectra are characterized by a poor photon statistics and an insufficient spectral resolution. Thus, the secondary power law is used as a general description.

Five parameters were left free to vary: the column density, the Gaussian line energy and the normalizations of the different model components.

3.2.2 Reflection model

When we consider heavy Compton-thick sources, with $N_{\rm H} \gtrsim 10^{25}$ cm^{-2}, the direct nuclear emission is entirely absorbed by the reprocessing material and only the reflected emission is observed. Since we are dealing with very large obscuring column densities, a pure reflection model has been considered as well. It is parametrized by the XSPEC model PEXRAV, contributing with just the reflected component, hence

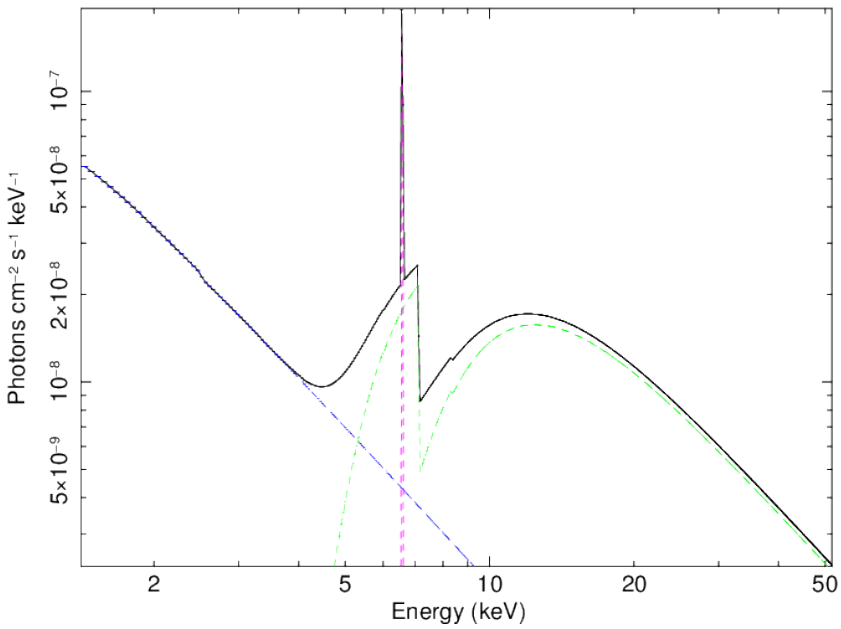

Figure 3.3: An example of transmission model used in the fit of the source XID412. The spectrum is composed of three components: a primary power law modified by intrinsic absorption (green line), a Gaussian line (magenta line) and a secondary power law (blue line). The sum of all components is represented by the black solid line.

not accounting for transmission through the absorbing material. Actually, this model was introduced to reproduce reflected emission by a plane-parallel, semi-infinite medium of cold electrons (e.g. an accretion disc) and not by an obscuring torus, but it can be used as an approximation. A power law with $\Gamma = 1.8$ was assumed as incident spectrum and a Gaussian line was added in order to reproduce the iron emission line (Fig. 3.4). In this model the line energy was left free to vary along with the model component normalizations, for a total of three free parameters. A viewing angle equal to 60° was considered, since for this value the reflected spectrum is the closest, in overall shape, to the reflected spectrum averaged over all viewing angles (Magdziarz & Zdziarski 1995). Moreover, the cut-off energy was fixed to 100 keV.

3.2.3 MYTorus

MYTorus (Murphy & Yaqoob 2009) is a self-consistent model suitable especially for spectral fitting of Compton-thick sources, but it is valid for column densities in the range $10^{22} - 10^{25}$ cm^{-2}. This model adopts a toroidal geometry for the reprocessor (a

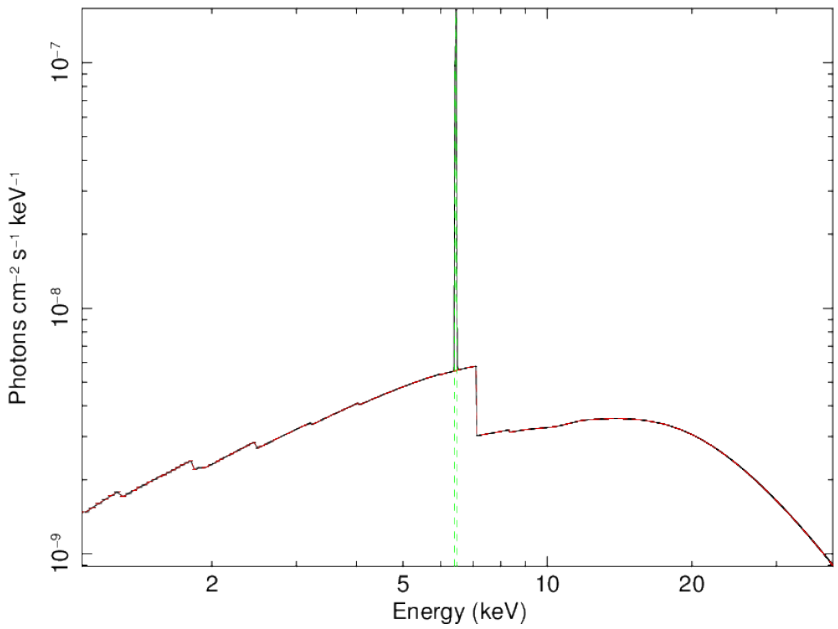

Figure 3.4: An example of reflection model used in the fit of the source XID490. It comprises two components: a reflection continuum (red line) and a Gaussian line (green line). The total emission is shown in black.

tube-like, azimuthally-symmetric torus) with a half opening angle of 60°, assuming that the reprocessing material is uniform, neutral and cold. The model geometry is shown in Fig. 3.5. The X-ray continuum source is located at the center of the torus and emits isotropically. The line of sight column density is:

$$N_{\mathrm{H,\,l.o.s.}} = N_{\mathrm{H}} \left[1 - \left(\frac{c}{a} \right)^2 \cos^2 \theta_{\mathrm{obs}} \right]^{\frac{1}{2}} \tag{3.1}$$

where N_{H}, the equatorial column density, is defined as the equivalent Hydrogen column density through the diameter of the tube of the torus, θ_{obs} is the inclination angle of the observer's line of sight with respect to the simmetry axis of the torus, a is the radius of the tube and c is the distance from the center of the torus to the center of the tube (Fig. 3.5).

MYTorus is implemented through interpolation of pre-calculated spectra in the form of tables. There are three groups of model components that combine to produce the total spectrum:

– The unscattered continuum, known also as "transmitted" continuum, is composed of the incident photons that do not interact with the torus and escape it. For the primary spectrum a power-law continuum is considered, with a photon

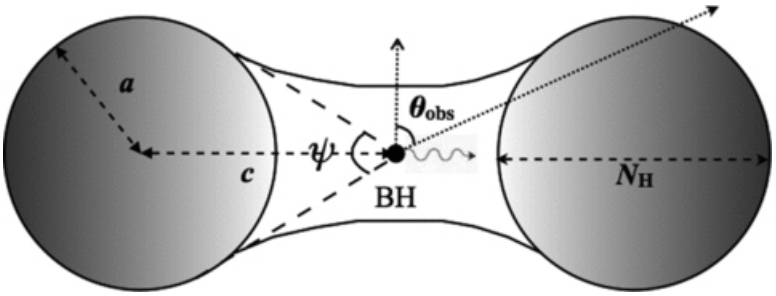

Figure 3.5: MYTorus model geometry. The X-ray source is located at the center of the torus, θ_{obs} is the observer's line of sight with respect to the symmetry axis of the torus. $N_{\rm H}$ is the equatorial column density of the torus, defined by the diameter of the tube. "BH" is the illuminating X-ray source and is located at the origin of the torus. The half-opening angle is equal to $(\pi - \psi)/2$ and $c/a = 2$ (from Murphy & Yaqoob 2009).

index fixed to 1.8; this spectrum terminates at a specific energy $E_{\rm T} = 500$ keV in the model adopted in this work. However, considering the spectral energy range of our sources, a lower cut-off value would not infuence the results.

– The scattered continuum, referred to as "reflection spectrum", takes into account the escaping photons scattered in the reprocessing medium at least once.

– The emission line component accounts for the zeroth-order and scattered photons producing the Fe Kα and Kβ fluorescence emission lines, in order to represent the "core" and the "Compton shoulder" respectively of these observed lines.

An additional unobscured power law was included in the model to account for the observed soft emission. Fig. 3.6 shows an example of this kind of model. The free model parameters are three: the column density, the secondary power-law normalization and the unscattered continuum normalization.

3.2.4 BNTorus

Similarly to the MYTorus model, the Brightman and Nandra torus (Brightman & Nandra 2011) is a self-consistent model. It has been constructed for column densities in the range $10^{21} - 10^{26}$ cm^{-2} and reproduces photoelectric absorption, Compton scattering and fluorescence lines. It assumes an X-ray point source emitting a power-law spectrum positioned at the center of a toroidal distribution of gas. The medium is characterized by a biconical distribution of matter with constant density and, as

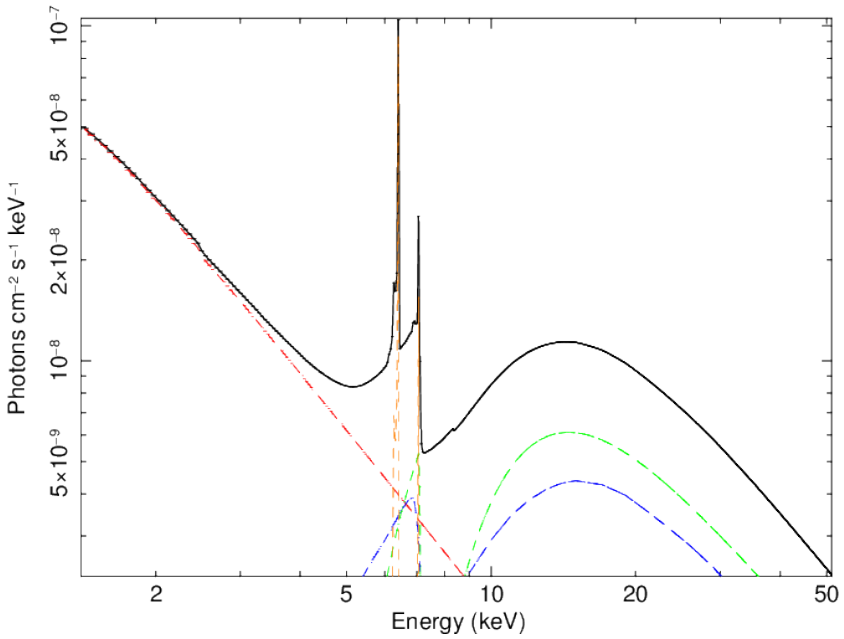

Figure 3.6: An example of MYTorus model used in the fit of the source XID262. The components shown in the spectrum are: the unscattered continuum (green line), the scattered continuum (blue line, i.e. the reflection component in MYTorus), the emission line components (orange line) and the soft component (red line). The black line represents the total emission.

a result, the line of sight column density does not depend on the inclination angle of the observer (Fig. 3.7). This model includes several emission lines in addition to the Fe Kα and Kβ, such as Kα emission lines from Nickel, Chromium, Calcium and other elements. These lines are modelled properly considering Compton scattering of fluorescent photons, hence including the Compton shoulder. In Fig. 3.8 an example of this model is presented.

BNTorus is implemented through table models, but the several model components are included in the same table, while they are treated in different tables in the previous model. The photon index of the primary power law was fixed to 1.8, the opening angle to 60° and a secondary power law was included in order to reproduce the observed soft emission.

The number of free parameters is three: the column density, the table model normalization and the secondary (i.e. scattered) power-law normalization.

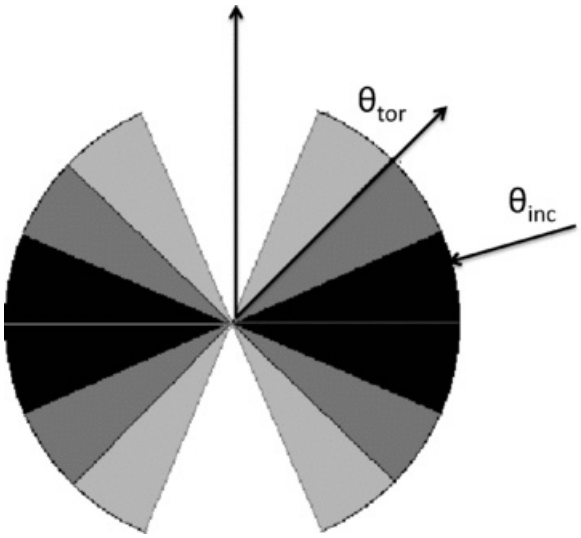

Figure 3.7: BNtorus geometry. A biconical distribution of matter is assumed so as to have a constant column density that does not depend on the inclination angle of the observer, $\theta_{\rm inc}$. $\theta_{\rm tor}$ defines the opening angle. The shading only serves to differentiate the possible opening angles and does not correspond to different densities (from Brightman & Nandra 2011).

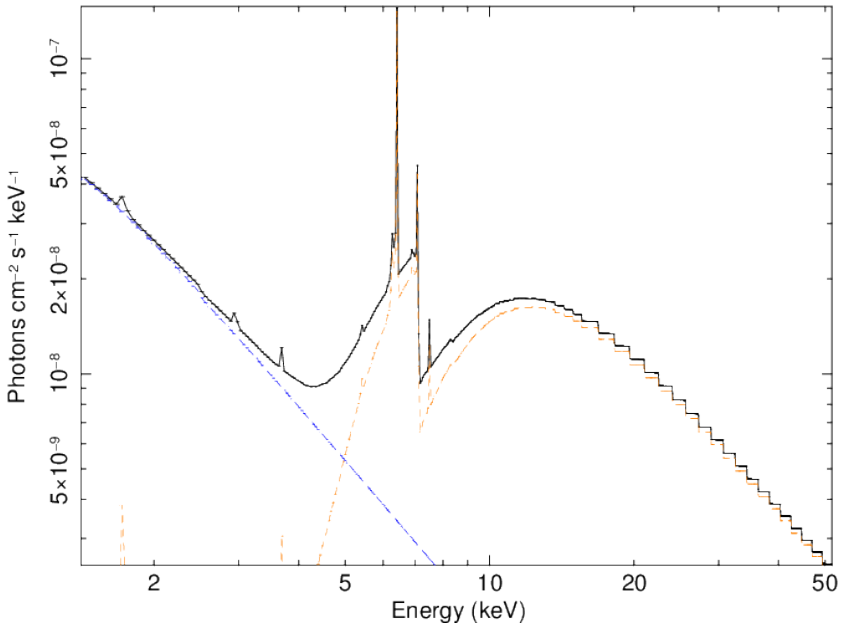

Figure 3.8: An example of BNTorus referred to the source XID412. The orange line represents the whole table model component, the soft component is shown in blue whereas the black line reproduces the total emission.

3.3 Results

Due to the redshift range of our sources $z = 2.58 - 4.76$, the scattered/reflected emission which dominates the high energy spectra of heavily obscured AGN (usually above ~ 10 keV rest-frame) is shifted in the ACIS-I energetic range ($0.5 - 7.0$ keV). The whole sample presents heavily obscured spectra, characterized by column densities in the range $\sim 3 \times 10^{23} - 4 \times 10^{24}$ cm^{-2}. An iron emission line was detected for 5 out of 6 sources and, in terms of EW, it is consistent with the strong iron line (EW $\sim$ 1 keV) typically observed in very obscured sources, considering the errors. Because of the limited photon statistics, some physical quantities are not well constrained and loose limits were placed. Moreover, more complex models were not used to fit the spectra with the poorest quality (namely, the spectra of the sources XID34 and XID403), as the code could not be able to find a good fit and best-fit parameters could hardly be constrained.

Hard X-ray luminosities, computed in the range $2 - 10$ keV, were corrected for the effect produced by absorption and are in the range $(2 - 6) \times 10^{44}$ erg s^{-1}, typical of quasars (see § 1.3). Instead, observed fluxes calculated in the $2 - 10$ keV band range between $(1 - 7) \times 10^{-15}$ erg cm^{-2} s^{-1}.

Rest-frame EWs were calculated in different ways depending on the model used:

- for the transmission and the reflection models, EW can be computed independently since it is an output of the model;
- for the MYTorus model, it was obtained calculating the iron Kα line flux of the emission-line table component, and dividing it by the monochromatic continuum flux at the line centroid;
- for the BNTorus model computing the EW is not possible as it is not an output of the model and, in addition, all the components are implemented in the same table. Therefore the emission line component cannot be separated to calculate line fluxes.

As far as the reflection model is concerned, it must be noticed that the model luminosity in the range $2 - 10$ keV is even one order of magnitude lower than the intrinsic luminosities calculated from other models (see Table 3.2). The reflection model accounts for the reflected emission only; therefore, determining the intrinsic luminosity by taking into account the effect produced by absorption, would require assumptions on the geometry of the system and on the distribution of the absorber.

Fit results are presented below for each source specifically, and the best-fit parameters derived from the spectral analysis are reported in Table 3.2. Errors are given at the 90% confidence level for one parameter of interest (Avni 1976). The intrinsic luminosity, instead, is determined by correcting for obscuration, hence the uncertainties on the column density, as well as on the flux, have to be accounted for. We determined the errors for the luminosity by considering the 90% confidence level for two parameters of interest, namely the column density and the power-law normalization.

XID34

XID34 is the source of the sample with the largest off-axis angle, so it is strongly background-dominated and the useful energy range is reduced to $0.5 - 3$ keV. The spectrum was fitted with both the transmission and the reflection model and a secondary power law was not needed by the data. Fig. 4.5 shows the fit performed with the transmission model. The column density is $\sim 2 \times 10^{23}$ cm^{-2} and the Fe Kα line has been detected at a rest-frame energy of about 6.5 keV at $\sim 1.3\sigma$, although the EW is smaller than 1 keV as usually observed for heavily obscured sources. The EW value is characterized by large errors due to the poor spectral quality.

A significant difference in the observed fluxes between 2 and 10 keV resulted from the two spectral fits (see Table 3.2), even though the C-stat/dof values are similar for both models. However, outside the covered energy range, the model trend is extrapolated in order to compute the flux, so this difference can be due to different trends of the models.

Moreover, this source was detected in the 1Ms dataset by Tozzi et al. (2006), who found a similar value for the column density and the luminosity ($N_{\rm H} \sim 3 \times 10^{23}$ cm^{-2} and $L_{[2-10\,\rm keV]} = 1.16 \times 10^{44}$ erg s^{-1}), but a very different value for the flux ($F_{[2-10\,\rm keV]} = 1.90 \times 10^{-15}$ erg cm^{-2} s^{-1}). The iron line was not detected neither in the 1Ms spectrum nor in the 4Ms one during a preliminary analysis that we performed on the 4Ms dataset at the beginning of this study.

XID262

XID262 was analyzed using the whole group of models described above. As far as the transmission and the reflection models are concerned, they both provide good fits although the iron line, consistent with emission from neutral material at a rest-frame energy of 6.3 keV, is better constrained in the former. Indeed, for the reflection

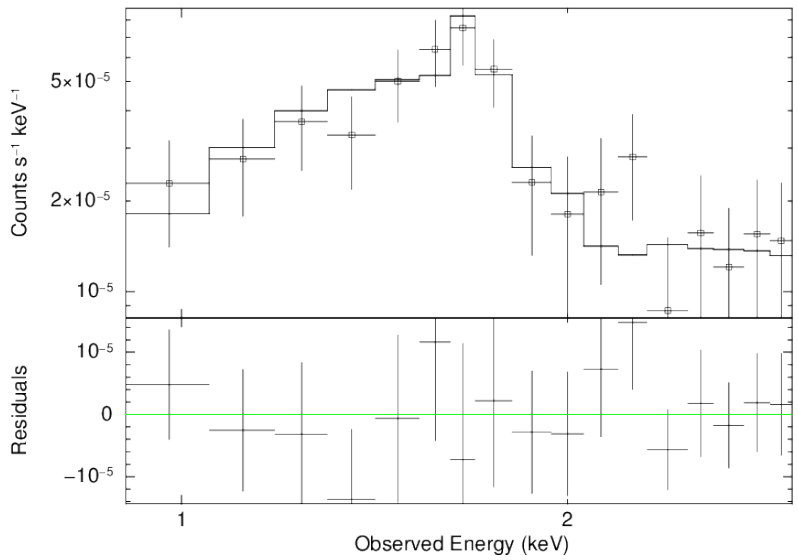

Figure 3.9: 7Ms *Chandra* X-ray spectrum of the source XID34 fitted by the transmission model; a secondary power law reproducing the soft emission was not needed by the data. An iron emission line was detected at ~ 6.5 keV rest-frame at $\sim 1.3\sigma$. The residuals, i.e. the difference between the data and the model, are shown at the bottom of the figure and the Cash statistic has been adopted. Because of the poor photon statistics, as well as the large off-axis angle, the spectrum resulted to be background-dominated. Therefore, we performed the analysis in a narrower energy range. The spectrum has been rebinned for presentation purposes.

model, determining errors for the line energy was not possible and only an upper limit for the EW was computed. For the transmission and the MYTorus models, the EW is consistent with the typical value of ~ 1 keV, although the errors are quite large (Table 3.2). The BNTorus and the MYTorus models provide very similar results, with the Fe emission line detected at $\sim 2.6\sigma$. Moreover, a soft component was added to the transmission model and the resulting fraction of scattered emission, computed as the ratio between the power-law normalizations, is of $\sim 6\%$. The spectrum of the source, fitted by the BNTorus model, is shown in Fig. 4.6.

Column densities obtained from the different models, of $\sim 1.5 \times 10^{24}$ cm^{-2}, are in agreement and point to a Compton-thick emission. Vito et al. (2013) and Mainieri et al. (2005), studying the 4Ms and the 1Ms datasets respectively, found lower values for the column density, flux and luminosity but in reasonable agreement with our measurements within the errors. The iron line, detected in this dataset, was not identified in the previous analyses.

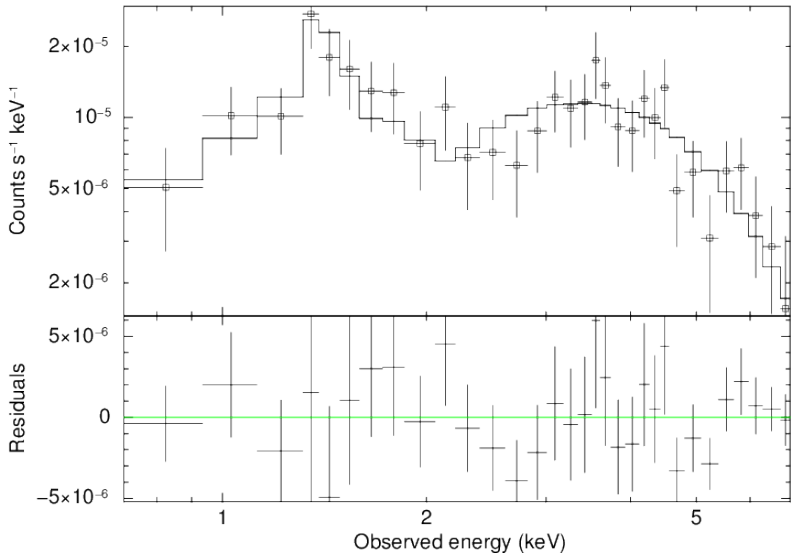

Figure 3.10: 7Ms *Chandra* X-ray spectrum of the source XID262 fitted by the BNTorus model. It is characterized by a reasonable count statistics as well as an intense iron emission line at ~ 6.4 keV rest-frame detected at $\sim 2.6\sigma$. The residuals, i.e. the difference between the data and the model, are shown at the bottom of the figure and the Cash statistic has been adopted. The spectrum has been rebinned for presentation purposes.

XID403

XID403 is a very off-axis source and is characterized by a very low photon statistics (see Table 3.1), hence it was analyzed using the simplest models, namely the transmission and the reflection ones. In order to investigate the presence of an iron emission line, as already observed by Gilli et al. (2014), and because of the poor photon statistics, the spectrum was grouped providing the *grppha* tool with the grouping information through a data file containing channels selected manually.

Both the transmission and the reflection models produce a reasonable fit but, while for the former an emission line is clearly detected with the centroid energy left free to vary, the same line in the latter is poorly constrained, so computing errors for the line was not possible and just an upper limit for the EW has been obtained. Due to the poor quality of this X-ray spectrum, rather loose constraints can be placed to best-fit parameters. Moreover, a secondary power law was not required. Fig. 4.7 shows the spectrum of the source fitted by the transmission model.

The spectral analysis provided a value for the column density of $\sim 1.5\times10^{24}$ cm^{-2}. The emission line, at a rest-frame energy of ~ 6.9 keV and detected at $\sim 1.3\sigma$, can be interpreted as emission from highly ionized iron (i.e. hydrogen-like iron, see the

discussion about the iron line in § 1.2.1). The measured EW is very large and, along with the obtained column density, points to Compton-thick absorption associated with this spectrum. These results are in agreement with those found by Gilli et al. (2014), i.e. $N_{\rm H} = 1.4^{+0.9}_{-0.5} \times 10^{24}$ cm^{-2} and $EW = 2.8^{+1.7}_{-1.4}$ keV. Considering the high column density, both the transmitted and the reflected scenarios are possible although the C-stat/dof value is slightly lower for the latter.

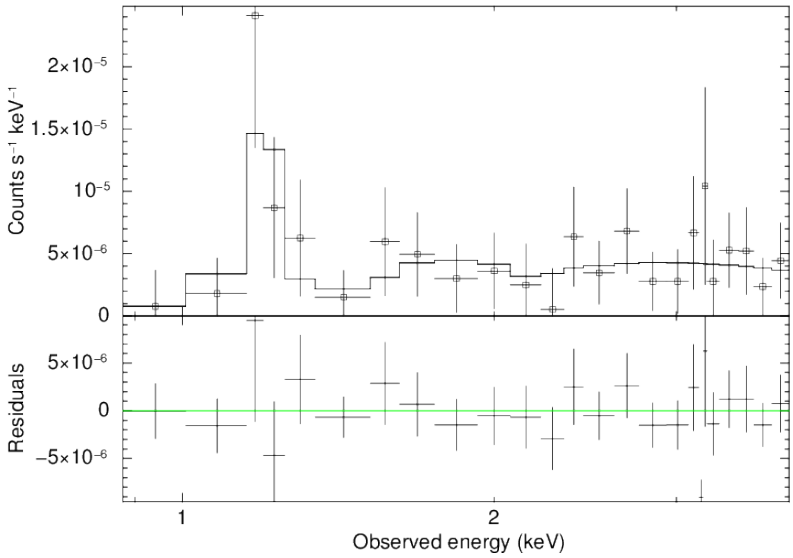

Figure 3.11: 7Ms *Chandra* X-ray spectrum of the source XID403 fitted by the transmission model; a secondary power law to reproduce the soft emission was not needed by the data. A Fe emission line was detected at $\sim 1.3\sigma$, and at a rest-frame energy of ~ 6.9 keV. The residuals, i.e. the difference between the data and the model, are shown at the bottom of the figure and the Cash statistic has been adopted. The spectrum has been rebinned for presentation purposes.

XID412

XID412 is a well studied heavily obscured AGN which lies in the inner region of the CDF-S area. The photon statistics is reasonably good, thus it was analyzed using all models described above. Best-fit parameters obtained using the different models, reported in Table 3.2, are in good agreement within the errors. Fig. 4.8 shows the spectrum of the source fitted by the transmission model. The soft component accounts for about 6% of the unobscured flux at 1 keV.

A comparison between the transmission and the reflection models points out that the former gives a better fit quality according to the C-stat/dof values. The MYTorus and the BNTorus models, treating both components self-consistently, confirm

the fact that the source is best described by a transmission-dominated continuum. The emission line, detected at $\sim 2\sigma$ and at ~ 6.6 keV rest-frame, could be ascribed to emission from either neutral or ionized iron (i.e. helium-like iron, see § 1.2.1). The EW, accounting for the errors, is consistent with the line commonly observed in obscured AGN spectra. Best-fit parameters provide a good agreement with those presented by Comastri et al. (2011) in a previous study of this source using XMM-*Newton* data, although flux and luminosity result higher than ours by a factor ~ 1.4 and ~ 1.7, respectively. Our values are more similar to those found by Vito et al. (2013) using the 4Ms dataset.

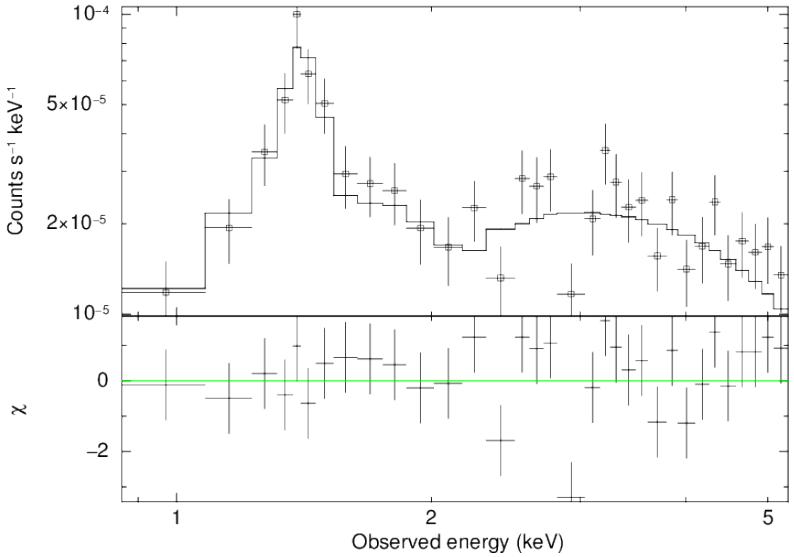

Figure 3.12: 7Ms *Chandra* X-ray spectrum of the source XID412 fitted by the transmission model. An iron emission line was detected at ~ 6.6 keV rest-frame at $\sim 2\sigma$. The spectrum is characterized by a reasonably good count statistics, thus we adopted the χ^2 statistic. The residuals in terms of σ are shown at the bottom of the figure.

XID490

XID490 is characterized by a poor photon statistics but its heavy Compton-thick nature, initially pointed out by the fit with the transmission model, led us to use also more complex ones. Actually, the transmission model is not able to reproduce properly heavily obscured spectra, since it takes into account photoelectric absorption only, not including Compton scattering. This last process becomes not negligible at high column densities. Indeed, best-fit parameters obtained from the simple transmission model were not in perfect agreement with those from the other

models, especially the luminosity. Hence, we performed a spectral fit using the XSPEC model PLCABS (Yaqoob 1997), which calculates transmitted emission for a cold, spherical and uniform distribution of matter surrounding an X-ray source. It considers Compton scattering, though the reflection continuum and the fluorescent line are not accounted for, thus a Gaussian line component was added as well. Moreover, it works for column densities up to $\sim 5 \times 10^{24}$ cm^{-2} and for a maximum observed energy of $\sim 10 - 18$ keV. A soft component was added to the transmission model and the resulting fraction of scattered emission, computed as the ratio between the power-law normalizations, is of $\sim 6\%$. The spectrum of the source, fitted by the MYTorus model, is shown in Fig. 4.9.

This source presents a flat spectrum and an extremely strong iron Kα line at ~ 6.4 keV rest-frame, clearly detected at $\sim 3\sigma$. EW values are very large but with limited constraints, while for the MYTorus model just a lower limit was determined. The column density is about 3×10^{24} cm^{-2} from the transmission model, while values obtained from the MYTorus and BNTorus models are unconstrained at the upper end (see Table 3.2). All models provide a good fit and agree in terms of flux and luminosities. XID490 was studied using the 1Ms dataset by Tozzi et al. (2006). They obtained a poorly constrained column density of about 1.9×10^{23} cm^{-2} and no lines were detected.

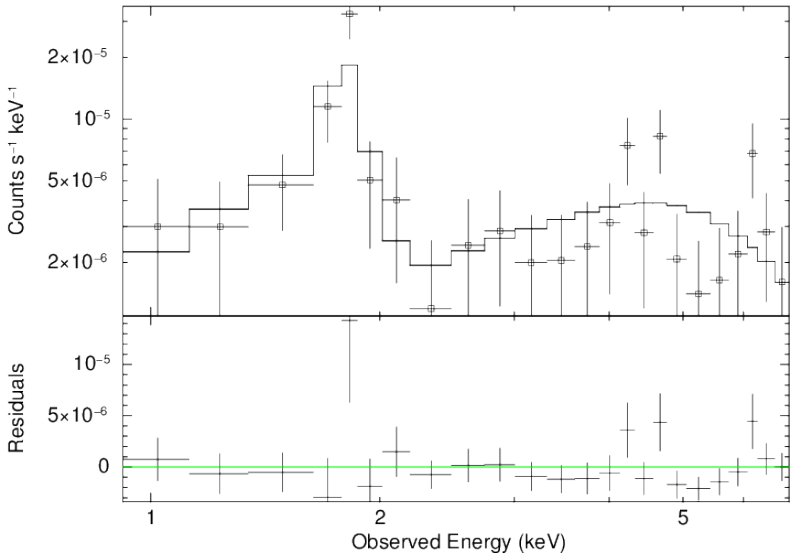

Figure 3.13: 7Ms *Chandra* X-ray spectrum of the source XID490 fitted by the MYTorus model. A Fe emission line was clearly detected at $\sim 3\sigma$, and at a rest-frame energy of ~ 6.4 keV. The residuals, i.e. the difference between the data and the model, are shown at the bottom of the figure and the Cash statistic has been adopted. The spectrum has been rebinned for presentation purposes.

XID546

XID546 is the brightest source of the sample and among the innermost sources in the CDF-S. The transmission model provided a good fit, while the reflection model was characterized by a large C-stat/dof value, thus it will not be considered. Therefore, this X-ray spectrum could be explained as transmitted emission, as proven by the best-fit column density equal to $\sim 4.4 \times 10^{23}$ cm^{-2}. Thanks to the good counting statistics, we were able to place constraints on both the column density and the photon index simultaneously, leaving the photon index as a free parameter in the transmission model. An equally good fit has been obtained with the MYTorus model (Table 3.2). Fig. 4.10 shows the spectrum of the source fitted by the MYTorus model.

XID546 is also the only source without a detected emission line. By means of the transmission model, an upper limit for the EW of the 6.4 keV iron emission line was computed, while for the MYTorus model the emission line table was removed from the overall model. The spectrum was not fitted with the BNTorus model, as all the components are implemented in the same table and therefore it is not possible to exclude the emission line component. Moreover, the best-fit parameters provide a good agreement with those obtained by Vito et al. (2013).

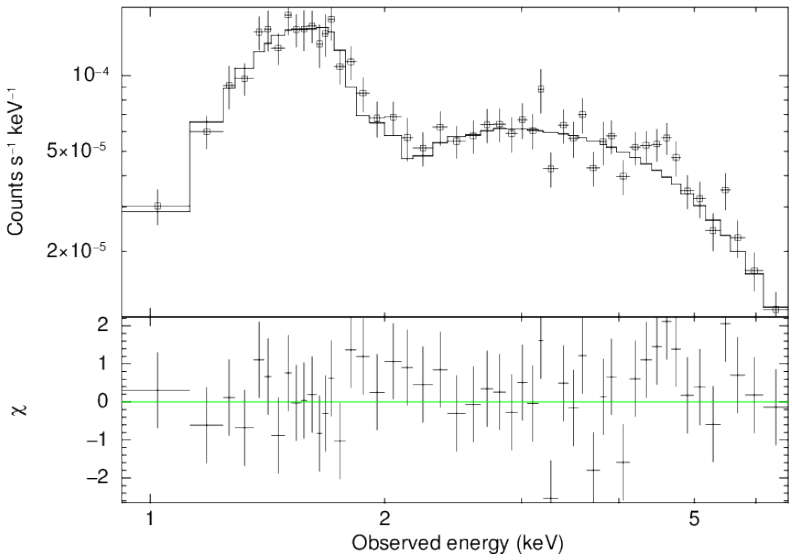

Figure 3.14: 7Ms *Chandra* X-ray spectrum of the source XID546 fitted by the MYTorus model. The emission line component was removed from the the overall model, as it provided larger residuals. The spectrum is characterized by a good count statistics, thus we adopted the χ^2 statistic. The residuals in terms of σ are shown at the bottom of the figure.

3.3.1 Summary of the results from X-ray spectral analysis

The X-ray spectral analysis performed for our sources pointed out the presence of heavy obscuration and high intrinsic luminosities in all of them. Fig. 5.1 shows the column densities obtained for our sample plotted against redshift. The comparison with previous analyses of these AGN stresses the importance of deep data for this kind of studies and, in particular, the role of the 7Ms *Chandra* observations, which are the best data available so far to analyze distant and obscured quasars. In addition to the improved statistics and spectral quality, these data allowed us to detect the iron line in three sources where this emission feature was not detected in previous studies.

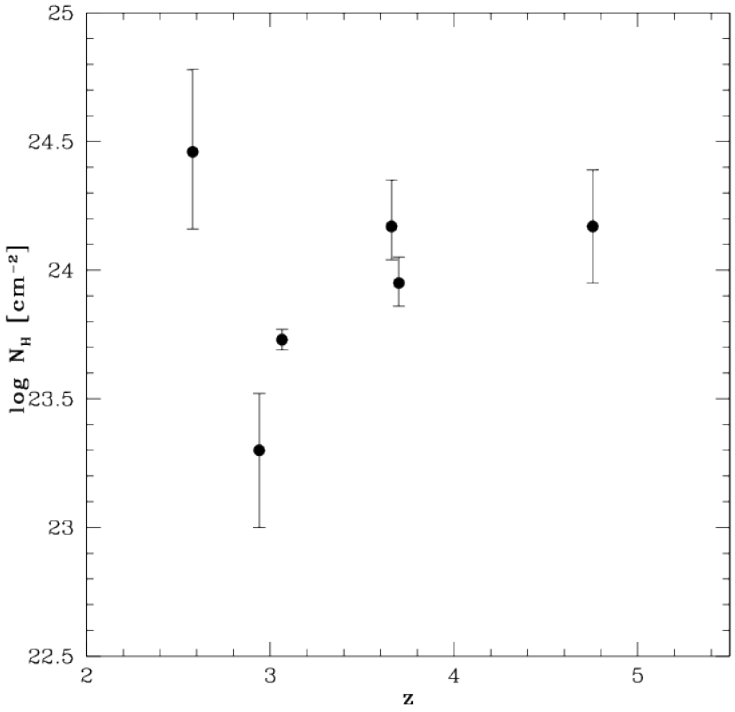

Figure 3.15: Column densities (derived from X-ray spectral analysis) vs. redshift for our six sources.

Source	Model	Stat/dof	$N_{\rm H}$	Γ	$E_{\rm Fe\ line}$	EW	$F_{[2-10\,{\rm keV}]}$	$L_{[2-10\,{\rm keV}]}$
(a)	(b)	(c)	(d)	(e)	(f)	(g)	(h)	(i)
34	Transmission	98.2/125	$20.3^{+12.5}_{-10.4}$	1.8	$6.57^{+0.20}_{-0.37}$	370^{+339}_{-293}	$3.03^{+0.42}_{-0.44}\times10^{-15}$	$1.96^{+1.04}_{-0.67}\times10^{44}$
	Reflection	98.6/126	-	1.8	$6.54^{+0.24}_{-0.38}$	307^{+311}_{-264}	$8.08^{+0.76}_{-0.78}\times10^{-15}$	$8.11^{+0.73}_{-0.71}\times10^{43}$
262	Transmission	205.1/247	$148.5^{+55.7}_{-35.7}$	1.8	$6.30^{+0.24}_{-0.24}$	628^{+572}_{-487}	$1.92^{+0.20}_{-0.20}\times10^{-15}$	$2.43^{+0.60}_{-0.46}\times10^{44}$
	Reflection	211.9/249	-	1.8	6.34	<493	$1.63^{+0.15}_{-0.15}\times10^{-15}$	$2.40^{+0.24}_{-0.21}\times10^{43}$
	MYTorus	204.2/249	$148.0^{+77.4}_{-36.9}$	1.8	6.4	517^{+1561}_{-196}	$2.00^{+0.22}_{-0.24}\times10^{-15}$	$3.97^{+2.92}_{-1.17}\times10^{44}$
	BNTorus	204.3/249	$145.3^{+81.7}_{-37.6}$	1.8	6.4	-	$1.96^{+0.20}_{-0.24}\times10^{-15}$	$3.91^{+3.62}_{-1.12}\times10^{44}$
403	Transmission	29.4/45	$148.1^{+96.3}_{-58.0}$	1.8	$6.92^{+0.50}_{-0.26}$	2491^{-2399}_{+1904}	$1.45^{+0.30}_{-0.30}\times10^{-15}$	$2.97^{+2.16}_{-1.37}\times10^{44}$
	Reflection	32.4/46	-	1.8	6.9	<1214	$1.03^{+0.13}_{-0.14}\times10^{-15}$	$2.91^{+0.54}_{-0.46}\times10^{43}$
412	Transmission	40.4/31	$98.8^{+24.6}_{-19.5}$	$1.67^{+0.12}_{-0.12}$	$6.57^{+0.20}_{-0.17}$	510^{+305}_{-304}	$2.36^{+0.23}_{-0.23}\times10^{-15}$	$2.85^{+0.42}_{-0.39}\times10^{44}$
	Reflection	48.4/32	-	1.8	$6.59^{+0.18}_{-0.13}$	680^{+326}_{-325}	$2.46^{+0.28}_{-0.27}\times10^{-15}$	$3.32^{+0.35}_{-0.36}\times10^{43}$
	MYTorus	43.0/33	$89.7^{+21.2}_{-17.3}$	1.8	6.4	319^{+954}_{-67}	$2.41^{+0.23}_{-0.26}\times10^{-15}$	$3.67^{+0.87}_{-0.68}\times10^{44}$
	BNTorus	42.6/33	$88.4^{+18.7}_{-17.4}$	1.8	6.4	-	$2.39^{+0.21}_{-0.26}\times10^{-15}$	$3.76^{+0.79}_{-0.67}\times10^{44}$
490	Transmission	128.5/152	$289.7^{+307.1}_{-143.8}$	1.8	$6.44^{+0.09}_{-0.09}$	5124^{+2107}_{-1732}	$0.93^{+0.10}_{-0.20}\times10^{-15}$	$2.72^{+0.60}_{-0.76}\times10^{44}$
	Reflection	135.0/154	-	1.8	$6.45^{+0.10}_{-0.11}$	1599^{+823}_{-687}	$0.63^{+0.07}_{-0.06}\times10^{-15}$	$6.22^{+0.74}_{-0.80}\times10^{42}$
	MYTorus	130.6/154	>334.8	1.8	6.4	>1390	$1.06^{+1.88}_{-0.08}\times10^{-15}$	$>3.17\times10^{44}$
	BNTorus	130.5/154	>377.2	1.8	6.4	-	$1.03^{+0.27}_{-0.08}\times10^{-15}$	$>3.32\times10^{44}$
546	Transmission	83.6/87	$44.3^{+8.1}_{-7.3}$	$1.57^{+0.19}_{-0.18}$	6.4	<149	$7.21^{+0.42}_{-0.65}\times10^{-15}$	$3.83^{+1.65}_{-1.06}\times10^{44}$
	MYTorus	86.0/87	$54.3^{+6.2}_{-5.1}$	1.8	-	-	$6.85^{+0.37}_{-0.35}\times10^{-15}$	$6.07^{+0.60}_{-0.55}\times10^{44}$

Table 3.2: Best-fit parameters for the whole sample. Errors are given at the 90% confidence level. $^{(a)}$ XID; $^{(b)}$ model used to fit the source spectrum; $^{(c)}$ ratio between the statistic value and the number of degrees of freedom, we adopted the χ^2 statistic for the sources XID412 and XID546, and the Cash statistic for the other sources; $^{(d)}$ column density, in units of 10^{22} cm^{-2}; $^{(e)}$ spectral index; $^{(f)}$ rest-frame energy of the iron emission line in keV; $^{(g)}$ rest-frame equivalent width of the iron line in eV; $^{(h)}$ observed flux in the hard [2-10 keV] band, in units of erg cm^{-2} s^{-1}; $^{(i)}$ rest-frame absorption corrected luminosity in the hard [2-10 keV] band, in units of erg s^{-1}.

Chapter 4

SED fitting

AGN emission spans a wide range of wavelengths; each spectral band is marked with the imprints left by several physical mechanisms, and therefore a multi-wavelength approach is mandatory in order to extract information about the underlying emission processes in the observed AGN spectral energy distributions (SEDs). These processes are related to both the host galaxy and the active nucleus, thus a tool taking into account different emission components is necessary to disentangle them and hence estimate the galaxy and AGN physical parameters. SED decomposition techniques, that fit AGN emission from UV to FIR, combine properly models and templates which describe the emission produced by components such as stars, dust and AGN. Through this kind of analysis we are able to gather information about the fundamental properties of both the galaxy and the AGN, such as stellar masses, SFR, gas and dust content, and the accretion luminosity. Over the years various SED fitting procedures have been developed, but most of them are suitable for star-forming galaxies and do not have an AGN component included. Nevertheless, studying active galaxies means that the AGN contribution to the whole emission cannot be neglected and, only recently, tools which take into account this component have been developed.

This chapter is dedicated to the description of the emission components that play a key role in the UV to IR SEDs of AGN, along with the description of the SED-fitting code used for our study. Finally, the results obtained through fitting photometric data of our sources will be presented.

4.1 Emission components

Realistic models reproducing AGN emission need to take into account the effects of three different components: the populations of stars of different age and chemical composition which compose the galaxy, the diffuse interstellar medium (ISM) that reprocesses the starlight, and the emission from the AGN which can be direct and/or reprocessed by dust.

4.1.1 Stars

Stellar emission contributes mostly in the UV, optical and NIR regimes, i.e. between ~ 0.3 and ~ 5 μm. Stars populating galaxies, which are not resolvable in individual sources, are usually represented as groups of stars born at the same time and with the same metallicity, the so-called simple stellar populations (SSPs). Actually, integrated spectra of galaxies are the results of contributions from stars with a wide range in metallicity, age and mass. Even if the case of a SSP is not realistic, it is possible to decompose the spectral energy distribution into various SSPs. Calculating the flux emitted by a SSP requires several fundamental elements:

- First of all, a large grid of evolutionary tracks created by modelling the evolution of stars for different initial masses and metallicities. These tracks define the path of a star in the Hertzsprung-Russel diagram (HRD) as a function of time.
- Secondly, isochrones of a given age t', i.e. lines in the HRD that connect the points belonging to the various evolutionary tracks where $t = t'$. The number of stars of a certain mass along the isochrones is governed by the initial mass function (IMF), which describes the distribution in mass of a stellar population and is assumed to be a simple power of the mass: $dN \propto m^{-x} dm$, where the index x defines the slope of the IMF.
- Thirdly, libraries of stellar spectra covering a wide range of stellar parameters, in order to determine the flux of the stars along the isochrones.

Four main parameters describe a SSP: age (t), composition (X,Y,Z) and the initial mass function (IMF). Lastly, the total spectrum of a SSP can be derived by integrating the contributions of all the stars with mass M, age t and metallicity Z:

$$S_\nu(t, Z) = \int_{M_L}^{M_U(t)} S_\nu(M, t, Z)\Phi(M)\, dM \tag{4.1}$$

where $S_\nu(M, t, Z)$ is the monochromatic flux emitted by an individual star and $\Phi(M) = dN/dm$ is the IMF. The integral is computed in a given range of masses: M_L is the mass of the lowest mass star in the SSP, whereas $M_U(t)$ is the mass of the highest mass star still alive in the SSP of age t. On the one hand, the most abundant stars in galaxies are the less massive, which contribute mainly in the NIR. On the other hand, the most massive, luminous stars are also the less abundant and their emission can dominate the spectrum of the galaxy in the UV-optical range. Fig. 4.1 shows the evolution of a standard SSP spectrum as a function of time: the spectrum, at different times, is the sum over all spectra of the stars along an isochrone. Initially, the spectrum and luminosity are dominated by the most massive stars emitting intense UV radiation. The UV flux diminishes as time proceeds, since massive stars evolve rapidly. After $\sim 10^8$ yr the emission shortwards of 1000 Å is almost completely disappeared and massive stars evolved in red supergiants dominate the NIR regime. After $\sim 10^9$ yr red giant stars account for most of the NIR emission and afterwards the SSP spectrum, dominated by less massive stars, evolves slightly.

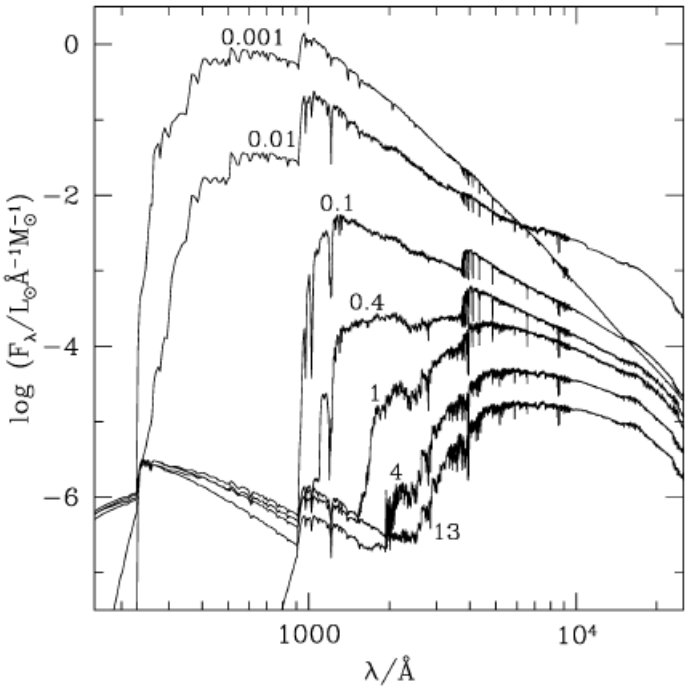

Figure 4.1: Spectral evolution of a standard SSP spectrum with solar metallicity. Time is given in units of 10^9 yr (from Bruzual & Charlot 2003).

As for the IMF, it ranges between a minimun and a maximum stellar mass: the

lower limit is usually 0.1 $M_\odot$, which is roughly the minimum mass of a star capable of activating the hydrogen burning; the upper limit is ~ 100 $M_\odot$. In addition, there are various alternatives for the shape of the IMF, defined by the index x: e.g. the Salpeter IMF (1955) with $x = 2.35$, the three-power form IMF by Kroupa et al. (1993) and the double power law by Chabrier (2003). However, its real shape over all conditions and redshift is still an open question.

4.1.2 Interstellar medium

The interstellar medium (ISM) has an important effect on the observed SEDs, as it processes the stellar radiation through different physical mechanisms. When light passes through a medium, its intensity changes as a result of emission, absorption and scattering by the medium itself. Therefore, accounting for the radiative transfer of the stellar light through the ISM, as well as the contribution of the ISM itself, is necessary in order to describe properly the SEDs of galaxies.

The ISM is composed of gas and dust particles. The interstellar gas constitutes about the 99% of the ISM mass and is usually treated in atomic form in the modelling of galaxies. It reprocesses extreme-UV light into strong emission lines, which are significant in actively star-forming galaxies. Clearly, there is also a molecular component but it has a low volume filling factor, hence its contribution is negligible when its opacity in the overall galaxy emission is considered. However, it is important to highlight that its contribution to the opacity becomes noticeable in particularly obscured sources such as AGN or ULIRGs. Its emission, instead, is mostly seen at NIR wavelengths and is due to heating by the diffuse stellar radiation field produced by newly formed stars (Walcher et al. 2011).

The interstellar dust is composed of graphitic carbon grains, silicate grains and polycyclic aromatic hydrocarbons (PAHs). A grain size distribution is necessary in order to model dust emission, whose general expression is:

$$dN(a) = 10^{A_i} a^q da \tag{4.2}$$

where $dN(a)$ is the number of grains with size between a and $a + da$, while the coefficient A_i fixes the abundances of graphite and silicates with respect to the abundance of hydrogen. The parameter q defines the extinction curve and it is equal to -3.5 for the Mathis-Rumpl-Nordisieck (MNR) distribution (Mathis et al. 1977). Therefore, dust is dominated in number by small grains. Moreover, we have to take into account the interactions between dust and electromagnetic radiation through

interstellar extinction, namely a combination of absorption and scattering of the radiation. Indeed, dust grains absorb photons whose wavelength is comparable to, or smaller than, their characteristic size, varying from about 0.005 μm to about 1 μm for graphite. This attenuation of the source intrinsic flux is, thus, wavelength dependent and is parametrized by the reddening curve:

$$k(\lambda) = \frac{A_\lambda}{E(B-V)} \tag{4.3}$$

where $A_\lambda = -2.5 \log (F_{\lambda,obs}/F_{\lambda,intr})$ is the wavelength dependent total extinction, i.e. it is a measure of the reduction of the intrinsic flux as a result of absorption and scattering processes. It depends on the line of sight as well as on the nature and the geometrical distribution of the dust grains. $E(B-V)$ is the color excess between the B and V bands and is defined as the difference between the observed and the intrinsic color index $B-V$. In particular, the strength of the interstellar extinction decreases from short to long wavelengths. The slope of the extinction curve in the V band is measured as:

$$R_V = \frac{A_V}{E(B-V)}. \tag{4.4}$$

Extinction laws have been measured for the Milky Way, with $R_V = 3.1$, as well as the Small and Large Magellanic Clouds, $R_V = 2.72$ and 2.76 respectively. In addition, an empirical curve for starburst galaxies was derived by Calzetti et al. (1994), with $R_V = 4.05$. Silicate grains contribute with absorption features at 9.7 and 18 μm usually observed in type 2 SEDs, while graphite produces an absorption at 2175 Å, visible as a bump in some extinction curves. Fig. 4.2 shows several extinction curves for the different R_V mentioned above.

Dust contributes to the overall SED in emission as well. PAH molecules emit strong features in the MIR at specific wavelengths (3.3, 6.3, 7.7, 8.6, 11.3 and 12.7 μm), as a result of the absorption of UV/optical photons which produce vibrational transitions. Moreover, the radiation absorbed by the grains at UV/optical wavelengths is re-radiated in infrared and sub-mm. In particular, the bulk of the cold dust emission heated by starburst activity is in the FIR and sub-mm regimes. A general result of the modelling is that emission at $\lambda \geq 100$ μm is mostly due to dust heated at thermal equilibrium by the interstellar radiation field (Bianchi 2013). If all dust grains have the same size and composition, their emission can be represented as a single temperature modified blackbody:

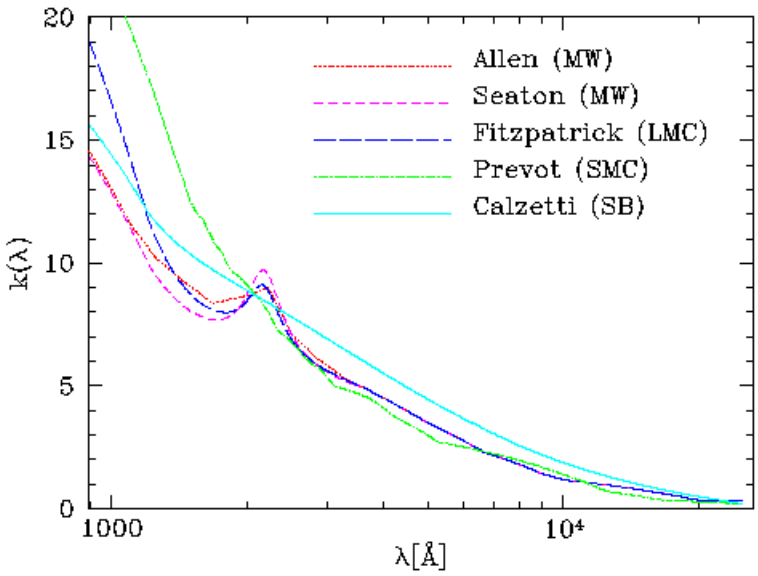

Figure 4.2: Extinction curve $k(\lambda)$ for different reddening laws as indicated in the legend (from Hyperz User's Manual, http://webast.ast.obs-mip.fr/hyperz/).

$$S_\nu \propto B_\nu(T_{\rm dust})\kappa_\nu M_{\rm d} \tag{4.5}$$

which is the flux density, derived from the radiative transfer solution, of a source under the assumption of thermal equilibrium and in the optically thin regime, occurring at long wavelengths. $B_\nu(T_{\rm dust})$ is the Planck function, $M_{\rm d}$ is the dust mass and κ_ν is the dust absorption coefficient per unit mass (in units of cm^2 g^{-1}), commonly taken to be a power law, $\kappa_\nu = \kappa_0(\nu/\nu_0)^\beta$, where k_0 is the value of the dust absorption coefficient given at a fixed frequency ν_0. The spectral index β is a function of grain size, composition, as well as temperature, and is 0 for a blackbody and in the range $1-2$ for a modified blackbody. However, the optically thin regime is not always valid, since some distant SMGs along with the local ULIRG Arp220 have a FIR emission consistent with a modified blackbody in the optically thick regime $S_\nu \propto B_\nu(T_{\rm dust})(1-e^{-\tau_\nu})$[1] (Rangwala et al. 2011). Actually, a realistic dust model should include grains of different sizes and compositions, as well as the range of temperature shown by the dust in the ISM, from the hot dust surrounding young stars and the active nucleus to the cold dust in cold molecular cores. To derive the overall dust emission, complex models integrate the emission for each grain size and composition, given a dust distribution. However, empirical templates of FIR

[1]From this equation, with the optical depth $\tau_\nu \ll 1$ and $d\tau = \rho_{\rm d}\kappa_\nu dl$, where $\rho_{\rm d}$ is the dust density, the relation (4.5) is obtained.

emission of galaxies are often employed to reproduce the galaxy SEDs, as the temperature distribution in complex models depends on the dust-gas geometry of the ISM, which requires high-resolution observations (Walcher et al. 2011).

4.1.3 AGN

The contribution of the active nucleus to the UV to IR SED is different depending on the viewing angle. For type-2 AGN it is due to thermal emission from circumnuclear hot dust which absorbs the AGN primary emission and re-emits it in the MIR, i.e. at $\lambda \sim 3 - 40$ μm. For type-1 objects the emission from the accretion disc is directly visible and thus it also dominates in the UV-optical regime, overwhelming the host galaxy emission. The hot dust emission, as in type-2 AGN, is present as well. However, our sample is composed of type-2 sources, hence our main interest resides in characterizing the dust emission. In this regard there is a very debated issue concerning the geometry of the dust distribution. We find in the literature two main types of models reproducing dust emission, as first proposed by Barvainis (1987) to reproduce the overall shape of the near-infrared bump in the AGN SEDs: a continuous distribution, referred to as "smooth", and a distribution in which dust is clumped into discrete clouds, referred to as "clumpy". Ascribing one of these two distributions to the observed emission is not straightforward, as the small angular size of the torus requires very high angular resolution to study its properties.

Recently, the extent and morphology of the nuclear dust distribution have been probed through high-resolution interferometric observations in the mid-infrared. The nuclear region has been resolved for some bright and nearby AGN and the results point to a clumpy or filamentary dust structure (e.g. Tristram et al. 2007, Burtscher et al. 2013). Further evidence of a clumpy distribution is provided by observations of variability of the X-ray absorbing gas in nearby AGN on timescales from days to years, due to Compton-thick clouds crossing the line of sight towards the central nucleus (e.g. Risaliti et al. 2007). Actually, this obscuration is attributed to dust-free clouds inside the dust sublimation radius, but they may be considered an inward extension of the torus. However, there are also studies supporting a smooth distribution: Leverson et al. (2007), for instance, studied the spectra of a sample of ULIRGs and found that the deep absorptions due to silicate grains requires a smooth distribution of material to be reproduced.

There is a popular model for each of the two classes, namely the smooth model by Fritz et al. (2006; see also Feltre 2013) and the clumpy model by Nenkova et al.

(2008a,b). Although a cumply structure is more realistic, both models are widely used in the literature providing a good reproduction of the observed SEDs of AGN, even though both present still unresolved issues. In particular, we analyzed our sources by means of the smooth model. It was extensively used in various analyses at different redshifts (e.g. Hatziminaoglou et al. 2010, Vignali et al. 2011, Pozzi et al. 2012) and is suitable for the purpose of our work, as we aim at constraining photometric SEDs as well as determining the physical properties of our sources. We refer to the specific papers for a detailed description of the models, however we summarize briefly some of their most important characteristics, especially focusing on the former.

Smooth model Fritz et al. use a flared disc geometry, represented as two concentric spheres without their polar cones, which delimit the inner and the outer radii (Fig. 4.3). The inner radius is the distance where the dust grains, exposed to the nuclear radiation field, reach the sublimation temperature (Barvainis 1987):

$$R_{\rm min} \simeq 1.3\sqrt{L_{46}^{AGN}}T_{1500}^{-2.8} \quad ({\rm pc}) \tag{4.6}$$

where L_{46}^{AGN} is the bolometric luminosity[2] of the central source in units of 10^{46} erg s^{-1} and T_{1500} is the sublimation temperature of the dust grains in units of 1500 K. Dust is composed of silicate and graphite grains and their distribution function is that given in Mathis et al. (1977). The different sublimation temperatures are accounted for, namely $\sim$1100 K for silicates and $\sim$1500 K for graphite. The torus density is variable along the radial and the angular coordinates:

$$\rho(r,\theta) = \alpha r^{\beta} e^{-\gamma|\cos\theta|} \tag{4.7}$$

where the normalization constant α is established by the equatorial optical depth at 9.7 μm, β defines the distribution of the dust along the radial coordinate and γ along the angular one.

The central energy source is assumed point-like and characterized by an isotropic emission, described as a composition of power laws with different indices:

[2]The AGN bolometric luminosity is almost entirely produced by the UV/optical light.

$$L(\lambda) \propto \begin{cases} \lambda^{1} & \text{if } 0.001 < \lambda < 0.03 \ [\mu\text{m}] \\ \lambda^{-0.2} & \text{if } 0.03 < \lambda < 0.125 \ [\mu\text{m}] \\ \lambda^{-1.5} & \text{if } 0.125 < \lambda < 10.0 \ [\mu\text{m}] \\ \lambda^{-4} & \text{if } \lambda > 10.0 \ [\mu\text{m}]. \end{cases} \tag{4.8}$$

The torus is divided into volume elements and the overall spectrum is calculated adding the emission from all the elements to that of the central source. The model accounts for absorption, emission as well as scattering by solving numerically the radiative transfer problem.

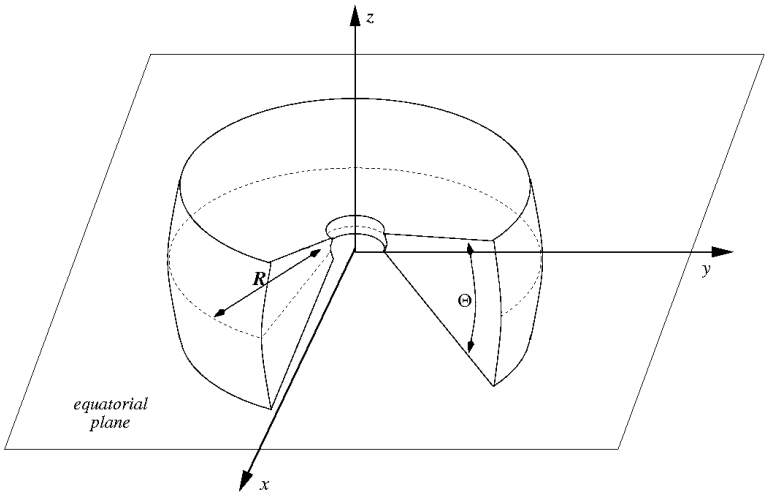

Figure 4.3: Geometry of the smooth torus of Fritz et al. (2006). In the figure R is the radial size and Θ is the torus full-opening angle.

Clumpy model Nenkova et al. consider dust clumped in identical clouds set in a Gaussian angular distribution (Fig. 4.4), where the total number of clouds along a direction at angle β from the equator is defined as:

$$\mathcal{N}_T(\beta) = \mathcal{N}_0 \exp(-\beta^2/\sigma^2) \tag{4.9}$$

with σ the width parameter of the distribution and $\mathcal{N}_0$ the number of clouds along the equatorial direction. The inner radius is defined as:

$$R_{\rm d} \simeq 0.4 \left(\frac{L}{10^{45}\ \text{erg}^{-1}} \right)^{1/2} \left(\frac{1500\ \text{K}}{T_{\rm sub}} \right)^{2.6} \quad (\text{pc}), \tag{4.10}$$

similar to the relation (4.6). Since the clouds are much smaller than the torus extension, they are considered as point sources with a given optical depth τ_λ. The primary emission, reproduced by a piecewise power-law distribution, heats directly a certain number of clouds which re-emit it at longer wavelengths, thus producing a diffuse radiation field in which the indirectly illuminated clouds are placed. The emission from the clumpy torus is calculated through integration of the AGN and cloud contributions, by solving the radiative transfer problem for each cloud.

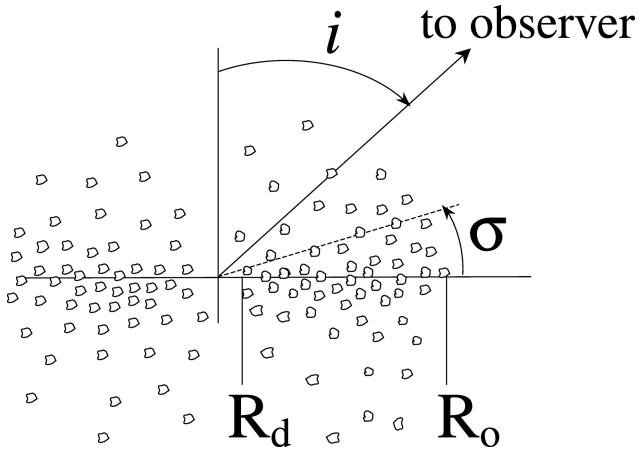

Figure 4.4: Geometry of the clumpy torus of Nenkova et al. (2008b). R_d and R_O are the inner and outer radii respectively. i is the viewing angle measured from the torus axis and σ is the width of the Gaussian angular distribution of the clouds.

In contrast with a smooth distribution, where the dust temperature only depends on the distance from the AGN, a clumpy distribution presents some fundamental differences in this regard. Clouds heated directly by the AGN will have a higher temperature on the illuminated face than on the opposite one and its emission will be strongly anisotropic; a more uniform emission is produced by clouds heated by the diffuse radiation field. Therefore, we can find different temperatures at the same distance from the AGN and the same dust temperature at different distances, e.g. considering the bright side of a further cloud and the dark side of a closer cloud which might have the same temperature. Moreover, the observed torus emission is determined by the inclination of the line of sight in the smooth model, while it is also related to the probability of encountering more or less clouds in the clumpy model. A thorough comparison between these two models, considering matched parameters, was performed by Feltre et al. (2012). They claim that the majority of the differences in the SEDs produced by the models are mainly due to the different

model assumptions (e.g. distribution of the primary source emission, dust chemical composition, etc.) and not to the clumpiness or smoothness of the dust distribution. However, in the present work we focus on the global characteristics of the SED and not on the details of the torus structure and geometry, hence the adopted model does not influence our results.

4.2 The SED-fitting tool

We analyzed our sources by using the SED-fitting code originally presented by Fritz et al. (2006) and Hatziminaoglou et al. (2008), and improved by Feltre (2013). This is an adaptable tool capable of dealing with different datasets as well as using a wide spectral range, between 10^{-2} and 10^{3} μm. For a detailed description of the code we refer to Feltre (2013), but here we summarize some of its major characteristics.

The code makes use of a multi-component approach, accounting for three emission components: stellar emission, hot dust emission heated by AGN activity and cold dust emission heated by starburst phenomena. The first component prevails mostly between ~ 0.3 and ~ 5 μm (rest-frame). It is modelled with a set of SSPs constructed by using "Padova" evolutionary tracks (Bertelli et al. 1994), a Salpeter IMF with masses in the range $0.15 - 120$ $M_{\odot}$ and the Jacoby et al. (1984) library of observed stellar spectra in the optical regime. The extension to the UV and IR range is given by the Kurucz (1993) theoretical libraries. Moreover, dust emission from stellar envelopes by Bressan et al. (1998) was included. The SSP ages are in the range between 10^{5} and $1{\times}10^{10}$ yr with five different metallicity values in the range between 0.0004 and 0.02. The effect of extinction is also taken into account with the possibility of choosing different extinction curves. The stellar component is introduced by convolving the SSP fluxes with the star formation history (SFH) of the galaxy. It describes how the star formation rate (SFR), i.e. the total stellar mass formed per unit time, varies as a function of time. The SFH is purpose-built with an exponentially declining trend (the so-called direct-τ model):

$$SFR(t) = \left(\frac{T_G - t}{T_G}\right) \exp\left(-\frac{T_G - t}{T_G \cdot \tau_B}\right) \tag{4.11}$$

where T_G is the age of the galaxy (or the age of the oldest SSP) which depends on the redshift of formation and τ_B is the duration of the initial burst normalized to the age of the galaxy. This relation derives from the Schmidt law (Schmidt 1959), which was obtained by considering that the SFR depends on gas density and assuming that

it varies with a power of the gas density itself:

$$SFR \propto \frac{d\rho_g}{dt} \propto \rho_g^n. \tag{4.12}$$

If $n \sim 1$, such a law produces an exponentially declining SFH. This simple model provides a reasonable description of the SFH of many galaxies, therefore this approximation is often adopted in evolutionary synthesis models (Kennicutt et al. 1996).

The AGN component is due to the dusty torus heated by the central source, whose emission peaks in the MIR. It is possible to fit this component with either the smooth torus by Fritz et al. (2006) or the clumpy torus by Nenkova et al. (2008a,b).

Finally, the cold dust component contributing at wavelengths $\gtrsim 30$ μm can be reproduced by different models:

- Empirical templates representative of starburst galaxies, such as Arp220, M82, M81, NGC4102, etc. By using this empirical approach it is not possible to derive specific physical properties of the cold dust but only the contribution of the starburst component to the total IR luminosity.

- Dusty SSP models by Piovan et al. (2006a,b). Their models take into account the effect produced by dust on the radiation emitted by SSPs. This is especially important when young stars are present, as they are embedded in dusty star forming region and, hence, heavily extincted. Thus, the radiation subtracted from stars comes out in the FIR band. On the contrary, empirical templates ignore this balance.

The fit is performed one component at a time in the observed data frame, therefore the model SED is shifted to the redshift of the object, taking into account the K-correction in order to compare flux densities. First of all, the code fits the FIR range if there are data points at $\lambda > 24$ μm. This is an arbitrary choice, however the starburst contribution shortward of this value is small and usually the torus gives a dominant contribution to this range. Secondly, the UV/optical part of the SED is considered. The fit with the stellar component at wavelengths up to 1.6 μm is taken into account if the χ^2_r is smaller than a given value. Otherwise, this part of the SED is fitted with a type-1 AGN component. Finally, the best AGN model is looked for by exploring the whole grid of models. If the stellar component has been included, the fit is performed in the mid-IR regime. The last step is

a simultaneous perturbation of the normalization constant values provided by the best fits, in order to improve the final results. As explained by Pozzi et al. (2012), the free parameters of the SED-fitting procedure are numerous: six are related to the AGN, two to the stellar component, one to the starburst and two further free parameters are represented by the normalizations of the stellar and of the starburst components. The torus normalization, instead, is estimated by difference, as it is considered once the other components have already been included. Overall, the free parameters are eleven. In particular, the torus model parameters (described in detail by Feltre et al. 2012) are the ratio $R_{\rm max}/R_{\rm min}$ between the outer and the inner radius of the torus (with $R_{\rm min}$ defined by the sublimation temperature of the dust grains, Eq. (4.6)); the torus opening angle Θ; the optical depth τ at 9.7 μm ($\tau_{9.7}$); the inclination of the line of sight with respect to the equatorial plane, θ; β and γ, which describe the spatial distribution of the dust. However, these parameters are subject to degeneracies, as different combinations can reproduce equally well a set of observed datapoints. As for the parameters related to the stellar emission, τ_B is the parameter of the exponential law for the star formation, while $E(B-V)$ is the reddening.

The determination of the best fit is carried out by a standard χ^2 minimization. As discussed in Vignali et al. (2009), the goodness of the fit is evaluated by means of a "merit function" which can be considered as a modified reduced χ^2, where the number of degrees of freedom is replaced by the number of photometric points building up the SED. This quantity is defined as:

$$\chi^2_{MF} = \frac{1}{N_O} \sum_{i=1}^{N_O} \left(\frac{F_i^O - F_i^M}{\sigma_i} \right)^2 \tag{4.13}$$

where N_O is the number of observed data points, F_i^O and F_i^M are the observed and the model flux densities in the i-band, respectively. In particular, the F_i^M are calculated by convolving the filter response curve with the model flux. Finally, σ_i is the error of the observed flux in the i-band.

The computed values of χ^2_{MF} could result very high due to the relatively small photometric errors in some cases and to the complexity of the spectral fitting, performed with limited grids of models and spectral libraries. The most important output parameters are the stellar mass, the total infrared luminosity between 8 and 1000 μm and the AGN bolometric luminosity.

4.3 Results

To fit the overall SEDs of our sources, the stellar component was modelled by means of a set of SSPs with solar metallicity whose age ranges between the formation redshift of the galaxy z_{form} and the source redshift z. The adopted z_{form} are in the range $6-9$. As for starlight extinction, the Calzetti attenuation law has been used, applying a common value of extinction to stars at all ages. Finally, the AGN component has been reproduced using the smooth torus geometry of Fritz et al. (2006), and the FIR emission using both empirical templates and dusty SSPs. We were able to derive the following relevant physical parameters of both the host galaxy and the AGN, reported in Tables 4.1 and 4.2 for SED fitting performed with empirical starburst templates and dusty SSPs, respectively: M_*, stellar mass of the galaxy; L_{IR}, total infrared luminosity integrated between 8 and 1000 μm rest-frame; L_{bol}, AGN bolometric luminosity produced by accretion; τ_B, duration of the initial burst of star formation in units of T_G (the age of the galaxy); $E(B-V)$, total extinction to the stellar population; AGN fraction, fractional AGN contribution to the total infrared luminosity observed in the range $8-1000$ μm.

Our galaxies turn out to be very massive objects, with stellar masses in the range $(0.8-4)\times10^{11}$ $M_\odot$ and characterized by an intense IR emission, $L_{IR} = [(2-7)\times10^{12}]$ $L_\odot$. The bolometric AGN luminosities are $\sim10^{46}$ erg s^{-1}; the AGN contributes to the IR $[8-1000]\mu$m luminosity up to few tens %. The galaxy lifetime spent in star formation ranges between 0.2 and 0.5 times the age of the galaxy. Most of the sources require a significant extinction to the host galaxy emission, $E(B-V) = [0.1-0.3]$. As expected, the χ^2_{MF} values are high. This kind of problem is not unusual in SED-fitting analyses: it can be ascribed to the combination of photometric measurements with different uncertainties as well as the "discretization" of the template grids used in the fitting procedure. Indeed, the template libraries used to fit photometric data include a finite number of SEDs, not covering with continuity the parameter space. A thorough discussion on this issue was presented by Gruppioni et al. (2008), who considered the total uncertainty on both the photometric data and the template SEDs by varying the small photometric errors of their photometric data to determine new photometric uncertainties. The enlarged relative errors obtained, ranges from $\sim15\%$ in the optical/mid-IR bands up to $\sim20\%$ in the mid and far-IR. In our analysis, we determined the uncertainties on the main best-fit parameters by considering all the acceptable solutions within 1σ confidence level, i.e. all the solutions with $\Delta\chi^2 = \chi^2 - \chi^2_{min} \lesssim 12.65$ (Lampton et al. 1976), considering the 11 degrees of

freedom of the SED-fitting procedure. The derived relative errors are of about 20% for the AGN bolometric luminosity and for the IR luminosity, while for the stellar masses they resulted to be of few %. This uncertainty is clearly underestimated and is of the order of the statistical errors on the photometric measurements. Comparisons of the stellar masses obtained through the code used in this analysis with other codes (adopting different libraries and IMFs) provided a relative error of $\sim 30\%$ (Feltre, private communication). Although the stellar mass is a crucial physical quantity, it suffers from systematic uncertainties, related to, e.g., the poor constraints on the stellar population properties (such as metallicity, extinction curves, IMF, as well as some phases of the stellar evolution) and the lack of a proper reconstruction of the SFH, translating into the necessity of several assumptions about these parameters. A comprehensive description of these aspects was presented by Santini et al. (2015), who investigated the influence of systematic effects due to different assumptions in the stellar mass estimates. Ten teams within the CANDELS collaboration computed the stellar mass for the sources observed in the CANDELS field (where our sources lie) by fitting the same photometry but adopting different codes and assumptions (in terms of SFH, IMF, template libraries, parameter grid sampling, etc.). The comparison among the resulting estimates is quite satisfactory, with the majority of the results around the median value. Hence, they claimed that the stellar mass is a stable parameter against the different assumptions, except for the IMF, which introduces a constant offset (in order to rescale to the Chabrier IMF, 0.24 dex needs to be subtracted from the stellar masses computed assuming the Salpeter IMF). They also quantified the scatter around the median value, which is roughly $25-35\%$. We compared our measurements with the results presented in their GOODS-S catalog[3], in particular with the median values and the results obtained with the method whose assumptions are more similar to ours (method $2d_\tau$ in Santini et al. 2015), i.e. the χ^2 minimization to estimate the goodness of fit, the Salpeter IMF, an exponentially declining SFH and the Calzetti extinction law. Our values result to be larger by a factor ~ 2.5 with respect to the median stellar mass, while the results of the method $2d_\tau$ provide an excellent agreement. Moreover, if we rescale our measurements to the Chabrier IMF (used by all methods but two), our results differ by a factor 1.8 at most.

Overall, the fits are extremely good and the SEDs whose FIR regime has been fitted with empirical templates show a smaller $\chi^2_{\rm MF}$, except for the source XID403,

[3]http://candels.ucolick.org/data_access/GOODS-S.html.

characterized by a lower $\chi^2_{\rm MF}$ when fitted with dusty SSP models, in agreement with the result obtained by Gilli et al. (2014). The optical/NIR regime of our SEDs is well sampled by several photometric datapoints allowing the code to constrain tightly the stellar component. Only one datapoint (the *Spitzer*/MIPS at 24 μm) accounts for the AGN component, but our analysis points out that it is necessary to reproduce the observed emission. The FIR part of the SEDs is sampled differently for the different sources. The source XID490 has the best covered FIR regime (Fig. 4.9) thanks to *Herschel*/PACS and SPIRE photometry, along with SCUBA and ALMA submm data. In particular, the SED fitted with empirical templates is, by far, better than that fitted with dusty SSPs, as confirmed by the statistic values. The other sources present less sampled FIR SEDs, but are reproduced quite well: XID34, XID403 and XID412 present *Herschel*/PACS and SPIRE as well as ALMA observations, hence the declining part of the FIR peak is constrained by at least one photometric point (Figs. 4.5, 4.7 and 4.8, respectively); while for XID546, *Spitzer*/MIPS as well as *Herschel*/PACS and SPIRE measurements sample only the "increasing" part (i.e., the Wien regime of the modified black body emission) of the FIR emission (Fig. 4.10). Constraining the FIR emission peak is of fundamental importance, especially the "decreasing" part, since it corresponds to the Rayleigh-Jeans tail, where the dust is in the optically thin regime. Therefore, the dust continuum can be used as an indicator of the dust mass and, through the dust-to-gas ratio, of the ISM mass in the galaxy (see § 4.3.2, Scoville et al. 2016).

A particular case is that of the source XID262. The analysis of the ALMA band 7 image (870 μm), thanks to the high resolution ($\sim 0.2''$), revealed that the object, thought to be an individual source in the *Spitzer*/MIPS and *Herschel* maps (as well as in SCUBA observations, Mainieri et al. 2005), is actually a blend of two sources. The mid and far-infrared photometry is dominated by a bright object at $3.5''$ from the source, and forced us to exclude these datapoints. As a result, the MIR regime is completely unconstrained, while the FIR emission relies on a single photometric point from ALMA. Hence, the AGN component is extremely different for the two fits and this translates into different AGN contributions. In particular, as shown in Fig. 4.6, the AGN component is reproduced by either a sort of AGN with scattering (*top panel*), or a heavily obscured AGN (*bottom panel*).

Source	M_*	L_{IR}	L_{bol}	τ_B	$E(B-V)$	f_{AGN}	χ^2_{MF}
(a)	(b)	(c)	(d)	(e)	(f)	(g)	(f)
34	9.6×10^{10}	7.3×10^{12}	2.2×10^{12}	0.15	0.08	0.037	6.52
262	3.0×10^{11}	3.2×10^{12}	3.5×10^{12}	0.2	0.25	0.142	2.09
403	1.9×10^{11}	5.5×10^{12}	3.7×10^{12}	0.5	0.32	0.015	7.83
412	1.9×10^{11}	2.6×10^{12}	2.4×10^{12}	0.2	0.24	0.082	6.44
490	4.0×10^{11}	5.2×10^{12}	5.0×10^{12}	0.2	0.33	0.214	2.78
546	4.1×10^{11}	2.8×10^{12}	2.3×10^{12}	0.2	0.31	0.063	4.32

Table 4.1: Best-fit parameters of the spectral decomposition obtained using empirical templates to fit the FIR part of the SED. Relative errors are $\sim 30\%$ for stellar masses and $\sim 20\%$ for IR luminosities and AGN bolometric luminosities. $^{(a)}$ XID; $^{(b)}$ stellar mass, in units of $M_\odot$; $^{(c)}$ total infrared luminosity integrated between 8 and 1000 μm, in units of $L_\odot$; $^{(d)}$ AGN bolometric luminosity due to accretion, in units of $L_\odot$; $^{(e)}$ duration of the starburst activity in units of the age of the galaxy, T_G; $^{(f)}$ total extinction to the stellar populations; $^{(g)}$ fractional AGN contribution to the total IR luminosity; $^{(f)}$ goodness of the fit given in terms of the "merit function" described above.

Source	M_*	L_{IR}	L_{bol}	τ_B	$E(B-V)$	f_{AGN}	χ^2_{MF}
34	7.4×10^{10}	4.3×10^{12}	3.4×10^{12}	0.15	0.08	0.040	6.71
262	3.0×10^{11}	1.3×10^{12}	3.4×10^{12}	0.2	0.25	0.068	2.30
403	1.7×10^{11}	6.2×10^{12}	3.5×10^{12}	0.5	0.32	0.010	6.22
412	1.9×10^{11}	2.2×10^{12}	3.0×10^{12}	0.2	0.24	0.433	6.48
490	3.3×10^{11}	4.1×10^{12}	3.4×10^{12}	0.2	0.33	0.129	6.64
546	4.0×10^{11}	1.5×10^{12}	3.2×10^{12}	0.2	0.31	0.121	6.69

Table 4.2: Best-fit parameters of the spectral decomposition obtained using dusty SSP templates to fit the FIR part of the SED. Relative errors are $\sim 30\%$ for stellar masses and $\sim 20\%$ for IR luminosities and AGN bolometric luminosities. The columns are the same as in Table 4.1.

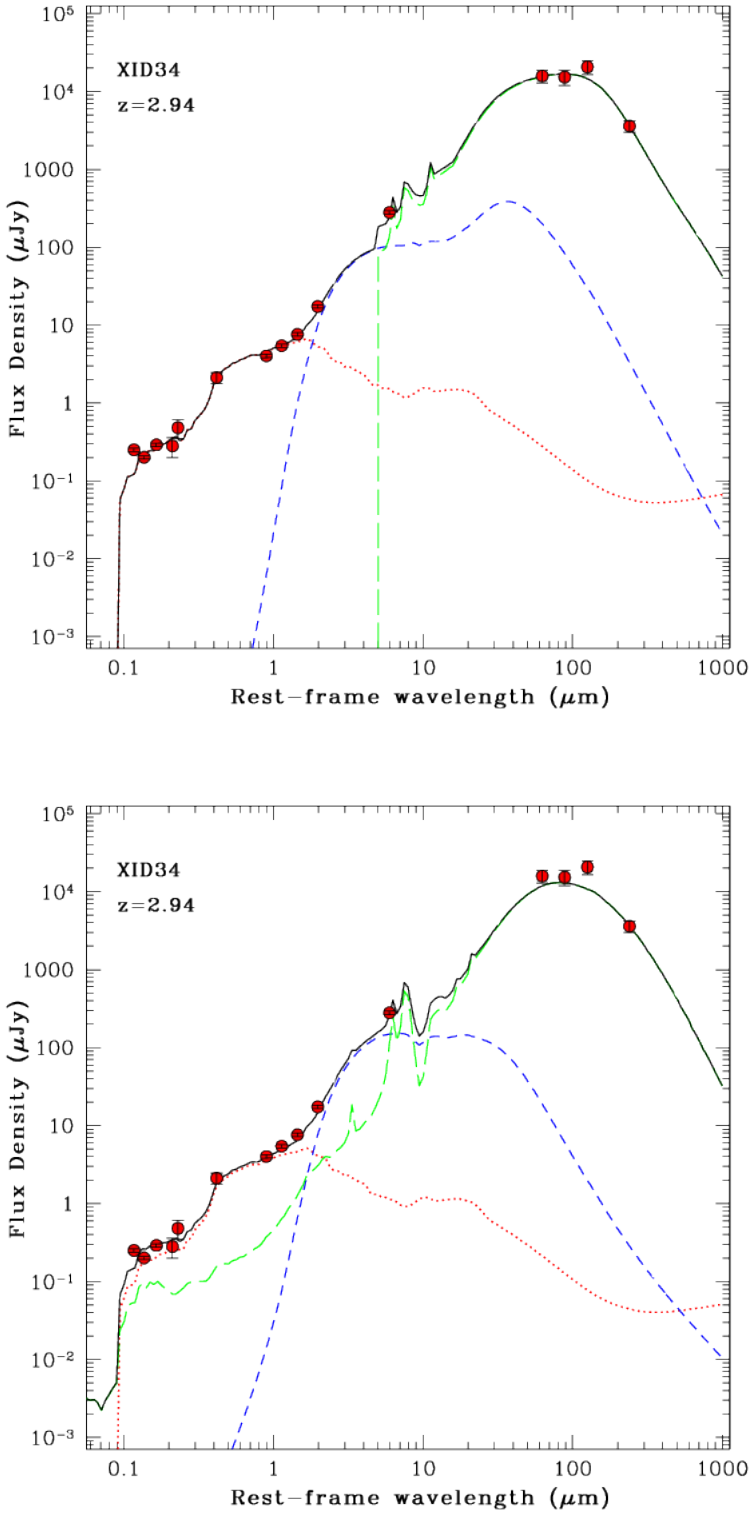

Figure 4.5: Spectral decomposition of the rest-frame SED of the source XID34. The red filled points are the photometric datapoints. The total SED (black solid line) is obtained by summing the contribution of the stellar (red dotted line), AGN (blue short-dashed line) and star-forming (green long-dashed line) components. In particular, empirical starburst templates (*top panel*) and dusty SSPs (*bottom panel*) have been used to fit the FIR part of the SED.

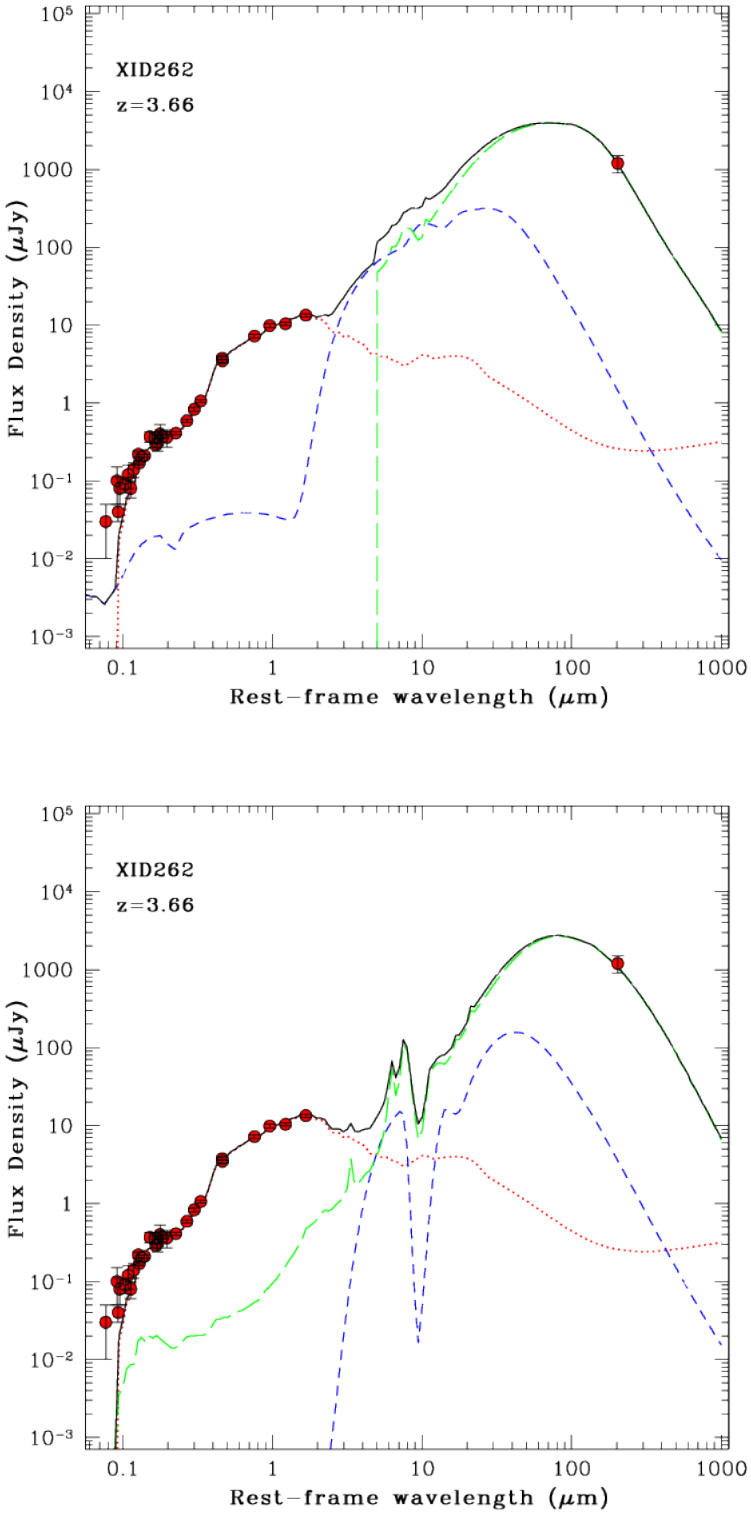

Figure 4.6: Spectral decomposition of the rest-frame SED of the source XID262. Symbols and line colors describing the different components are the same as in Fig. 4.5. Empirical starburst templates (*top panel*) and dusty SSPs (*bottom panel*) have been used to fit the FIR part of the SED.

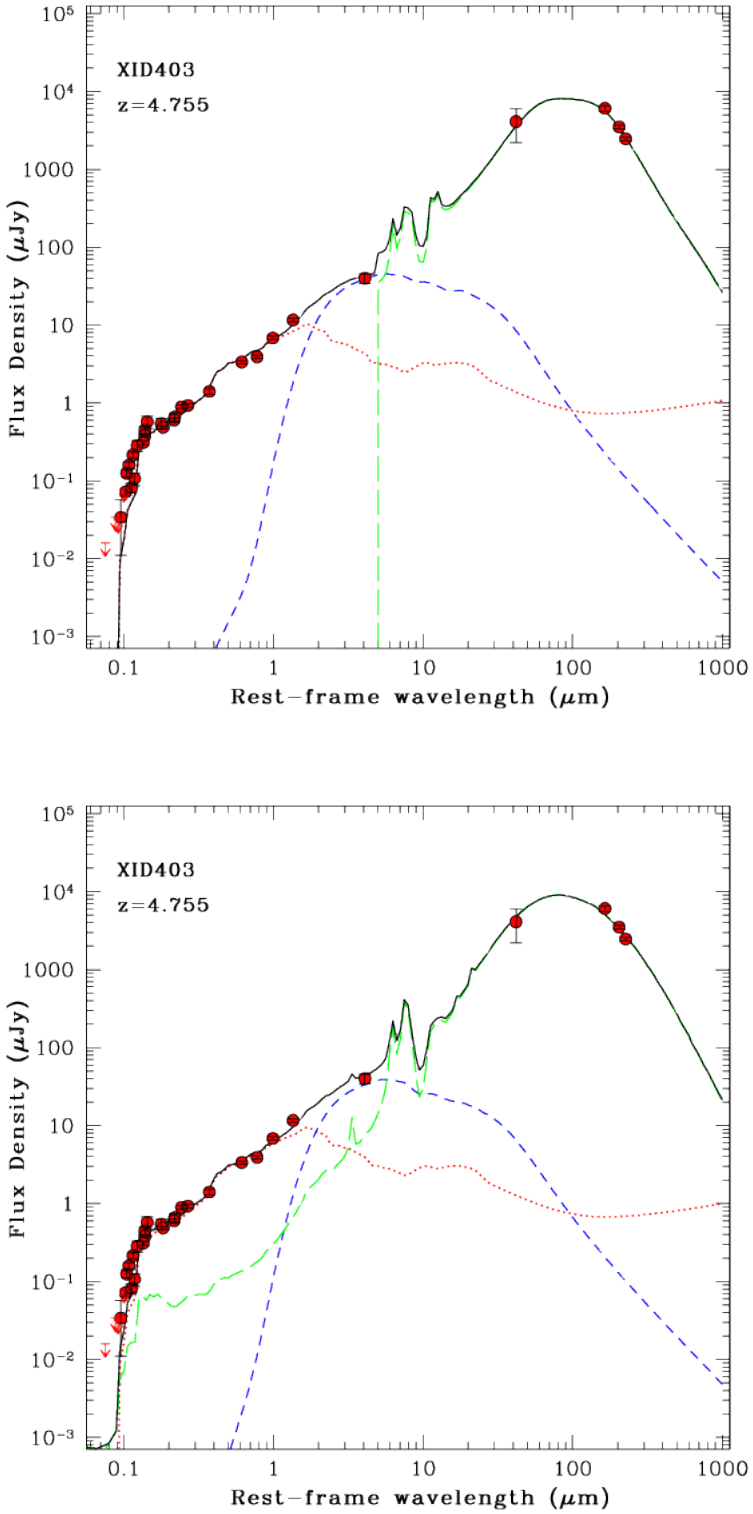

Figure 4.7: Spectral decomposition of the rest-frame SED of the source XID403. Symbols and line colors describing the different components are the same as in Fig. 4.5. Empirical starburst templates (*top panel*) and dusty SSPs (*bottom panel*) have been used to fit the FIR part of the SED.

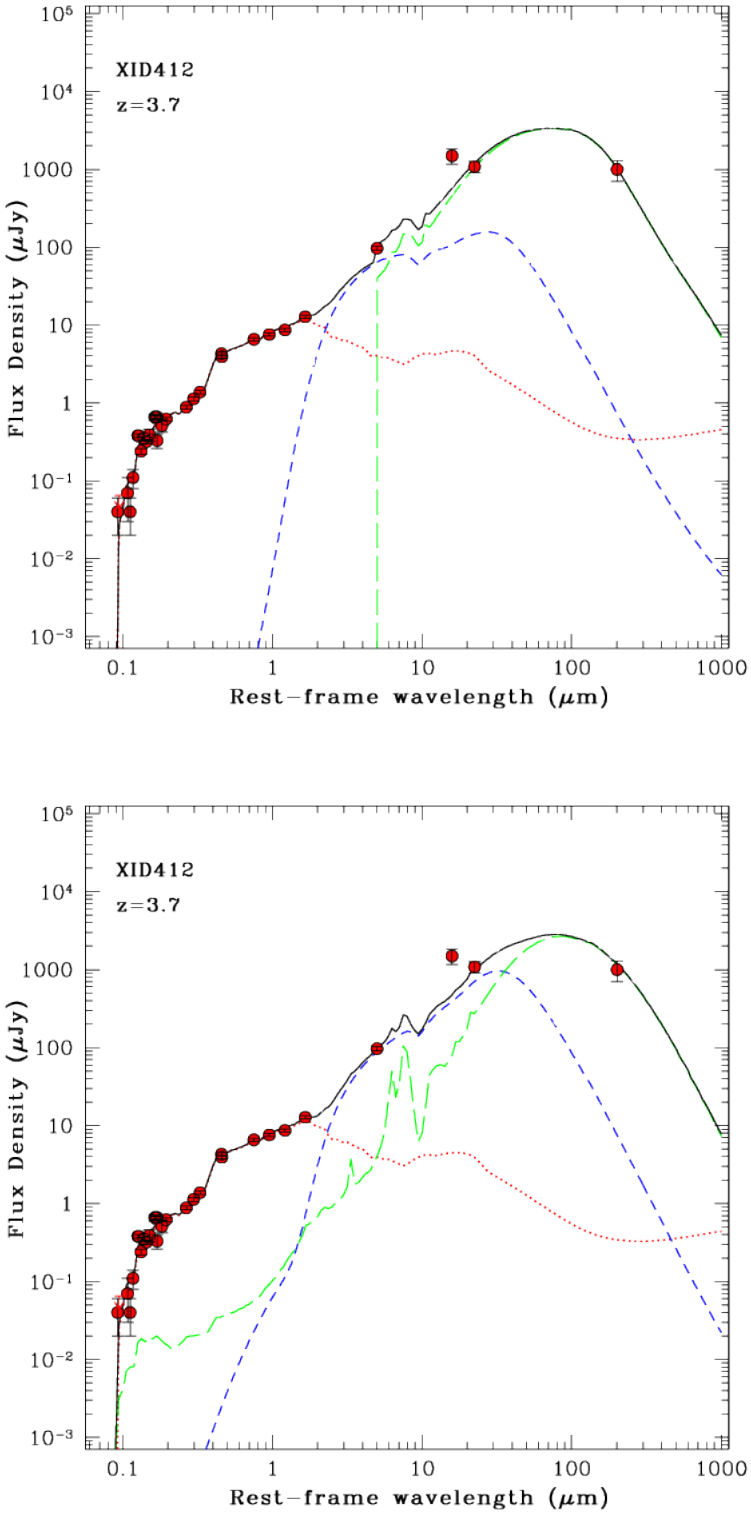

Figure 4.8: Spectral decomposition of the rest-frame SED of the source XID412. Symbols and line colors describing the different components are the same as in Fig. 4.5. Empirical starburst templates (*top panel*) and dusty SSPs (*bottom panel*) have been used to fit the FIR part of the SED.

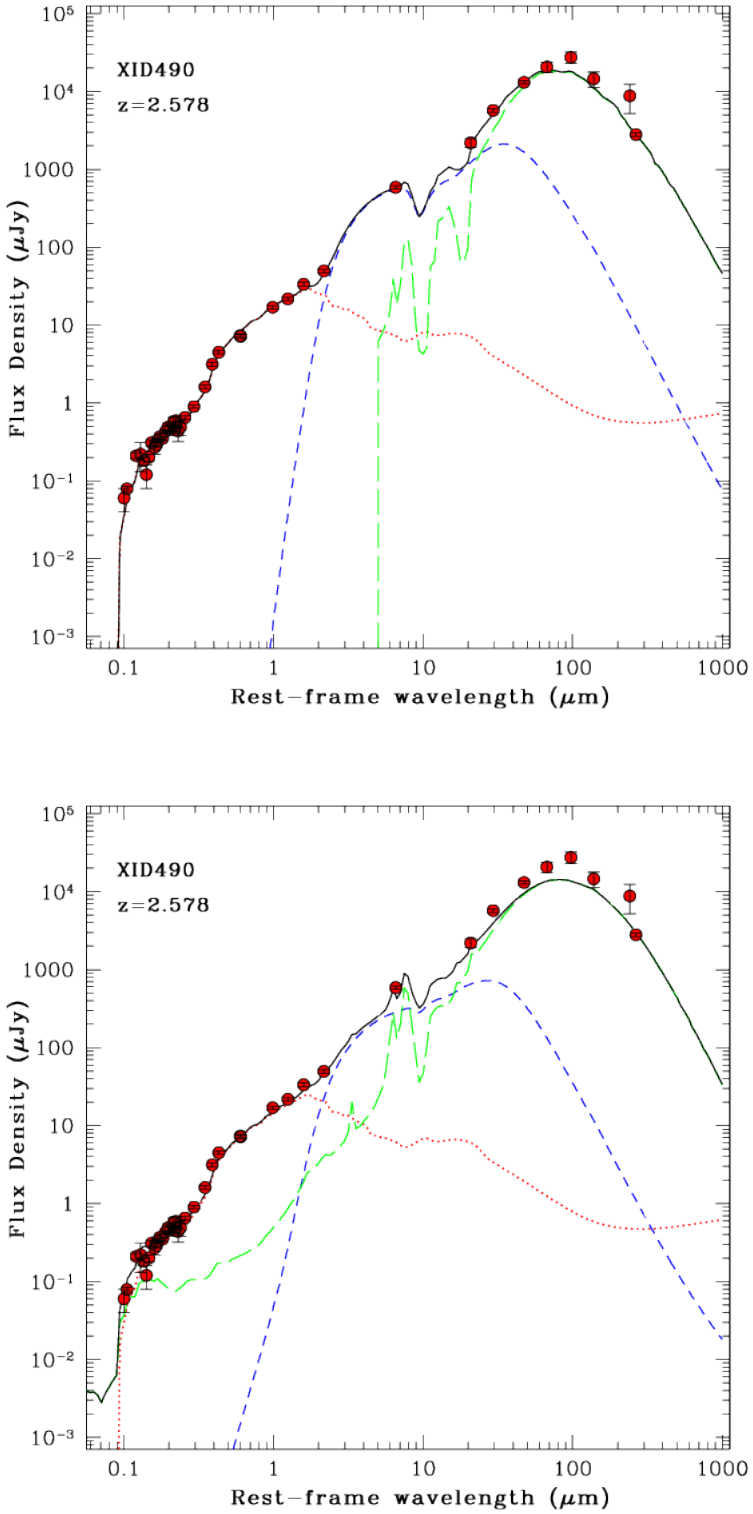

Figure 4.9: Spectral decomposition of the rest-frame SED of the source XID490. Symbols and line colors describing the different components are the same as in Fig. 4.5. Empirical starburst templates (*top panel*) and dusty SSPs (*bottom panel*) have been used to fit the FIR part of the SED.

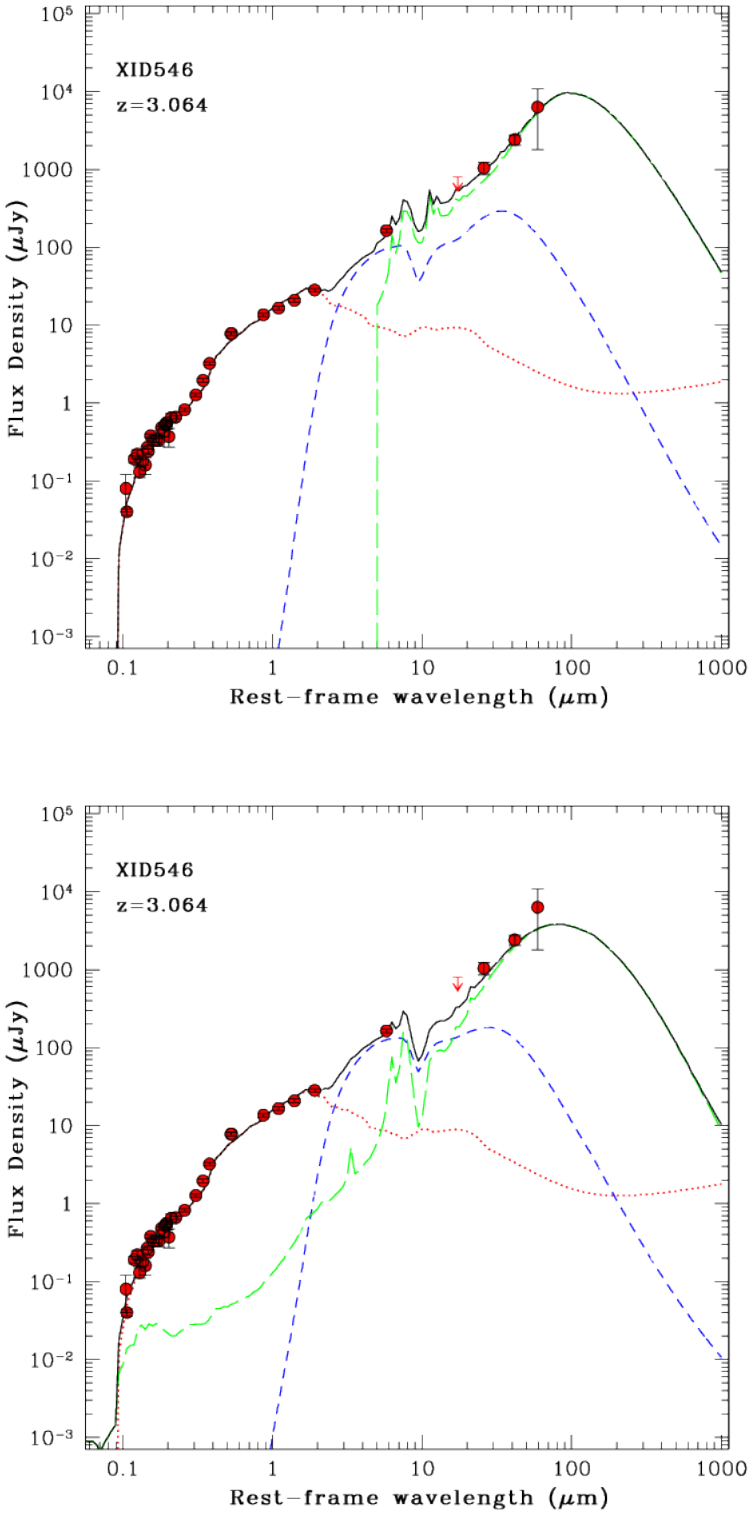

Figure 4.10: Spectral decomposition of the rest-frame SED of the source XID546. Symbols and line colors describing the different components are the same as in Fig. 4.5. The downward-pointing arrow marks a 3σ upper limit. Empirical starburst templates (*top panel*) and dusty SSPs (*bottom panel*) have been used to fit the FIR part of the SED.

4.3.1 X-ray luminosity tests

In order to test the solidity of the AGN luminosities, derived by both the X-ray spectral analysis and the SED fitting, we compared them with values predicted by two correlations between AGN properties. We first considered the luminosity relation found by Gandhi et al. (2009) between the MIR and X-ray AGN luminosities (see also Asmus et al. 2015 for an updated version of this correlation). Through high-resolution mid-IR continuum photometry they were able to probe the central regions (within $\sim 70-120$ pc) of a sample of local Seyfert galaxies, where the contamination from powerful SF is negligible and the AGN torus dominates the overall emission. They found that the luminosity at 12.3 μm ($\mathrm{L_{MIR}}$) is tightly correlated with the intrinsic X-ray luminosity in the [2 − 10 keV] band ($\mathrm{L_X}$) following an almost linear relation:

$$\log\left(\frac{L_{\mathrm{MIR}}}{10^{43}}\right) = (0.19 \pm 0.05) + (1.11 \pm 0.07)\log\left(\frac{L_{\mathrm{X}}}{10^{43}}\right) \tag{4.14}$$

where the luminosities are normalized to 10^{43} erg s^{-1}, the approximate mean power of the sample, and $\mathrm{L_{MIR}} = \lambda L_{\lambda}^{12.3}$. The scatter of this relation is $\sigma \sim 0.23$. We obtained $L_{\lambda}^{12.3}$ by computing the corresponding flux density $\mathrm{S}_{\nu_{12.3\mu\mathrm{m}}/(1+z)}$ from the model SED and then calculating the luminosity at 12.3 μm rest-frame through the relation (Hogg 1999):

$$\nu S_{\nu} = \frac{\nu_{\mathrm{e}} L_{\nu_{\mathrm{e}}}}{4\pi D_{\mathrm{L}}^2} \tag{4.15}$$

where $\nu_{\mathrm{e}} = \nu(1+z)$ is the emitted frequency, ν is the observed frequency and D_{L} is the luminosity distance. In Fig. 4.11 the X-ray luminosities derived through spectral analysis are compared with the X-ray luminosities obtained from Eq. (4.14). Our measurements, within the errors, are in agreement with those derived from the Gandhi et al. (2009) relation.

Next, we exploited the relations derived by Lusso et al. (2012) who analyzed the dependence of the bolometric correction k_{bol} on the bolometric luminosity L_{bol} in the soft and hard X-ray bands for a sample of type-1 and type-2 AGN X-ray selected in the COSMOS field. In particular, the bolometric correction in a given band was computed using the standard definition $k_{\mathrm{band}} = L_{\mathrm{bol}}/L_{\mathrm{band}}$. Their $k_{\mathrm{bol}} - L_{\mathrm{bol}}$

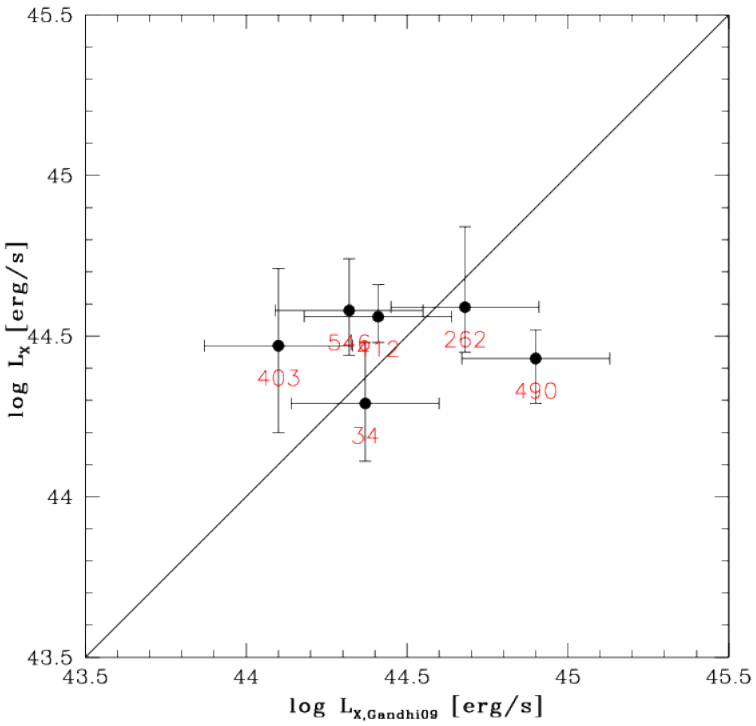

Figure 4.11: Comparison of X-ray luminosities in the range $2-10$ keV obtained through our X-ray spectral analysis and the estimates derived from the Gandhi et al. (2009) relation applied to our sample (see Eq. (4.14)). The solid line shows the 1:1 relation.

three-order polynomial relation is:

$$\log k_{\rm bol} = 0.386 \log \frac{L}{10^{12}} + 0.071 \left(\log \frac{L}{10^{12}} \right)^2 - 0.010 \left(\log \frac{L}{10^{12}} \right)^3 + 0.23 \qquad (4.16)$$

where L is the bolometric luminosity in units of $L_{\odot}$. By applying this correction to our AGN bolometric luminosities we derived an estimate of the X-ray luminosity in the range $2-10$ keV that we compared to the values obtained through spectral analysis. As shown in Fig. 4.12, the X-ray luminosities derived from both the X-ray analysis and the SED fitting through Eq. (4.16) are in agreement within the errors.

To sum up, considering the uncertainties and the different methods adopted to derive the X-ray luminosities, we can conclude that these values are solid physical parameters and representative of the accretion processes occurring in our sources.

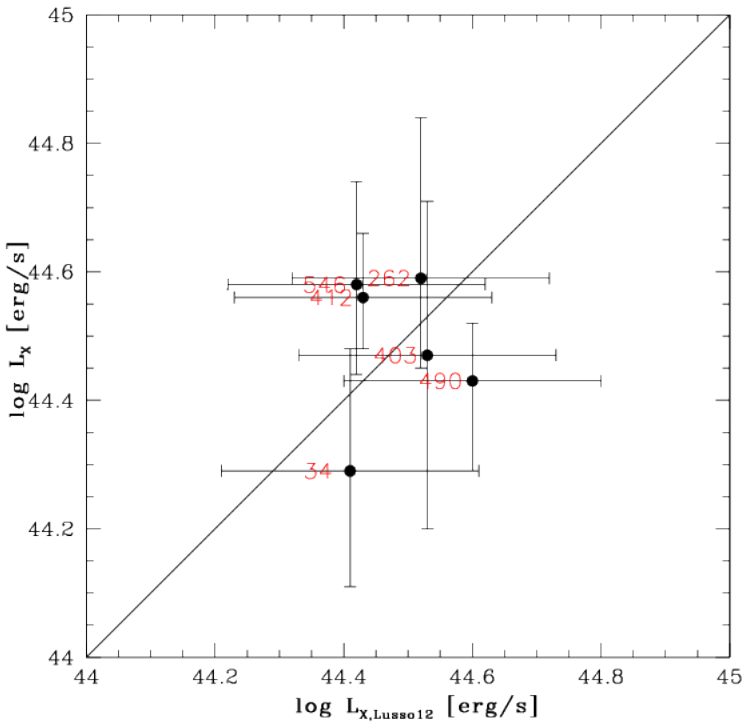

Figure 4.12: X-ray luminosity in the range $2-10$ keV for our sample derived through X-ray spectral analysis over the estimate obtained by applying the k-correction $k_{\rm bol}$ (Lusso et al. 2012) to the AGN bolometric luminosity obtained from the SED fitting. The solid line shows the 1:1 relation.

4.3.2 Star formation rate and molecular gas mass

An important parameter related to the host galaxy that can be determined starting from the SED decomposition is the star formation rate. We considered the IR luminosity due to starburst activity ($L_{\rm FIR}$), i.e. the best-fit values in Table 4.1 (for the source XID403 we considered the IR luminosity in Table 4.2), hence subtracting the contamination due to AGN emission, in order to use the Kennicutt (1998) SFR calibration determined for infrared-selected starburst galaxies :

$$SFR(M_\odot/{\rm yr}) = \frac{L_{\rm FIR}(L_\odot)}{5.8 \times 10^9}. \tag{4.17}$$

This relation is based on the direct coupling between the SFR and the IR luminosity: the bolometric luminosity produced by star formation, dominated by young stars, is mostly absorbed by dust which re-emits it in the IR. The values obtained for the whole sample, reported in Table 4.3, point out an intense star formation activity with SFRs in the range between $\sim$400 and $\sim$1200 $M_\odot$ yr^{-1}.

In order to estimate the gas content of the host galaxy, we derived the molecular gas mass (which is the dominant component) following the work of Scoville et al. (2016), who obtained a relation between the source luminosity at 850 μm rest-frame and the molecular gas mass. They used the long wavelength dust continuum to probe the molecular ISM mass[4]. Indeed, the FIR-submm emission from galaxies is due to dust re-emission which is optically thin in the Rayleigh-Jeans tail of the modified blackbody spectrum reproducing the observed flux density. This emission is directly related to the total dust mass and, through the dust-to-gas abundance ratio, to the ISM mass. In order to calibrate empirically the ratio of the specific luminosity at 850 μm ($\nu = 353$ GHz) rest-frame to the molecular gas mass, Scoville et al. analyzed a sample of local star forming galaxies, ULIRGs and $z \sim 2$ SMGs with both submm observations and CO(1-0) (rotational transition at 2.6 μm rest-frame) integrated fluxes which probe the dust emission and the gas mass, respectively. This ratio was found to be nearly constant across the whole sample:

$$\alpha_\nu \equiv < \frac{L_{\nu 850\mu m}}{M_{\rm mol}} > = 6.7 \pm 1.7 \times 10^{19} \text{ erg s}^{-1} \text{ Hz}^{-1} \text{ M}_\odot^{-1}. \tag{4.18}$$

To use this relation, we computed the flux density $S_{\nu_{850\mu m}/(1+z)}$ from the model SED and then calculated the luminosity at 850 μm rest-frame through the relation (4.15). The estimate of the ISM mass would require to know explicitly the dust opacity curve, the dust temperature and the dust-to-gas abundance ratio, but it is possible to obviate the issue thanks to the calibration reported in (4.18), by absorbing these parameters into the empirical constant α_ν.

Nevertheless, we would like to stress one of the assumptions of this calibration. The estimate of the molecular gas mass from the CO line luminosity requires the use of a conversion factor $\alpha_{\rm CO}$ (in units of $\text{M}_\odot/(\text{K km s}^{-1} \text{ pc}^2)$), through the relation $M_{\rm mol} = \alpha_{\rm CO} L'_{\rm CO}$. This factor likely depends on local ISM conditions, such as pressure, gas dynamics and metallicity, but it is a poorly constrained parameter for different types of galaxies and still an active area of research. $\alpha_{\rm CO} \sim 4.8$ $\text{M}_\odot/(\text{K km s}^{-1} \text{ pc}^2)$ for Giant Molecular Clouds (GMCs) in the Milky Way, and Scoville et al. chose to use a single conversion factor for all galaxies of their sample, equal to the Galactic one, although they analyzed both normal and star-forming galaxies. Indeed, it was found that $\alpha_{\rm CO}$ is lower for highly star-forming systems (based on a radiative transfer model of CO kinematics, Downes & Solomon 1998), which shows

[4]Scoville et al. considered the molecular gas masses rather than HI plus H_2 since the atomic gas was not well measured in many galaxies of their sample.

a characteristic value $\alpha_{\rm CO} \sim 0.8$ M$_\odot$/(K km s^{-1} pc^2), within a range $0.3 - 1.3$ (e.g. Carilli & Walter 2013 and references therein). This lower value would imply more CO emission per unit molecular gas mass, probably deriving from different molecular gas conditions and heating processes in starbursts with respect to normal galaxies (e.g. Papadopoulos et al. 2012). Several studies have been presented which contain discussions about $\alpha_{\rm CO}$ in star-forming galaxies (e.g. Tacconi et al. 2008, Magdis et al. 2012, Magnelli et al. 2012, Bothwell et al. 2013), providing similar values of the conversion factor. Hence, prompted by these results, we decided to rescale the calibration in Eq. (4.18) to an $\alpha_{\rm CO} = 0.8$. Moreover, to account for the atomic hydrogen mass M$_{\rm HI}$, we considered the results by Calura et al. (2014), who converted the [CII]158 μm line luminosity into atomic gass mass for a sample of high-redshift quasar hosts and obtained an average value of $M_{\rm H_2}/M_{\rm HI} \sim 5$ for the whole sample. The obtained gas masses, which are in the range $(0.7 - 3.5) \times 10^{10}$ M$_\odot$, are reported in Table 4.3. These results are in agreement with the values measured tipically for SMGs (e.g. Tacconi et al. 2008, Bothwell et al. 2013), which often show even larger values ($\sim 10^{11}$ M$_\odot$).

Source $^{(a)}$	SFR $^{(b)}$	M$_{\rm gas}$ $^{(c)}$
34	1210 ± 240	2.8 ± 0.7
262	470 ± 100	0.8 ± 0.2
403	930 ± 190	3.7 ± 0.9
412	410 ± 80	0.7 ± 0.2
490	700 ± 140	2.5 ± 0.6
546	450 ± 90	3.5 ± 0.9

Table 4.3: Star formation rates and gas masses derived for our sources by means of the relations (4.17) and (4.18), respectively. $^{(a)}$ XID; $^{(b)}$ SFR in units of M$_\odot$ yr^{-1}; $^{(c)}$ $M_{\rm gas} = M_{\rm H_2} + M_{\rm HI}$ in units of 10^{10} M$_\odot$.

Chapter 5

Discussion and conclusions

5.1 Size of the targets

The co-evolution of the first SMBHs and their host galaxies can be studied, in terms of host galaxy properties, primarily with observations of dust continuum, molecular CO, and [CII] line emission at submillimeter and millimeter wavelengths. The strong thermal FIR continuum is produced by dust heated by young, massive stars, hence representing the regions of active star formation, the CO transitions trace molecular gas which serves as the fuel for star formation, and the [CII] fine structure line emission probes the photodissociation regions (PDRs) and the interstellar medium. High-redshift QSOs and SMGs, the main targets to investigate this co-evolutionary scenario, tend to have significant masses of cold dust as well as substantial reservoirs of molecular gas. Several analyses of both the stellar component and the molecular gas hosted in these sources confirm that they have comparable sizes, both showing compact morphologies. In this regard, Swinbank et al. (2010) performed a detailed study of the stellar structure of a sample of 25 SMGs (including both AGN and starburst galaxies) at redshift between 0.7 and 3.4. They used deep *HST* I- and H-band images and derived typical half-light radii of about 2 kpc. Tacconi et al. (2008), instead, obtained sub-arcsec resolution millimeter interferometry of four SMGs at $z \sim 2$ using IRAM Plateau de Bure Interferometer (PdBI). They detected CO rotational transitions, which are a good tracer of the cold molecular gas from which stars form. The observed emission has a compact intrinsic size, with $r_{\rm half} \lesssim 2$ kpc. The sizes derived by Swinbank et al. (2010) are slightly larger but comparable to the gas sizes measured by Tacconi et al. (2008); this similarity suggests that both the stars and the dense gas are located in compact regions. Furthermore,

Wang et al. (2013) presented ALMA observations of the [CII] fine structure line and heated dust continuum emission of five quasar host galaxies at $z \sim 6$. Their detections reveal intrinsic source sizes of few kpc and indicate active star formation within these regions where both CO and [CII] emission are co-spatial with FIR emission. Other compelling results are provided by Harrison et al. (2016) who presented high-resolution ALMA 870 μm imaging of five high-redshift ($z \sim 1.5-4.5$) AGN host galaxies. They measured the angular size of the rest-frame FIR emission constraining the spatial distribution of star formation. The sub-mm emission results to be extended on scales of FWHM$\sim 0.2'' - 0.5''$, corresponding to physical sizes of $1 - 3$ kpc. However, these sources at FIR/sub-mm wavelengths are usually just marginally resolved; as such, these data do not probe the source morphology, but put tight constraints on the spatial extent of the observed object. All these sources are characterized by physical parameters similar to those derived for our targets, i.e. stellar masses $M_* \sim 10^{10} - 10^{11}$ $M_\odot$, gas masses $M_{gas} \sim 10^{10} - 10^{11}$ $M_\odot$ and IR luminosities $L_{IR} \gtrsim 10^{12}$ $L_\odot$, some of them showing obscured AGN activity detected through X-ray observations.

As far as our sample is concerned, we have solid observational constraints on the extension issue from previous works on the source XID403. De Breuck et al. (2014) presented ALMA Band 7 (345 GHz, i.e. 870 μm) observations of the [CII] line emission and dust continuum, which are confined in a region with a radius smaller than 2 kpc. Moreover, a continuum Band 6 (230 GHz, 1300 μm) observation of this target was analyzed by Gilli et al. (2014), who found an intrinsic source size of 0.27 ± 0.08 arcsec (Gaussian FWHM), corresponding to a dust half-light radius of $r^d_{\rm half} = 0.9 \pm 0.3$ kpc. In the *HST*/WFC3 H-band ($\sim$2800 Å rest-frame) the source presents a stellar half-light radius of $\sim 0.2''$, i.e. $r^*_{\rm half} \sim 1.3$ kpc, comparable to what has been found for the dust emission and in line with the studies mentioned above. For the source XID490 we retrieved from the ALMA Archive[1] a public observation (17 min at $0.2''$ resolution, PI: Leiton, 2012.1.00983) in the ALMA Band 7 and analyzed it with the help of the Italian ALMA Regional Center. The image has been fitted with a single Gaussian component with a FWHM of 0.15 ± 0.01 arcsec. The observation is characterized by a continuum rms of 56 μJy and the flux density measured at the peak is 2.8 mJy, so the resulting signal-to-noise ratio is 50. The corresponding dust half-light radius is $r^d_{\rm half} = 0.6 \pm 0.1$ kpc. This size is more compact than that shown by the stellar component in the *HST*/WFC3 H-

[1] http://almascience.eso.org/alma-data/archive

band, which is of about 0.38″, hence $r^*_{\rm half} \sim 3$ kpc. Unfortunately, dust continuum observations with sub-arcsecond resolution are not available for the other sources of the sample. Therefore, prompted by the similarity between the dust and gas as well as the stellar extents for this kind of sources, we decided to adopt the stellar half-light radius for the targets without additional information, as an estimate of the galaxy size. However, we have to bear in mind that the stellar size can be larger than the dust size and, as a result, the $r^*_{\rm half}$ values have to be considered as upper limits. Indeed, the precise spatial relation between the optical and sub-mm emission in these objects is still unclear, and the sub-mm emission could be more compact that the optical galaxy (Blain et al. 2002).

The half-light radii adopted are reported in Table 5.1: we used the dust half-light radius derived by Gilli et al. (2014) for the source XID403 and the radius obtained from the ALMA Band 7 observation for the source XID490; for the sources XID262, XID412 and XID546 the stellar half-light radii measured with GALFIT by the CANDELS team[2] were adopted (van der Wel et al. 2012); finally, for the source XID34 we measured $r^*_{\rm half}$ in the *HST*/ACS z-band from the GEMS (Galaxy Evolution from Morphology and SEDs) dataset (Haussler et al. 2007), as this source falls outside the CANDELS field.

5.2 Column density

In order to estimate the equivalent column density associated with the gas in the host galaxy, we considered a simple geometrical approximation assuming a spherical gas distribution of uniform density. Hence, under the assumption that both molecular and atomic gas are co-spatial with dust, and considering that half of the total gas mass $M_{\rm gas} = M_{\rm H_2} + M_{\rm HI}$ is confined within $r_{\rm half}$, we computed the ISM column densities for the six sources of our sample. The values obtained are reported in Table 5.1 and range between $\sim 10^{23}$ and $\sim 10^{24}$ cm^{-2}, which are of the same order of those derived from the X-ray spectral analysis. Since we considered an upper limit for the gas size, the resulting column densities are, actually, lower limits. The host ISM can, then, significantly contribute to the observed X-ray obscuration, from $\sim 10\%$ up to being comparable with the value measured from the X-ray spectra. In Fig. 5.1 the ISM column densities are plotted against the values derived from the X-ray spectral analysis: for the sources XID262 and XID412 the contribution of

[2]We adopted the semi-major axis of the ellipse that contains half of the total light in the best fitting Sersic model of the F160W image at $\lambda \sim 1.6$ μm.

the host galaxy is $\gtrsim 10\%$; for XID403, $N_{\mathrm{H,\,ISM}}$ is about half of $N_{\mathrm{H,\,X}}$, while the sources XID34 and XID546 show an almost perfect agreement between the two quantities. The host ISM is, thus, capable of providing heavy absorption, and the obtained column densities could be large enough to "confuse" the picture of pure torus absorption (Netzer 2015). The presence of hot dust surrounding the central engine, and heated by its emission, is supported by the mid-IR "excess" observed in the SED, but this does not mean that it has a toroidal geometry and that it is the only component which takes part in obscuring the active nucleus. Probably, if the evolution of the sources sharing the same properties as ours is led by complex merging phenomena, a simple unification model based on torus-like absorbers and ordered gas motion cannot be adopted to explain the observed emission. Therefore, the study of the obscuration might be addressed using a different interpretation of the distribution of the absorbing material with respect to the simple toroidal shape. The absorption may occur at different physical scales and, in particular, the medium in the host galaxy is an ingredient that should be considered, as it probably has a substantial role in the obscuration issue.

Hopkins et al. (2005, 2006), whose evolutionary scenario was described in § 1.3.1, studied the AGN obscuration during a major merger event by computing the column density along several lines of sight, and modelling the ISM through a hot (diffuse) and a cold (molecular and neutral) phase, with most of the mass distributed in dense and cold structures. They found that the column density does not depend considerably on the assumptions regarding the small-scale physics of the ISM and obscuration, as the central regions of the merging galaxies are expected to be highly chaotic. Moreover, the scales associated with obscuration are related to starburst activity and obscured quasar growth, and turned out to be larger ($\gtrsim$ 100 pc) than the typical scales of traditional tori. In particular, the galaxy is able to generate an important contribution to obscuration. In this scenario, the obscuring column density could be an evolving function of time, luminosity and host galaxy properties, dominated by gas inflows that fuel the central BH in different evolutionary stages. Therefore, a significant population of obscured AGN is produced by the evolution of the column density and the AGN type depends, thus, on the evolutionary stage of the host.

The role of the host galaxy ISM in obscuring the AGN emission has also been studied through several numerical simulations (e.g. Bournaud et al. 2011). Thick gaseous disks in high redshift galaxies subject to violent instability can produce strong obscuration towards the central AGN, characterized by very high column

Source (a)	$r_{\rm half}$ (b)	$r_{\rm half}$ (c)	$N_{\rm H,\ ISM}$ (d)	$N_{\rm H,\ X}$ (e)
34	0.15±0.01	1.2 ± 0.1	2.9 ± 0.9	$2.0^{+1.3}_{-1.0}$
262	0.11±0.01	0.8 ± 0.1	1.8 ± 0.7	$14.8^{+7.7}_{-3.7}$
403	0.14±0.04	0.9 ± 0.3	6.9 ± 4.9	$14.8^{+9.6}_{-5.8}$
412	0.14±0.01	1.0 ± 0.1	1.0 ± 0.3	$9.0^{+2.1}_{-1.7}$
490	0.08±0.01	0.6 ± 0.1	10.4 ± 4.4	$29.0^{+30.7}_{-14.4}$
546	0.14±0.01	1.1 ± 0.1	4.4 ± 1.4	$5.4^{+0.6}_{-0.5}$

Table 5.1: Half-light radii and column densities derived from both the SED-fitting and the X-ray analyses. (a) XID; (b) half-light radius in arcsec; (c) half-light radius in kpc; (d) column density associated with the ISM in the host galaxy, in units of 10^{23} cm^{-2}; (e) column density derived from the X-ray spectral analysis, in units of 10^{23} cm^{-2}.

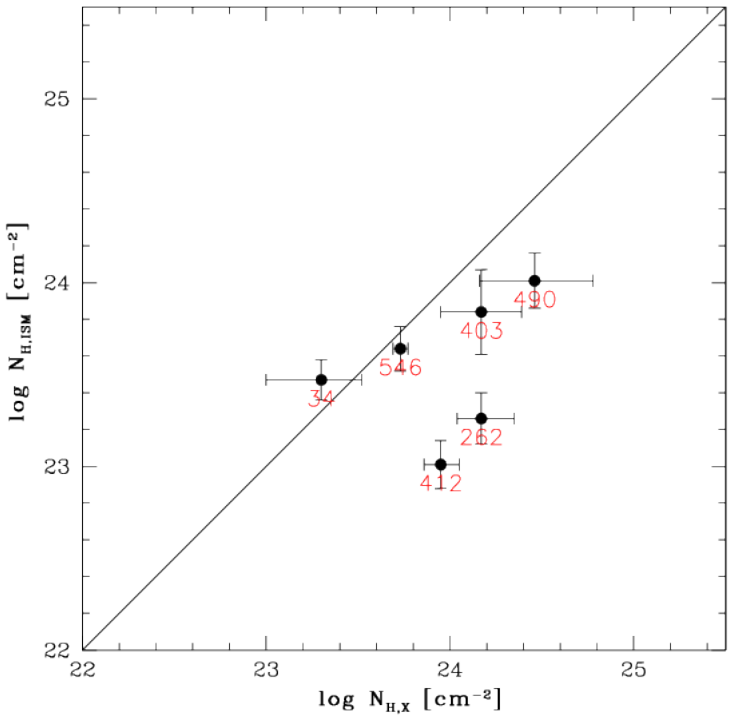

Figure 5.1: ISM column densities plotted against the column densities obtained through X-ray spectral analysis. The solid line shows the 1:1 relation.

densities ($\log N_{\rm H} > 23$), even reaching the Compton-thick regime. Juneau et al. (2013) pointed out that at high redshift, in addition to small-scale absorption (i.e. the pc-scale torus), there are important amounts of gas in galaxies that can potentially contribute to absorb X-rays. In particular, they found that there is a more frequent X-ray absorption in galaxies hosting an AGN with higher sSFRs (i.e., SFR/M_*). A possible explanation for this observed trend is that the gas reservoir which fuels the intense star formation also acts as an important absorber for the AGN. This situation could be more likely at high redshift, where the AGN hosts show an increase in SFR and gas content (e.g. Carilli & Walter 2013).

The kinematics and spatial distribution of the ISM could be better constrained by observing molecular lines, which provide the most direct insight into the physics and behaviour of these systems. SMGs and QSOs often exhibit double-peaked CO spectra, a potential indicator of either the existence of kinematically distinct components within these systems or a rotating disk-like component (e.g. Tacconi et al. 2008, Bothwell et al. 2013). However, only galaxy-integrated line fluxes can be measured at high redshift, and spatially resolved molecular gas observations are restricted to few, bright sources (Carilli & Walter 2013). Therefore, inferring the size of the CO reservoir and studying the kinematic mode that determines the gas dynamics, as well as how the ISM takes part in the obscuration of the central AGN, are very challenging at these redshifts, since observations usually lack the angular resolution necessary to resolve the emission, leading to upper limits on the measured sizes.

5.3 Overall results

The X-ray/multiwavelength analysis performed for our sample aimed at characterizing the properties of both the host galaxy and the AGN. Therefore, putting together our results, we can provide a rather comprehensive picture of the targets. Our AGN hosted in SMGs show heavily obscured accretion activity onto the SMBH along with a powerful concurrent star formation. Thanks to the ability of the X-rays to probe the AGN emission without suffering from significant galaxy contamination, we were able to study the main physical parameters of active nuclei, determined through X-ray spectral analysis. The extracted spectra show the typical features of heavily obscured sources, namely flat slopes coupled with a photoelectric cut-off and a prominent iron line (detected in five out of six objects). Once the column density has been obtained, it is possible to correct the luminosity for the effect produced

by obscuration, computing the intrinc luminosity. In Fig. 5.2 we compare the intrinsic luminosities in the rest-frame $[0.5-10$ keV$]$ band and the column densities derived for our sources with the values measured for a sample of obscured AGN in the XMM-COSMOS field by Mainieri et al. (2011). Our objects are among the most obscured ones, $N_{\rm H} = [(0.3-4)\times10^{24}]$ cm^{-2}, but intrinsically powerful quasars, $\rm L_{[0.5-10]\,keV} = [(2.2-7)\times10^{44}]$ erg s^{-1}.

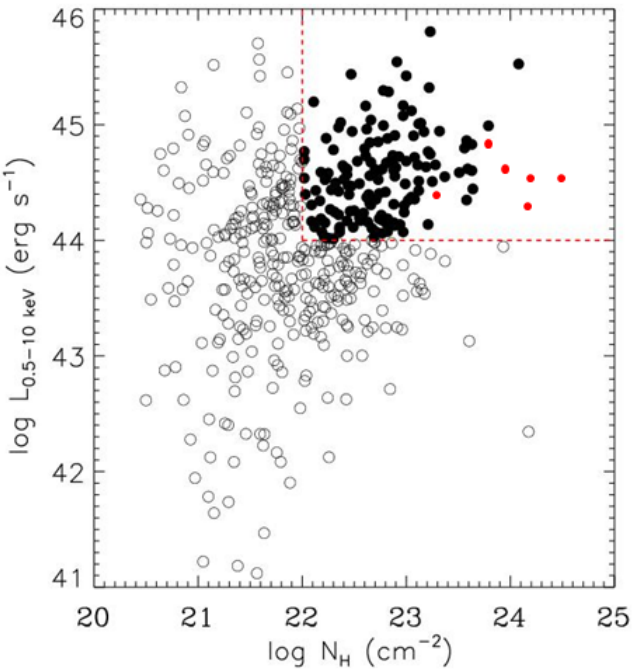

Figure 5.2: Intrinsic rest-frame $[0.5-10$ keV$]$ luminosity vs. column density for a sample of type-2 AGN (black filled circles) in the XMM-COSMOS survey (Mainieri et al. 2011) compared with the results obtained for our sample (red filled circles). Our targets are among the most obscured sources and in the quasar luminosity regime ($\log L_{\rm X} > 44$), populating the upper-right part of the plot.

Moreover, the obscuration to the AGN emission due to gas and dust allowed us to trace the host galaxy properties. Through an SED decomposition technique, we disentangled the contributions to the overall emission produced by the different components which take part in building up the SED. Therefore, we characterized the host in terms of both stellar mass and IR luminosity, the AGN in terms of bolometric luminosity derived from the hot-dust emission in the mid-IR as well as its contribution to the total IR luminosity, hence deriving the SFR (by using the Kennicutt (1998) calibration). In Fig. 5.3, we place our sources in the context of the "main sequence" of star-forming galaxies, i.e. the correlation between SFR and

stellar mass. We considered the study conducted by Schreiber et al. (2015), who presented an analysis of the deepest *Herschel* images along with the stacking of a complete sample of star-forming galaxies, in order to determine the dispersion of this correlation. They measured SFRs by combining UV and far-IR emission, while our measurements rely on the far-IR emission only. The main sequence shows a redshift evolution and a flattening for $M_* > 10^{11}$ $M_\odot$, but the reason for this change in the slope is still unkown. Our sources lie in the high-mass and high-SFR region of the plot, with SFR $= [400 - 1200]$ $M_\odot$ yr^{-1} and $M_* = [(0.8 - 4) \times 10^{11}]$ $M_\odot$. Our targets are characterized by SFRs typical of very massive objects at their redshifts. A few candidates, being above the main sequence, could show an excess of star formation, according to a merger-driven starburst activity. However, accounting for the uncertainties, it is not possible to infer more general conclusions from the position of the sources with respect to the main sequence.

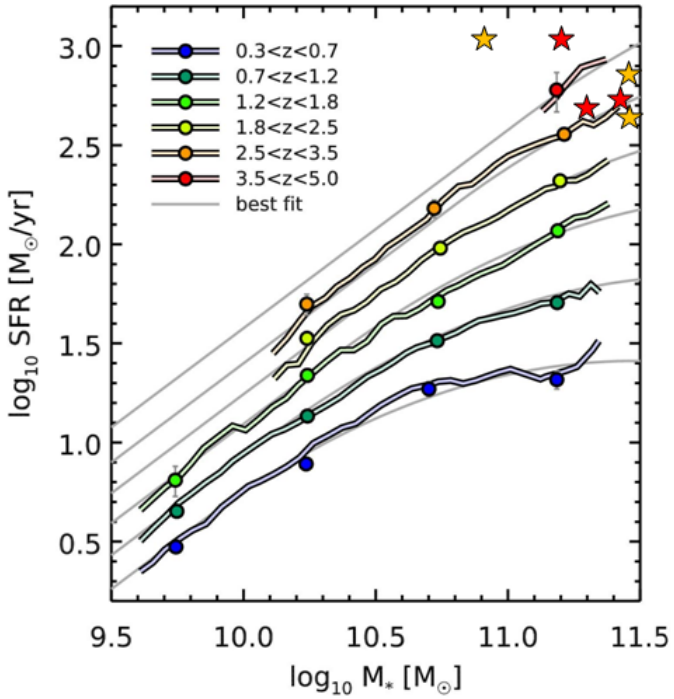

Figure 5.3: Comparison between the SFR of star-forming galaxies at different masses and redshifts (from Schreiber et al. 2015; the results from stacking are displayed as colored solid lines and colored filled circles) and the values derived for our sample (colored filled stars; relative errors are of the order of $\sim$20% for the SFRs and of $\sim$30% for the stellar masses). Colors correspond to the different redshifts as indicated in the legend. Gray solid lines represent the best-fit to the filled circles.

Considering the derived SFRs, gas and stellar masses, and the source sizes, we constrained the surface densities of these quantities (see Table 5.2), assuming a uniform distribution with radius $r_{\rm half}$. As for the surface density of star formation, $\Sigma_{\rm SFR} = (SFR/2)/(\pi r^2_{\rm half})$, it ranges between ~ 60 and ~ 300 $M_\odot$ yr^{-1} kpc^{-2}, in line with the range found by, e.g., Harrison et al. (2016), $\sim 20 - 200$ $M_\odot$ yr^{-1} kpc^{-2}, for a sample of X-ray selected AGN at $z \sim 1.5 - 4.5$ and observed with ALMA (see also Genzel et al. 2010 and Hodge et al. 2013). Similarly, under the assumption that both atomic and molecular gas are co-spatial, we estimated the gas surface density, $\Sigma_{\rm gas} = \Sigma_{\rm HI+H_2} = (M_{\rm gas}/2)/(\pi r^2_{\rm half})$, with values in the range $(0.1 - 1.1) \times 10^{10}$ $M_\odot$ kpc^{-2}. Finally, we combined the size and stellar mass estimates to derive the stellar surface density, $\Sigma_* = (M_*/2)/(\pi r^2_{\rm half})$, where $r_{\rm half}$ is the stellar half-light radius for all sources. Our results are in the range $(0.7 - 7.5) \times 10^{10}$ $M_\odot$ kpc^{-2}. These values are in agreement with those typically found for SMGs (see, e.g., Daddi et al. 2010 and Swinbank et al. 2010 for a comparison with $\Sigma_{\rm gas}$ and Σ_* obtained for SMGs).

Source (a)	$\Sigma_{\rm SFR}$ (b)	$\Sigma_{\rm gas}$ (c)	Σ_* (d)	$t_{\rm dep}$ (e)
34	134±27	3.1 ± 0.9	1.1 ± 0.4	2.3 ± 0.7
262	118±24	1.9 ± 0.7	7.5 ± 2.2	1.7 ± 0.5
403	184±44	7.3 ± 3.2	1.6 ± 0.9	4.0 ± 1.2
412	66±13	1.1 ± 0.4	3.0 ± 1.1	1.7 ± 0.5
490	312±65	11 ± 5	0.7 ± 0.2	3.5 ± 1.1
546	59±12	4.6 ± 1.4	5.4 ± 1.9	7.7 ± 2.5

Table 5.2: Surface densities and gas depletion time derived for the whole sample. $^{(a)}$ XID; $^{(b)}$ SFR surface density in units of $M_\odot$ yr^{-1} kpc^{-2}; $^{(c)}$ gas surface density in units of 10^9 $M_\odot$ kpc^{-2}; $^{(d)}$ stellar surface density in units of 10^{10} $M_\odot$ kpc^{-2}; $^{(e)}$ depletion time in units of 10^7 yr.

High-redshift QSOs and SMGs are thought to be complex systems of dense gas, massive star formation and even AGN activity. Tacconi et al. (2008) suggested that a significant fraction of the stellar mass of these objects ($\sim 50\%$) formed and assembled during their most active phase, while the rest formed over a longer period of time. Taking into account the high SFRs, we can estimate the gas exhaustion timescale, i.e. the time that the available gas needs to be depleted assuming a

constant SFR. Hence, $t_{\rm dep} = M_{gas}/{\rm SFR}$ resulted to be in the range $\sim (2-8) \times 10^7$ yr. After this timescale, corresponding roughly to the duration of the SMG phase, the galaxy would end up as a compact remnant with quiescent activity, because of feedback from AGN and supernovae. It has been argued that SMGs at high redshift (e.g. Tacconi et al. 2008, Gilli et al. 2014) could be the best progenitors of the compact quiescent galaxies (cQGs; e.g. Barro et al. 2013) observed at $1 \lesssim z \lesssim 3$. Indeed, these objects show compact morphologies, with stellar half-light radii ${\rm r_{half}} \sim 0.5-2$ kpc and stellar surface densities $\Sigma_* > 10^{10}$ ${\rm M_\odot}$ ${\rm kpc^{-2}}$. The formation channel of the cQGs is still an open issue. However, we showed that our sources have a compact (sub-kpc for most of the sample) stellar core with stellar surface densities similar to those of cQGs observed at $z > 1$. Therefore, according to the values derived for SFR, stellar mass, gas depletion timescale and size, our targets could be the progenitors of this kind of systems.

5.4 Summary and conclusions

We have presented a multiwavelength analysis of a sample of heavily obscured AGN and their host galaxies at high redshift. Through this study, we were able to characterize the properties of both the active nuclei and the hosts. Moreover, our results put constraints on the role of the host ISM in obscuring the AGN, and place this work in the framework of AGN evolution and their accretion history across cosmic time. Obscured AGN can be very elusive sources, because of obscuration produced by large amounts of gas which feed both accretion onto the SMBH and star formation in the galaxy, producing an intimate connection between the AGN and their hosts (i.e. the BH-galaxy co-evolution). In this research area, deep surveys represent fundamental tools, since they are able to disclose a large fraction of obscured AGN, which constitute the bulk of the AGN population.

- We used a large dataset spanning a broad range of wavelengths, from the X-ray to the sub-mm band, each range showing the imprints of a specific emission component. In particular, we performed the X-ray study of the targets exploiting the extraordinary capability of X-rays to trace the accretion activity occurring in active nuclei. To this end, we used the deepest X-ray observations available so far, the 7Ms exposure of the CDF-S. Moreover, thanks to the broad-band coverage supporting this field, we were able to perform the multiwavelength study of the hosts as well, using the broad-band photometry

from CANDELS and *Herschel*, as well as high-resolution ALMA observations for some sources. We collected a sample of six X-ray selected type-2 AGN at $z > 2.5$, characterized by $\log N_{\rm H} > 23$ and good *Herschel* FIR detections.

- We extracted the X-ray spectra from the 7Ms *Chandra* dataset and performed an analysis by means of proper models, in order to characterize the spectral properties and gather information about AGN physical parameters. In particular, we derived the obscuring column densities, $N_{\rm H} = [(0.3 - 4) \times 10^{24}]$ cm^{-2}, and the intrinsic rest-frame $[2 - 10$ keV$]$ band luminosities, $\rm L_{[2-10]\,keV} = [(2 - 6) \times 10^{44}]$ erg s^{-1}. Moreover, we studied the iron Kα line, a prominent feature in obscured AGN spectra, whose EW resulted to be $\gtrsim 0.5$ keV, even up to few keV for the most obscured sources. Moreover, the improved spectral quality of the 7Ms dataset allowed us to detect the iron line in three sources where this feature was not detected in previous works.

- We built up the UV to FIR SEDs for our targets and analyzed them by means of an SED decomposition technique. Therefore, the contribution of the different components playing a key role in the overall emission (namely stars, dust and active nucleus) can be disentangled and, thus, the characteristic parameters of the sources can be derived: stellar mass, $\rm M_* = [(0.8 - 4) \times 10^{11}]$ $\rm M_\odot$, total IR ($8 - 1000$ μm) luminosity, $\rm L_{IR} = [(2 - 7) \times 10^{12}]$ $\rm L_\odot$ and AGN bolometric luminosity, $\rm L_{bol} = [(2-5) \times 10^{12}]$ $\rm L_\odot$. Moreover, by subtracting the AGN contribution to the total IR luminosity, we measured the SFRs assuming a Kennicutt (1998) calibration law, hence obtaining SFR $= [400 - 1200]$ $\rm M_\odot$ yr^{-1}.

- The gas mass in the host galaxy was estimated by using the Scoville et al. (2016) calibration, which relates the intrinsic luminosity at 850 μm rest-frame (derived from the model SED and interpreted as emission from dust heated by star formation) to the molecular gas mass, i.e. the fuel for the SF activity. Our targets host large reservoirs of cold gas, $\rm M_{mol} = [(0.7 - 3.5) \times 10^{10}]$ $\rm M_\odot$. Then, under the assumption that stars and ISM are confined within regions of comparable size (as observed for different samples of QSOs and SMGs at high redshift), we assessed the source size by adopting either the dust half-light radius, when available from ALMA observations of the dust continuum emission, or the stellar half-light radius, measured with GALFIT by the CANDELS team. Finally, adopting a simple geometrical model, i.e. a spherical gas

distribution of uniform gas, we computed the column density associated with the ISM in the host galaxy.

- The comparison between the column densities measured from the X-ray spectral analysis with those associated with the host galaxy pointed out that the contribution of the host ISM to the obscuration of the AGN emission can be substantial, ranging from $\sim 10\%$ up to $\sim 100\%$ of the value derived from the X-ray spectra. The absorption may occur at different physical scales in these sources and, in particular, the medium in the host galaxy is an ingredient that should be taken into account, since it may have a relevant role in driving the early co-evolution of galaxies with their black holes. It appears therefore likely that the obscuration is not totally ascribed to the parsec-scale torus of the unified model, but that a fraction of the obscuration is related to the host galaxy, at least at high redshift. Therefore, the AGN unification suggested to explain the observations of lower-luminosity (and arguably secularly evolving) systems, may not apply to powerful quasars at high redshift.

5.4.1 Future perspectives

We performed our analysis on a small number of targets, but we aim at enlarging the sample in the near future. Indeed, the search for potential candidates could be carried out in other deep fields, such as the CDF-N, the COSMOS field and the SUBARU deep field (all part of a deep and extensive X-ray plus multiwavelength coverage), taking into account a wider redshift range as well. Thanks to these additional datasets we could improve the statistics of the sample by a factor $2 - 3$.

The role of high-resolution ALMA observations is fundamental in this study, since it is possible to build up large samples of high-redshift galaxies with accurate measurements of the angular sizes of the rest-frame FIR emission and, consequently, to constrain the spatial distribution of star formation activity. In this regard, ALMA observations have been proposed by our group for a sample of sources that includes some objects analyzed in this work. The goal of the proposal is to recover the source flux density and sample the dust continuum emission in the SED of the targets, thus providing an estimate of the gas mass in the galaxy. At the same time, it is possible to place constraints on the extent of the emitting region, obtaining a better estimate of the ISM column density. Furthermore, the ALMA archive is being enriched with new observations, especially of sources in the CDF-S, which may represent new targets for our analysis. Finally, a comparison with a sample of unobscured AGN

at similar redshift could provide useful information about the condition of the ISM with respect to the AGN type and the possibility to test whether the unified model holds at high redshift.

Bibliography

Alexander, D. M., Bauer, F. E., Brandt, W. N., et al. 2003, AJ, 126, 539

Alexander, D. M., Bauer, F. E., Chapman, S. C., et al. 2005a, ApJ, 632, 736

Alexander, D. M. & Hickox, R. C. 2012, Nature, 56, 93

Alexander, D. M., Smail, I., Bauer, F. E., et al. 2005b, Nature, 434, 738

Antonucci, R. 1993, ARA&A, 31, 473

Arnaud, K. A. 1996, in Astronomical Society of the Pacific Conference Series, Vol. 101, Astronomical Data Analysis Software and Systems V, ed. G. H. Jacoby & J. Barnes, 17

Asmus, D., Gandhi, P., Hönig, S. F., Smette, A., & Duschl, W. J. 2015, MNRAS, 454, 766

Avni, Y. 1976, ApJ, 210, 642

Barvainis, R. 1987, ApJ, 320, 537

Beckmann, V. & Shrader, C. R. 2012, Active Galactic Nuclei

Bertelli, G., Bressan, A., Chiosi, C., Fagotto, F., & Nasi, E. 1994, A&AS, 106

Bianchi, S. 2013, A&A, 552, A89

Blain, A. W., Smail, I., Ivison, R. J., Kneib, J.-P., & Frayer, D. T. 2002, Phys. Rep., 369, 111

Bothwell, M. S., Smail, I., Chapman, S. C., et al. 2013, MNRAS, 429, 3047

Bournaud, F., Chapon, D., Teyssier, R., et al. 2011a, ApJ, 730, 4

Bournaud, F., Dekel, A., Teyssier, R., et al. 2011b, ApJ, 741, L33

Brandt, W. N. & Alexander, D. M. 2010, Proceedings of the National Academy of Science, 107, 7184

Brandt, W. N. & Alexander, D. M. 2015, A&A Rev., 23, 1

Bressan, A., Granato, G. L., & Silva, L. 1998, A&A, 332, 135

Brightman, M. & Nandra, K. 2011, MNRAS, 413, 1206

Bruzual, G. & Charlot, S. 2003, MNRAS, 344, 1000

Burlon, D., Ajello, M., Greiner, J., et al. 2011, ApJ, 728, 58

Burtscher, L., Meisenheimer, K., Tristram, K. R. W., et al. 2013, A&A, 558, A149

Calura, F., Gilli, R., Vignali, C., et al. 2014, MNRAS, 438, 2765

Calzetti, D., Kinney, A. L., & Storchi-Bergmann, T. 1994, ApJ, 429, 582

Carilli, C. L. & Walter, F. 2013, ARA&A, 51, 105

Cash, W. 1979, ApJ, 228, 939

Chabrier, G. 2003, PASP, 115, 763

Chapman, S. C., Blain, A. W., Smail, I., & Ivison, R. J. 2005, ApJ, 622, 772

Comastri, A. 2004, in Astrophysics and Space Science Library, Vol. 308, Supermassive Black Holes in the Distant Universe, ed. A. J. Barger, 245

Comastri, A., Ranalli, P., Iwasawa, K., et al. 2011, A&A, 526, L9

Coppin, K. E. K., Chapman, S. C., Smail, I., et al. 2010, MNRAS, 407, L103

Daddi, E., Elbaz, D., Walter, F., et al. 2010, ApJ, 714, L118

De Breuck, C., Williams, R. J., Swinbank, M., et al. 2014, A&A, 565, A59

Del Moro, A., Alexander, D. M., Bauer, F. E., et al. 2016, MNRAS, 456, 2105

Delvecchio, I., Gruppioni, C., Pozzi, F., et al. 2014, MNRAS, 439, 2736

Di Matteo, T. 1999, ArXiv Astrophysics e-prints

Done, C. 2010, ArXiv e-prints

Downes, D. & Solomon, P. M. 1998, ApJ, 507, 615

Elvis, M., Wilkes, B. J., McDowell, J. C., et al. 1994, ApJS, 95, 1

Fabian, A. C., Iwasawa, K., Reynolds, C. S., & Young, A. J. 2000, PASP, 112, 1145

Fabian, A. C. & Miniutti, G. 2005, ArXiv Astrophysics e-prints

Feltre, A. 2013, PhD thesis

Feltre, A., Hatziminaoglou, E., Fritz, J., & Franceschini, A. 2012, MNRAS, 426, 120

Ferrarese, L. & Merritt, D. 2000, ApJ, 539, L9

Fritz, J., Franceschini, A., & Hatziminaoglou, E. 2006, MNRAS, 366, 767

Gandhi, P., Horst, H., Smette, A., et al. 2009, A&A, 502, 457

Genzel, R., Tacconi, L. J., Gracia-Carpio, J., et al. 2010, MNRAS, 407, 2091

Georgantopoulos, I., Rovilos, E., & Comastri, A. 2011, A&A, 526, A46

Giacconi, R., Zirm, A., Wang, J., et al. 2002, ApJS, 139, 369

Giavalisco, M., Ferguson, H. C., Koekemoer, A. M., et al. 2004, ApJ, 600, L93

Gilli, R., Comastri, A., & Hasinger, G. 2007, A&A, 463, 79

Gilli, R., Norman, C., Vignali, C., et al. 2014, A&A, 562, A67

Gilli, R., Salvati, M., & Hasinger, G. 2001, A&A, 366, 407

Grogin, N. A., Kocevski, D. D., Faber, S. M., et al. 2011, ApJS, 197, 35

Gruppioni, C., Pozzi, F., Polletta, M., et al. 2008, ApJ, 684, 136

Hainline, L. J., Blain, A. W., Smail, I., et al. 2011, ApJ, 740, 96

Harrison, C. M., Simpson, J. M., Stanley, F., et al. 2016, MNRAS, 457, L122

Hatziminaoglou, E., Fritz, J., Franceschini, A., et al. 2008, MNRAS, 386, 1252

Hatziminaoglou, E., Omont, A., Stevens, J. A., et al. 2010, A&A, 518, L33

Häussler, B., McIntosh, D. H., Barden, M., et al. 2007, ApJS, 172, 615

Hodge, J. A., Karim, A., Smail, I., et al. 2013, ApJ, 768, 91

Hogg, D. W. 1999, ArXiv Astrophysics e-prints

Hopkins, P. F., Hernquist, L., Cox, T. J., et al. 2005, ApJ, 630, 705

Hopkins, P. F., Hernquist, L., Cox, T. J., et al. 2006, ApJS, 163, 1

Hopkins, P. F., Hernquist, L., Cox, T. J., & Kereš, D. 2008, ApJS, 175, 356

Iwasawa, K., Gilli, R., Vignali, C., et al. 2012, A&A, 546, A84

Jacoby, G. H., Hunter, D. A., & Christian, C. A. 1984, ApJS, 56, 257

Juneau, S., Dickinson, M., Bournaud, F., et al. 2013, ApJ, 764, 176

Kellermann, K. I., Sramek, R. A., Schmidt, M., Green, R. F., & Shaffer, D. B. 1994, AJ, 108, 1163

Kennicutt, Jr., R. C. 1998, ApJ, 498, 541

Kennicutt, Jr., R. C., Schweizer, F., & Barnes, J. E. 1996, Galaxies: Interactions and Induced Star Formation

Kocevski, D. D., Lemaux, B. C., Lubin, L. M., et al. 2011, ApJ, 736, 38

Kroupa, P., Tout, C. A., & Gilmore, G. 1993, MNRAS, 262, 545

Kurucz, R. 1993, SYNTHE Spectrum Synthesis Programs and Line Data. Kurucz CD-ROM No. 18. Cambridge, Mass.: Smithsonian Astrophysical Observatory, 1993., 18

La Franca, F., Fiore, F., Comastri, A., et al. 2005, ApJ, 635, 864

Laird, E. S., Nandra, K., Pope, A., & Scott, D. 2010, MNRAS, 401, 2763

Lampton, M., Margon, B., & Bowyer, S. 1976, ApJ, 208, 177

Lanzuisi, G., Ranalli, P., Georgantopoulos, I., et al. 2015, A&A, 573, A137

Levenson, N. A., Sirocky, M. M., Hao, L., et al. 2007, ApJ, 654, L45

Luo, B., Bauer, F. E., Brandt, W. N., et al. 2008, ApJS, 179, 19

Lusso, E., Comastri, A., Simmons, B. D., et al. 2012, MNRAS, 425, 623

Madau, P., Pozzetti, L., & Dickinson, M. 1998, ApJ, 498, 106

Magdis, G. E., Daddi, E., Béthermin, M., et al. 2012, ApJ, 760, 6

Magdziarz, P. & Zdziarski, A. A. 1995, MNRAS, 273, 837

Magnelli, B., Saintonge, A., Lutz, D., et al. 2012, A&A, 548, A22

Magorrian, J., Tremaine, S., Richstone, D., et al. 1998, AJ, 115, 2285

Mainieri, V., Bergeron, J., Hasinger, G., et al. 2002, A&A, 393, 425

Mainieri, V., Bongiorno, A., Merloni, A., et al. 2011, A&A, 535, A80

Mainieri, V., Rigopoulou, D., Lehmann, I., et al. 2005, MNRAS, 356, 1571

Maiolino, R. & Rieke, G. H. 1995, ApJ, 454, 95

Mateos, S., Barcons, X., Carrera, F. J., et al. 2005, A&A, 444, 79

Mathis, J. S., Rumpl, W., & Nordsieck, K. H. 1977, ApJ, 217, 425

McLeod, K. K. 1997, Near-IR Properties of Quasar Host Galaxies, ed. D. L. Clements & I. Pérez-Fournon (Berlin, Heidelberg: Springer Berlin Heidelberg), 45–50

Moran, E. C., Filippenko, A. V., & Chornock, R. 2002, ApJ, 579, L71

Mortlock, D. J., Warren, S. J., Venemans, B. P., et al. 2011, Nature, 474, 616

Murphy, K. D. & Yaqoob, T. 2009, MNRAS, 397, 1549

Nandra, K. & Pounds, K. A. 1994, MNRAS, 268, 405

Nenkova, M., Sirocky, M. M., Ivezić, Ž., & Elitzur, M. 2008a, ApJ, 685, 147

Nenkova, M., Sirocky, M. M., Nikutta, R., Ivezić, Ž., & Elitzur, M. 2008b, ApJ, 685, 160

Netzer, H. 2013, The Physics and Evolution of Active Galactic Nuclei

Netzer, H. 2015, ARA&A, 53, 365

Norman, C., Hasinger, G., Giacconi, R., et al. 2002, ApJ, 571, 218

Papadopoulos, P. P., van der Werf, P. P., Xilouris, E. M., et al. 2012, MNRAS, 426, 2601

Peterson, B. M. 2003, An Introduction to Active Galactic Nuclei

Piovan, L., Tantalo, R., & Chiosi, C. 2006a, MNRAS, 366, 923

Piovan, L., Tantalo, R., & Chiosi, C. 2006b, MNRAS, 370, 1454

Pozzi, F., Vignali, C., Gruppioni, C., et al. 2012, MNRAS, 423, 1909

Rangwala, N., Maloney, P. R., Glenn, J., et al. 2011, ApJ, 743, 94

Rigopoulou, D., Mainieri, V., Almaini, O., et al. 2009, MNRAS, 400, 1199

Risaliti, G. & Elvis, M. 2004, in Astrophysics and Space Science Library, Vol. 308, Supermassive Black Holes in the Distant Universe, ed. A. J. Barger, 187

Risaliti, G., Elvis, M., Fabbiano, G., et al. 2007, ApJ, 659, L111

Salpeter, E. E. 1955, ApJ, 121, 161

Sanders, D. B., Soifer, B. T., Elias, J. H., et al. 1988, ApJ, 325, 74

Santini, P., Ferguson, H. C., Fontana, A., et al. 2015, ApJ, 801, 97

Schmidt, M. 1959, ApJ, 129, 243

Schreiber, C., Pannella, M., Elbaz, D., et al. 2015, A&A, 575, A74

Scoville, N., Sheth, K., Aussel, H., et al. 2016, ApJ, 820, 83

Shakura, N. I. & Sunyaev, R. A. 1973, A&A, 24, 337

Silverman, J. D., Kampczyk, P., Jahnke, K., et al. 2011, ApJ, 743, 2

Swinbank, A. M., Smail, I., Chapman, S. C., et al. 2010, MNRAS, 405, 234

Szokoly, G. P., Bergeron, J., Hasinger, G., et al. 2004, ApJS, 155, 271

Tacconi, L. J., Genzel, R., Smail, I., et al. 2008, ApJ, 680, 246

Thomas, D., Maraston, C., Bender, R., & Mendes de Oliveira, C. 2005, ApJ, 621, 673

Tozzi, P., Gilli, R., Mainieri, V., et al. 2006, A&A, 451, 457

Treister, E., Natarajan, P., Sanders, D. B., et al. 2010, Science, 328, 600

Treister, E., Urry, C. M., Van Duyne, J., et al. 2006, ApJ, 640, 603

Tristram, K. R. W., Meisenheimer, K., Jaffe, W., et al. 2007, A&A, 474, 837

Ueda, Y., Akiyama, M., Hasinger, G., Miyaji, T., & Watson, M. G. 2014, ApJ, 786, 104

Urry, C. M. & Padovani, P. 1995, PASP, 107, 803

van der Wel, A., Bell, E. F., Häussler, B., et al. 2012, ApJS, 203, 24

Vignali, C. 2014, in IAU Symposium, Vol. 304, Multiwavelength AGN Surveys and Studies, ed. A. M. Mickaelian & D. B. Sanders, 132–138

Vignali, C., Piconcelli, E., Lanzuisi, G., et al. 2011, MNRAS, 416, 2068

Vignali, C., Pozzi, F., Fritz, J., et al. 2009, MNRAS, 395, 2189

Vito, F., Gilli, R., Vignali, C., et al. 2014, MNRAS, 445, 3557

Vito, F., Vignali, C., Gilli, R., et al. 2013, MNRAS, 428, 354

Volonteri, M. 2012, Science, 337, 544

Walcher, J., Groves, B., Budavári, T., & Dale, D. 2011, Ap&SS, 331, 1

Wang, R., Wagg, J., Carilli, C. L., et al. 2013a, ApJ, 773, 44

Wang, S. X., Brandt, W. N., Luo, B., et al. 2013b, ApJ, 778, 179

Wardlow, J. L., Smail, I., Coppin, K. E. K., et al. 2011, MNRAS, 415, 1479

Xue, Y. Q., Luo, B., Brandt, W. N., et al. 2011, ApJS, 195, 10

Yaqoob, T. 1997, ApJ, 479, 184